THE UNIVERSITY OF CHICAGO

SEARCH FOR NON-STANDARD MODEL BEHAVIOR, INCLUDING CP VIOLATION, IN HIGGS PRODUCTION AND DECAY TO ZZ^*

A DISSERTATION SUBMITTED TO
THE FACULTY OF THE DIVISION OF THE PHYSICAL SCIENCES
IN CANDIDACY FOR THE DEGREE OF
DOCTOR OF PHILOSOPHY

DEPARTMENT OF PHYSICS

BY
JORDAN WEBSTER

CHICAGO, ILLINOIS
AUGUST 2015

Table of Contents

List of Figures

List of Tables

Acknowledgments

This thesis was made possible due to the help and support provided by many individuals over the last couple years. First and foremost I thank my advisor, Jim Pilcher, for encouraging me to work on challenging problems and teaching me to maintain a broad perspective. I also thank Eric Feng for tirelessly supporting the work in this thesis, and for spending hours on end teaching me simple lessons in particle physics. I owe thanks many other collaborators in the ATLAS HSG2 group; this is truly a shared piece of work.

Other members of the Chicago HEP group have provided me with indispensable support throughout my graduate education. I thank my first advisor, Florencia Canelli, for teaching me how to think like a particle physicist. I also thank Mel Shochet for trusting me with one of the most fun and challenging hardware projects on ATLAS. Thanks to Young-Kee Kim for bringing me chocolate-filled croissants every morning while we worked together installing FTK HOLA cards. I had the privilege to work with many incredibly talented post-docs over the years, including Joe Tuggle, John Alison, Jamie Saxon, Bjoern Penning, Lauren Tompkins, Antonio Boveia, and Georgios Choudalakis. I thank all of you for your patience. In addition, I thank all of my fellow students for being willing to help me through analysis problems and talk through new ideas. In particular, thanks to Sam Meehan, Jeff Dandoy, Anton Kapliy, Ho Ling Li, Constantinos Melachrinos, Joakim Olsson, Patrick Bryant, Karol Krizka, and Chris Meyer. Thanks to Y^2 Cheng for constantly reminding me to keep my eyes on the real prize.

Finally, I thank my family and friends who have been influential in my life, and who have helped me make it to where I am today. I would not have finished this thesis without you. Thanks to Debbe, Scott, Bryce and Cait for their unconditional support. Thanks to Judy for giving me the occasional opportunity to escape Hyde Park for a home-cooked meal. Thanks to Cathy for her loving support, which has kept me alive and (mostly) sane while writing this thesis. Thanks to Tranisha and Jisette for keeping my competitive spirit alive. Thanks to Mik, Pauline, Jake, Marc, Monika, Bobby, Jessica, Kara, and Dr. Low for being encouraging and fun. Thanks to Tim, Kathryn, and all of the Brooks Brothers for supporting me and broadening my perspective.

This work is dedicated to all of you.

Abstract

This thesis presents an ATLAS study of the tensor structure characterizing the interaction of the scalar Higgs boson with two Z bosons. The measurement is based on 25 fb^{-1} of proton-proton collision data produced at the Large Hadron Collider with center of mass energy equal to 7 and 8 TeV. Nine discriminant observables in the four lepton final state are used to search for CP-odd and CP-even components in the Lagrangian beyond those of the Standard Model. These are represented by $\frac{\tilde{\kappa}_{AVV}}{\kappa_{SM}} \tan\alpha$ and $\frac{\tilde{\kappa}_{HVV}}{\kappa_{SM}}$, respectively. Both of these parameters are found to be consistent with their predicted Standard Model values of zero. Values outside the intervals $-3.24 < \frac{\tilde{\kappa}_{AVV}}{\kappa_{SM}} \tan\alpha < 0.91$ and $-0.82 < \frac{\tilde{\kappa}_{HVV}}{\kappa_{SM}} < 0.87$ are excluded at 95% confidence level. These results are combined with a search for the same structure in the interaction of the Higgs with pairs of W bosons.

Chapter 1
Introduction

The observation of the Higgs boson in 2012 [1, 2] is a shining achievement for the first run of the Large Hadron Collider. Its discovery completes the Standard Model and makes it possible to fully check the consistency of the electroweak theory. Over the past three years there has been an intense effort to measure all properties of the newly discovered boson. Most results so far are remarkably consistent with the Standard Model predictions, but it is important to continue these tests.

Some extensions to the Standard Model predict that the Higgs boson has spin and charge-parity quantum numbers that differ from the Standard Model values [3, 4]. The charge-parity state of the Higgs can be tested by measuring the tensor structure of the Higgs decay to vector bosons pairs. In this thesis, $H \to ZZ^* \to 4\ell$ decays in the ATLAS detector are used to measure the tensor structure of the HZZ interaction assuming that the Higgs is a scalar particle. The purpose of the measurement is to look for possible non Standard Model terms that depend on the CP (charge conjugation $\times$ parity) mixture of the boson. Such contributions could point to CP violation in the Higgs sector and impact the role of the Higgs in electroweak symmetry breaking.

This thesis is organized as follows. Chapter 2 provides an overview of the Standard Model and the Higgs boson. The measured parameters of the tensor structure are defined at the end of the chapter. Chapter 3 provides an overview of the Large Hadron Collider and the ATLAS experiment. Chapter 4 provides a detailed description of the analysis that is used to make measurements. The results are presented in Chapter 5. In Chapter 6, the results are combined with a search for the same tensor structure for the HWW interaction. Finally, concluding remarks are provided in Chapter 7.

Chapter 2

A Survey of Higgs Boson Theory

The Standard Model is a theory of fundamental particles and interactions that has been developed over several decades under the guidance of theoretical predictions and experimental observations. It has been found to describe accurately particle interactions at the highest energies studied in laboratories. One of the central particles in the Standard Model is the Higgs boson, which gives mass to the other elementary particles. The Higgs boson was not observed until recently, and it is now being studied thoroughly at the Large Hadron Collider. This chapter provides an overview of the Standard Model and the Higgs boson.

2.1 The Standard Model

The Standard Model (SM) [5–8] of particle physics was developed in the latter half of the 20th century. It encompasses three of the four fundamental forces of nature: the strong, electromagnetic, and weak forces. The interactions described by the SM have an impact on everyday life. Strong interactions in the nuclei of atoms ensure the stability of ordinary matter. Electromagnetic interactions between electrons and nuclei are responsible for the formation of atoms and the emission of light from atomic transitions. Weak interactions are responsible for β decay, a process that allows the Earth and Sun to generate heat.

The SM is based on a mathematical framework called Quantum Field Theory [9], which is used to construct quantum mechanical models of particles. Within the framework, particles are represented by states of quantized fields. In the SM, matter is made up of fermions called quarks and leptons, which correspond to fields of half-integer spin. There are two types of quarks: up-type and down-type. The up-type quarks have an electric charge of $+2/3$ and the down-type quarks have a charge of $-1/3$. Leptons are also divided into two types. There are neutral leptons called neutrinos and massive leptons like the electron with a charge of -1. Furthermore, there are three families of each of these quark and lepton types, with progressively heavier quarks and charged leptons in each family. The heavier charged leptons are the muon and the tau. Each of these particles also has an anti-matter counterpart with opposite charge.

Interactions among particles are governed by a Lagrangian. The SM is a gauge theory, meaning the Lagrangian is invariant under a continuous group of local transformations. In particular, the SM Lagrangian is invariant under transformations of the group $SU(3) \times SU(2) \times U(1)$. Gauge fields with integer spin are included in the model to maintain this invariance, and excitations in these fields correspond to gauge bosons. There are a total of twelve gauge bosons: eight gluons corresponding to the generators of $SU(3)$, two oppositely charged W bosons corresponding to generators of $SU(2)$, and a neutral Z boson and a photon (γ), which correspond to linear combinations of generators for $SU(2)$ and $U(1)$. The gauge bosons ensure that the SM is renormalizable, which is a form of consistency that is necessary for the model to have predictive power.

The fermion and gauge fields mentioned above are enough to define a renormalizable theory of interacting particles. However, the theory is not consistent with experimental observations unless additional fields are added to the model. Several problems arise. First, to preserve gauge invariance the gauge bosons need to be massless (i.e. the gauge fields must be included without mass terms). However, the $W^{\pm}$ and Z bosons responsible for mediating weak interactions need to have large masses to properly describe the weak force. The fermion masses are also problematic. Weak interactions are found to couple differently to left- and right-handed fermion helicity states. This is accounted for in the SM by treating left- and right-handed fermion states as different fields. Including a fermion mass term in the Lagrangian would break gauge invariance because it would couple these fields. Thus, the fermions also need to be massless, which is inconsistent with observations.

These problems are resolved by the concept of spontaneous symmetry breaking [10–14], in which the true symmetry of the Lagrangian is concealed by an arbitrary choice of an asymmetrical ground state. More specifically, additional spin zero (scalar) fields that couple to electroweak gauge fields are added to the Lagrangian. The fields are chosen such that the zero values do not correspond to the lowest energy state. As a result, the symmetry is broken in the ground state and the scalar fields take on a non-zero value, referred to as the vacuum expectation value. The vacuum expectation value couples to fermion and gauge fields and can give the corresponding particles mass while maintaining gauge invariance.

Spontaneous symmetry breaking also results in the prediction of a neutral, massive scalar boson called the Higgs boson (also called the Higgs, or H). The coupling of the Higgs to fermions in the SM is proportional to the fermion masses. The mass of the Higgs, however, is not fixed in the SM because it depends on an arbitrary symmetry breaking parameter.

Before the turn-on of the Large Hadron Collider the Higgs boson had not been discovered.

On July 4, 2012, the ATLAS and CMS collaborations both announced discoveries of a new particle with a mass near 125 GeV in searches for the SM Higgs [1, 2]. This launched a new era of experimental studies focused on measuring the properties of the new particle. The mass of the particle is currently measured to be $125.09 \pm 0.21(\text{stat}) \pm 0.11(\text{syst})$ GeV [15], where the "stat" denotes the statistical uncertainty and "syst" denotes the systematic uncertainty. All measurements of other properties of the particle are thus far consistent with the hypothesis that the new particle is the SM Higgs, including fermion and boson couplings, production rate, decay width, and spin and CP quantum numbers. Regardless, it is possible that careful measurements of the Higgs properties will reveal departures from the SM.

2.2 Beyond the Standard Model

Despite the success of the SM, there are numerous reasons to think that a complete description of particle interactions will require new physics that goes beyond the SM (BSM). For example, it is assumed that the early universe had an equal composition of matter and antimatter, yet the present universe is composed overwhelmingly of matter. The SM does not fully explain this asymmetry. In addition, neutrinos are required to be massless in the SM but the observations of neutrino oscillations [16] imply that neutrinos have mass. Furthermore, there is overwhelming astronomical evidence for the existence of dark matter [17] and dark energy [18], yet no description of either is included in the SM.

BSM theories are proposed to help explain these shortcomings, in addition to others. Some of these theories predict that the Higgs boson has spin and CP (spin/CP) quantum numbers that differ from the SM values [3, 4]. The SM Higgs is a CP-even scalar with a spin/CP eigenstate of $J^{CP} = 0^+$. Alternate eigenstates interact differently with the $W^\pm$, Z, and γ gauge bosons, and therefore the spin/CP state can be tested by studying $H \to ZZ^*$, $H \to WW^*$, and $H \to \gamma\gamma$ decays. Measurements are done by both ATLAS [19] and CMS [20] to test if the data is compatible with any of the following eigenstates:

- 0^-: CP-odd pseudoscalar
- 0_h^+: CP-even scalar with couplings to higher dimensional operators (this state is explained more clearly later in the section)
- 2^+: CP-even tensor with spin equal to two

Each of these states is found to be excluded in favor of the SM Higgs at a confidence level greater than 99.9% by both ATLAS and CMS. Spin-one eigenstates are forbidden in decays to $\gamma\gamma$ by the Landau-Yang theorem [21, 22], so the observation of the Higgs in $H \to \gamma\gamma$ decays is enough to exclude the spin-one hypothesis. Regardless, this hypothesis is tested in an ATLAS publication [23] using $H \to ZZ^*$ and $H \to WW^*$ decays, and it is excluded at a confidence level greater than 99.7%.

These results indicate that the Higgs spin/CP state is fully compatible with the SM expectation. However, it is possible that the Higgs is scalar with a mixed CP eigenstate [4]. Many extensions of the SM predict a Higgs sector that features multiple neutral Higgs bosons, and in such cases the bosons can be subject to this type of CP-violation. It is important to experimentally test this possibility, which can be done by measuring the tensor structure of HVV interactions, where the V's here correspond to $W^\pm$ or Z bosons.

The HVV interaction can be described in terms of an effective Lagrangian that contains BSM CP-even and CP-odd terms [24]. The Lagrangian for a scalar field H is given by

$$\begin{aligned}\mathcal{L} = \quad & \Big\{\cos(\alpha)\kappa_{\mathrm{SM}}\left[\tfrac{1}{2}g_{HZZ}Z_\mu Z^\mu + g_{HWW}W^+_\mu W^{-\mu}\right] \\ & -\tfrac{1}{4}\tfrac{1}{\Lambda}\left[\cos(\alpha)\kappa_{HZZ}Z_{\mu\nu}Z^{\mu\nu} + \sin(\alpha)\kappa_{AZZ}Z_{\mu\nu}\tilde{Z}^{\mu\nu}\right] \\ & -\tfrac{1}{2}\tfrac{1}{\Lambda}\left[\cos(\alpha)\kappa_{HWW}W^+_{\mu\nu}W^{-\mu\nu} + \sin(\alpha)\kappa_{AWW}W^+_{\mu\nu}\tilde{W}^{-\mu\nu}\right]\Big\} H,\end{aligned} \tag{2.1}$$

where V^μ represents a vector boson field ($V = Z$ or $W^\pm$), $V^{\mu\nu}$ represents a reduced field tensor, and $\tilde{V}^{\mu\nu}$ represents a dual tensor defined as $\tilde{V}^{\mu\nu} = \frac{1}{2}\varepsilon_{\mu\nu\rho\sigma}V^{\rho\sigma}$. The parameters κ_{SM}, κ_{HVV}, and κ_{AVV} are couplings for interactions between particles represented by the H field and ZZ or W^+W^- pairs. More specifically, κ_{SM} is the coupling for a SM scalar, κ_{AVV} is the coupling for a BSM CP-even scalar, and κ_{HVV} is the coupling for a BSM CP-odd scalar. The parameter α represents a CP mixing angle, so that CP-violation is implied when $\alpha \neq 0$ or π (provided the corresponding couplings are non-zero). The parameters g_{HZZ} and g_{HWW} are SM couplings proportional to the squared masses of the Z and W bosons, respectively. By construction, this Lagrangian is only valid up to the energy scale Λ.

Within this framework, a SM Higgs corresponds to the case where $\kappa_{SM} = 1$ and $\kappa_{HVV} = \kappa_{AVV} = \alpha = 0$. For a 0^- boson $\kappa_{AVV} = 1$, $\alpha = \pi/2$, and $\kappa_{SM} = \kappa_{HVV} = 0$. Similarly, for a 0_h^+ boson $\kappa_{HVV} = 1$ and $\kappa_{SM} = \kappa_{AVV} = \alpha = 0$. A CP mixed state corresponds to the case where κ_{AVV} is non-zero along with either or both of the CP-even couplings κ_{SM} or $\tilde{\kappa}_{HVV}$, and α is not 0 or π. Generically, the couplings and mixing angle can have any real value.

This thesis presents a measurement of the scaled coupling ratios $\frac{\tilde{\kappa}_{AVV}}{\kappa_{SM}} \tan\alpha$ and $\frac{\tilde{\kappa}_{HVV}}{\kappa_{SM}}$, where $\tilde{\kappa}_{AVV}$ and $\tilde{\kappa}_{HVV}$ are defined as follows:

$$\tilde{\kappa}_{AVV} = \frac{1}{4}\frac{v}{\Lambda}\kappa_{AVV} \text{ and } \tilde{\kappa}_{HVV} = \frac{1}{4}\frac{v}{\Lambda}\kappa_{HVV}. \tag{2.2}$$

Here v is the vacuum expectation value equal to 246 GeV [25], and the energy scale Λ is set to 1 TeV since there is no evidence of BSM physics below this energy scale. The motivation for the $v/4\Lambda$ factor is to make the coupling ratios compatible with tensor couplings g_4/g_1 and g_2/g_1 in a generic scalar scattering amplitude from an alternate parameterization described in Ref. [3]. In the SM both $\frac{\tilde{\kappa}_{AVV}}{\kappa_{SM}} \tan\alpha$ and $\frac{\tilde{\kappa}_{HVV}}{\kappa_{SM}}$ are approximately zero, although electroweak corrections make small contributions to $\frac{\tilde{\kappa}_{AVV}}{\kappa_{SM}} \tan\alpha$ on the order of 0.1% and to $\frac{\tilde{\kappa}_{HVV}}{\kappa_{SM}}$ on the order of 1%.

The values of these parameters depend on the squared Lorentz invariant four momenta of the V bosons, which means they can be measured by studying the V decays. More details on the variables used can be found in Section 4.1.

In the measurement presented in this thesis it is assumed that the Higgs has a mass near 125 GeV. This is important because it means at least one of the vector bosons produced in the HVV decay is off-shell, which impacts the final state kinematics. It is also assumed that the total decay width width of the Higgs is small with respect to the resolution of the ATLAS detector (below roughly 2 GeV), which is consistent with the theoretical prediction (about 4 keV) and experimental observations.

Chapter 3
The LHC and ATLAS

The Large Hadron Collider (LHC) is host to a number of high energy physics experiments that can be used to test the validity of the SM. This chapter provides a brief introduction to the LHC and the ATLAS detector. More information on the LHC can be found in Ref. [26–28]. Information on the design, construction, and operation of the ATLAS detector can be found in Ref. [29–33]

3.1 LHC

The Large Hadron Collider (LHC) is a super-conducting particle accelerator located at the European Organization for Nuclear Research (CERN) near the city of Geneva, Switzerland. It was constructed between 1998 and 2008, and is currently the largest particle collider in the world. The LHC accelerates particles around a circular 27 km tunnel buried roughly 100 m below ground. A diagram of the machine is shown in Figure 3.1. There are four experiments located at collision points around the LHC ring. This thesis is based on data generated by the ATLAS experiment [29], which is designed to study proton-proton (*pp*) collisions. The CMS experiment [34] is located on the opposite side of the ring and is also designed to study *pp* collisions. The other two experiments are ALICE [35] and LHCb [36]. ALICE is designed to study heavy ion collisions, and LHCb is designed to study physics related to *b*-hadrons.

Before protons are fed into the LHC, they pass through a number of smaller particle accelerators that successively increase their energy. At the beginning of the injection chain, protons from hydrogen atoms are accelerated to an energy of 50 MeV in a linear accelerator called LINAC2. They then enter a synchrotron called the PS Booster, which accelerates them to 1.4 GeV and injects them into the Proton Synchrotron (PS). The PS accelerates the protons to 26 GeV and then passes them into the Super Proton Synchrotron (SPS). Once the protons are accelerated to 450 GeV, they are injected into the main LHC ring. This injection chain produces bunches of protons that travel in opposite directions in separate beam pipes. Super-conducting RF cavities located on a section of the ring (IP4) are designed to accelerate the bunches to an energy 7 TeV. The bunches are bent around the ring by super-conducting dipole magnets that generate magnetic fields up to 8.3 T. The beam pipes are nominally

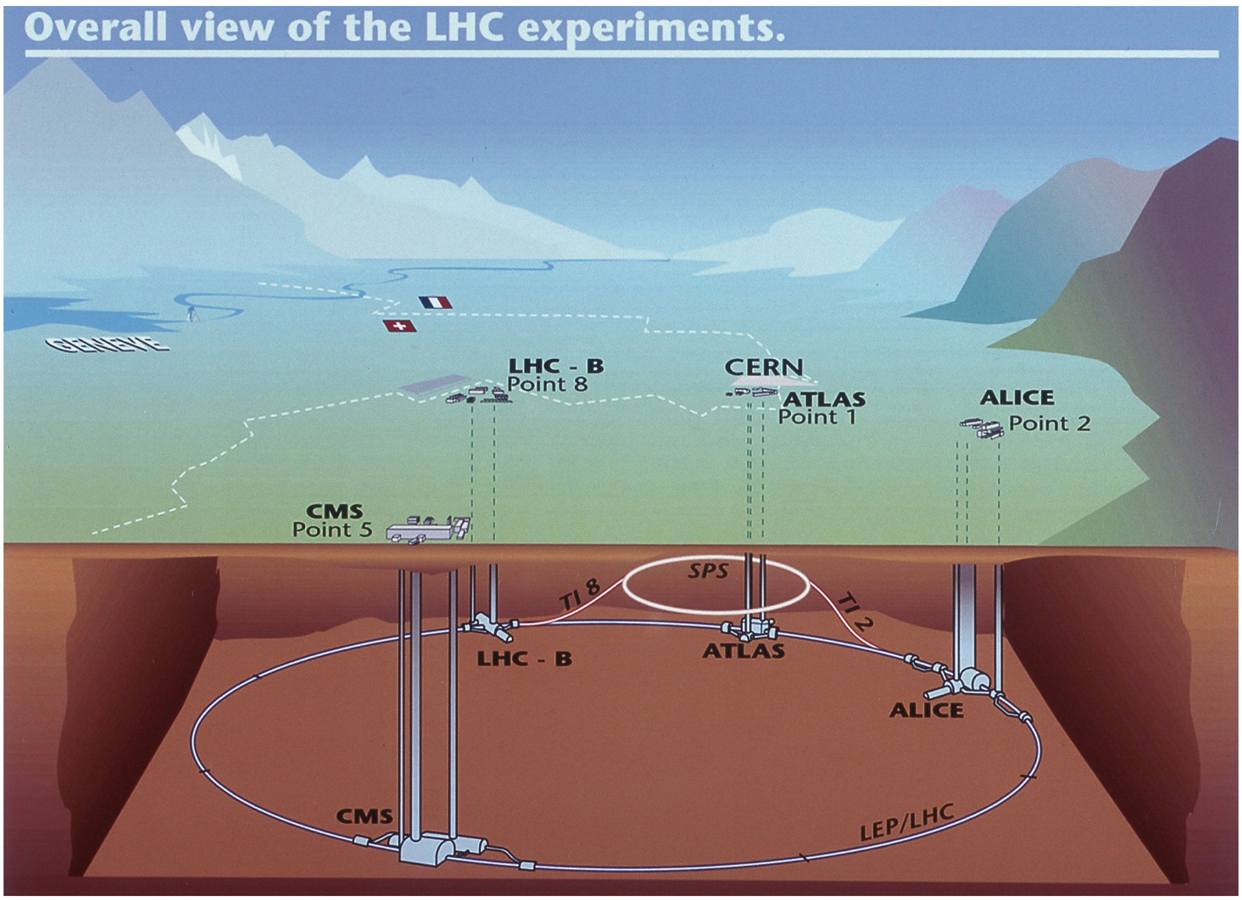

Figure 3.1: Diagram of the LHC and the four experiments constructed around the ring: ATLAS, ALICE, CMS, and LHCb.

designed to contain a total of 2808 bunches, each with roughly 10^{11} protons. However, since the machine has only been in full operation for three years it has yet fully reach the design goals.

The LHC was turned on for the first time in September, 2008. Shortly after it was turned on, a quench occurred in one of the super-conducting dipole magnets and the high current caused a faulty solder connection between magnets to open. An electrical arc ensued, which led to a sudden evaporation of liquid helium. This resulted in an explosion that damaged over 50 magnets. Repairs were finished in 2009. The first LHC run (Run I) took place between 2010 and 2012. In 2010 and 2011 the LHC ran with each beam accelerated to 3.5 TeV, producing collisions up to center of mass energy $\sqrt{s} = 7$ TeV. In 2012 the energy of the beams was increased to 4 TeV, producing collisions up to center of mass energy $\sqrt{s} = 8$ TeV. The machine was shut down in 2013 for modifications and upgrades. The second run (Run II) will begin later in 2015 and produce collisions up to $\sqrt{s} = 13$ TeV. The energy of the beam is important because higher energy collisions can be used to study more massive particles and shorter distances.

Another important characteristic of the beam is luminosity. The *instantaneous* luminosity is proportional to the rate at which collisions are produced by the accelerator, so a beam with a high instantaneous luminosity is capable of producing data at a high rate. Figure 3.2 shows the peak instantaneous luminosity delivered by the LHC in 2010-2012 [37]. The highest instantaneous luminosity was achieved in 2012 at nearly 8×10^{33} cm^{-2} s^{-1}. This can be compared to the design luminosity of 10^{34} cm^{-2} s^{-1}.

If the instantaneous luminosity is integrated over a time window, the result is proportional to the total number of collisions. This is called the *integrated* luminosity and it is used to characterize the total size of a dataset. Figure 3.3 shows the integrated luminosity accumulated over time in 2010-2012 [37]. The LHC runs in 2010 and 2011 with $\sqrt{s} = 7$ TeV generated a total integrated luminosity of roughly 5 fb^{-1}. The full run during 2012 with $\sqrt{s} = 8$ TeV generated roughly 25 fb^{-1}. Both of these datasets are used in this thesis to measure the tensor structure of the Higgs boson.

At collision points, proton bunches are squeezed to a diameter of roughly 16 μm. When two bunches cross it can result in multiple *pp* interactions. This effect, called *pile-up*, is important to take into account when generating simulated data. Figure 3.4 shows a luminosity-weighted distribution of the mean number of interactions per bunch crossing (μ) during 2011

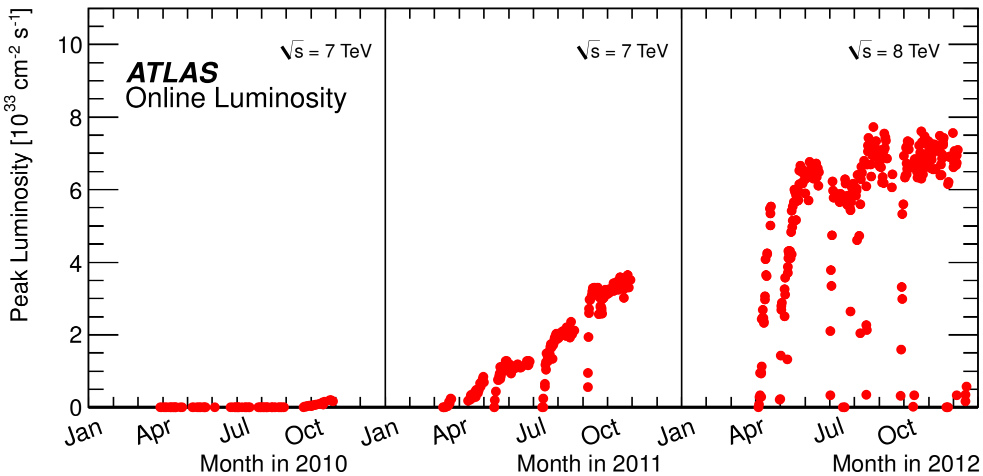

Figure 3.2: Peak instantaneous luminosity for *pp* collisions delivered by the LHC in the years 2010, 2011, and 2012. The periodic dips in luminosity are associated with technical stops of the machine and the introduction of new beam configurations.

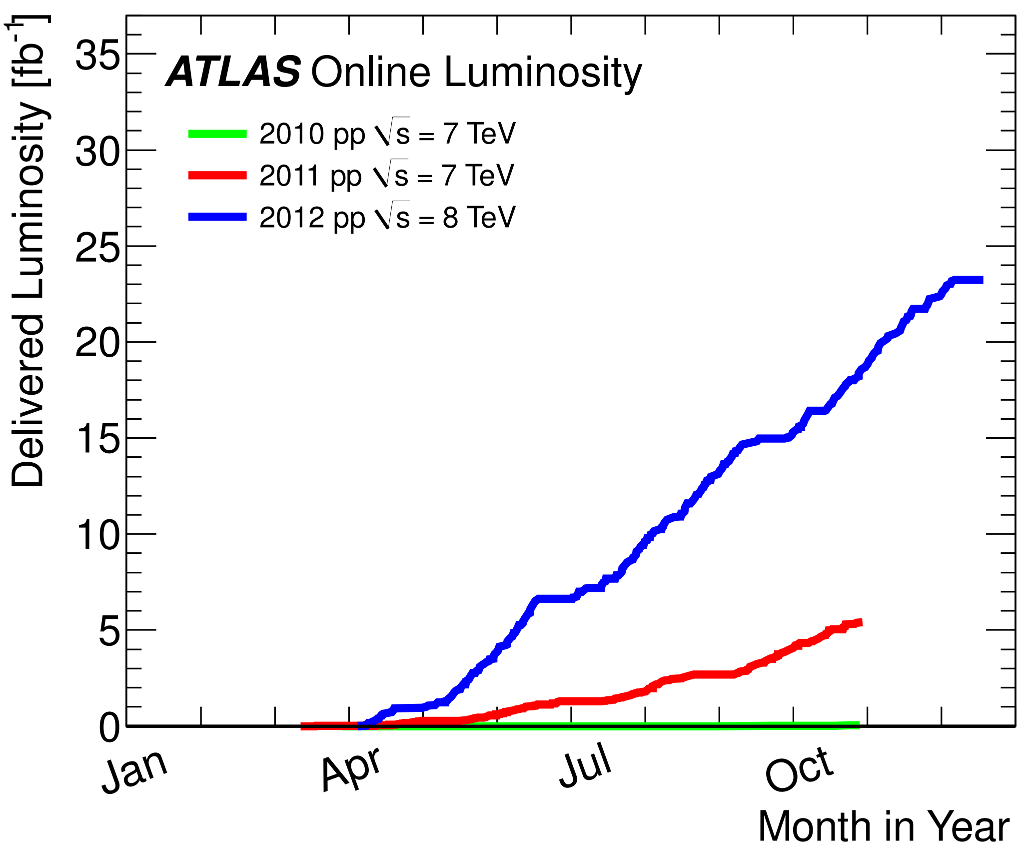

Figure 3.3: Integrated luminosity for *pp* collisions accumulated at the LHC in the years 2010, 2011, and 2012.

and 2012 operation [37]. During the 2012 run the mean number of interactions per bunch crossing was as large as 40. More information on the calculation of μ can be found in Ref. [38].

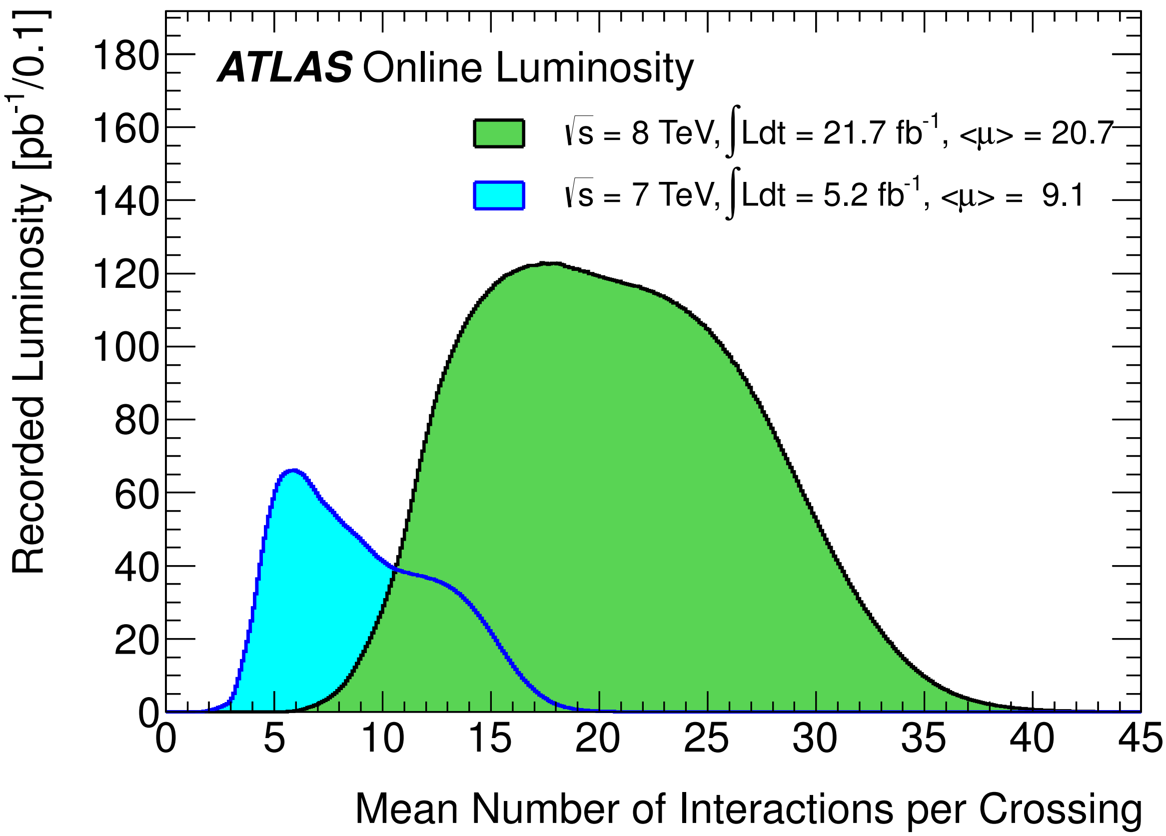

Figure 3.4: The luminosity-weighted distribution of the mean number of interactions per proton bunch (μ) crossing during the 2011 and 2012 LHC runs.

3.2 ATLAS Detector

ATLAS (A Toroidal LHC Apparatus) is a particle detector at the LHC designed to study pp collisions. The detector has a cylindrical shape and is approximately 25 m high and 44 m long, with a weight of roughly 7000 tons. The beam pipe passes through the middle of the detector along the cylindrical axis of symmetry. Collisions occur at the center and produce particles that emerge outward in all directions.

As particles emerge from the collision point, they pass through several different detector layers. Each layer is sensitive to a different class of particles. A diagram with the cross-section of the full detector is shown in Figure 3.5. The inner most layer is called the Inner Detector (ID). This sub-system is designed to reconstruct the trajectories of charged particles. The ID is surrounded by the Electromagnetic and Hadronic Calorimeters, which are designed to measure the energies of electrons, positrons, photons, and hadrons. Surrounding the calorimeters is the Muon Spectrometer (MS), designed to reconstruct muon trajectories.

A right-handed coordinate system is used to characterize particles measured by the ATLAS detector. The z-axis (or longitudinal axis) runs along the beam line, the x-axis points towards the center of the LHC ring, and the y-axis points upward. The origin is defined as the interaction point. The $x - y$ plane perpendicular to the beam line is called the transverse plane. The momentum of particles produced in a collision is conserved in the transverse plane, so the transverse component of momentum, p_{T}, is a commonly used kinematic variable. Longitudinal momentum of the colliding proton consituents is not known, so the conservation of longitudinal momentum is less useful.

Since the ATLAS detector has a cylindrical shape, the Cartesian axes defined above are often converted to an $r - \phi$ coordinate system. In this case, ϕ is the azimuthal angle defined with respect to the x-axis, and r is the transverse distance from the beam line. The polar angle θ with respect to the z-axis is often reported in terms of a Lorentz invariant parameter called pseudorapidity. The pseudorapidity is given by $\eta = -\ln\left[\tan\left(\theta/2\right)\right]$. In the $\eta - \phi$ space, the distance $\Delta R = \sqrt{\Delta\eta^2 + \Delta\phi^2}$ is a Lorentz invariant quantity sometimes used to characterize the separation between particles traversing through the detector.

A detailed description of the ATLAS detector and sub-systems is provided in Ref. [29]. The remainder of this section contains brief overviews of each sub-system.

3.2.1 Inner Detector

The ID is closest to the interaction point, and is used to reconstruct trajectories of charged particles with energies of at least 500 MeV. The detector consists of modular sensors built around the beam pipe with cylindrical symmetry. There are barrel layers centered at the interaction point, in addition to end cap wheels at each end of the barrel that extend the η range. The positions of charged particles are measured with high precision as they traverse the ID layers. All of the ID sensors sit inside a 2 T magnetic field aligned with the beam

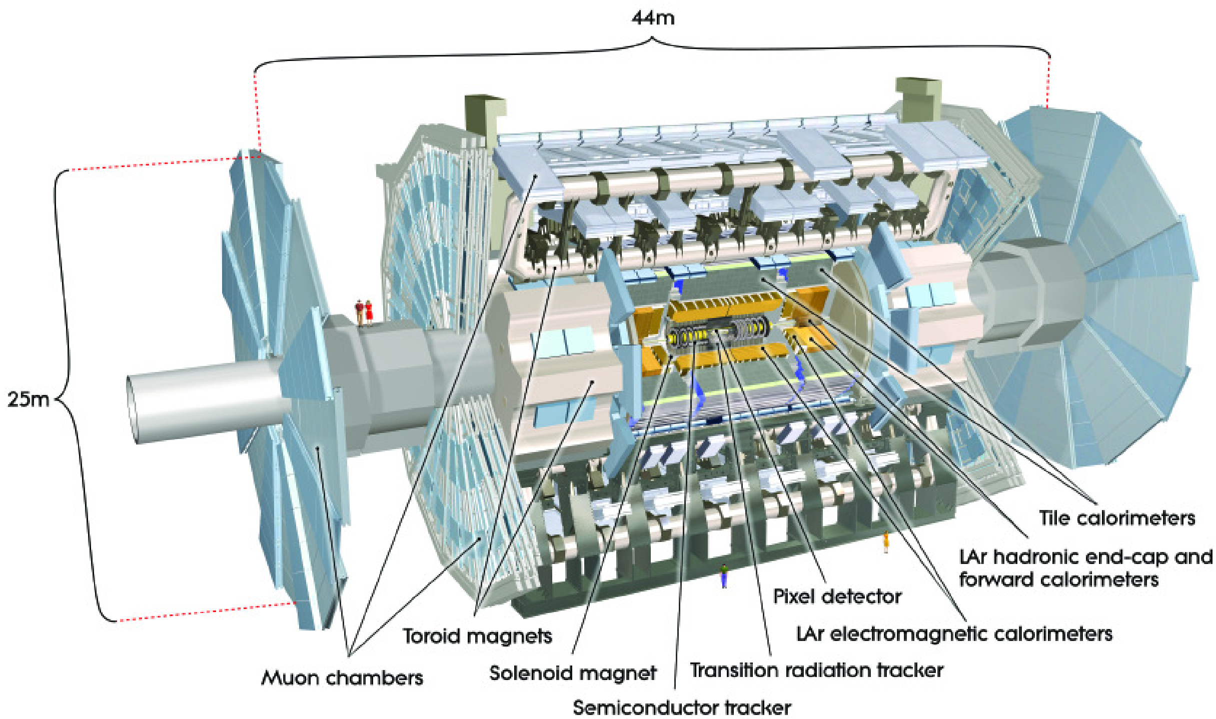

Figure 3.5: Diagram of the ATLAS detector [29].

line, which is generated by a super-conducting solenoid. Charged particles follow helical trajectories as they pass through this field, and the curvature of the trajectories can be used for charge identification and momentum determination.

The ID consists of three sub-systems, as illustrated in Figure 3.6. The inner most sub-system is called the silicon Pixel detector [39, 40]. This component has three layers in the barrel and three layers in each end cap, providing uniform coverage in ϕ for $|\eta| < 2.5$. Each of the layers consists of many silicon sensors or pixels, each 50 by 400 μm. When charged particles pass through the silicon sensors they generate electron-hole pairs that drift in an applied electric field to a readout device. The system contains a total of 80 million readout channels and provides a position resolution of 10 μm in the $r-\phi$ plane, and 115 μm in the z-direction. This level of precision is necessary for resolving dense tracking environments, when many charged particles are produced in collisions.

The Pixel detector is surrounded by the SCT (semiconductor tracker) [41, 42], which consists of four double layers in the barrel and nine layers in each end cap, providing coverage for $|\eta| < 2.5$. The SCT is composed of strips of solid silicon that operate similarly to the

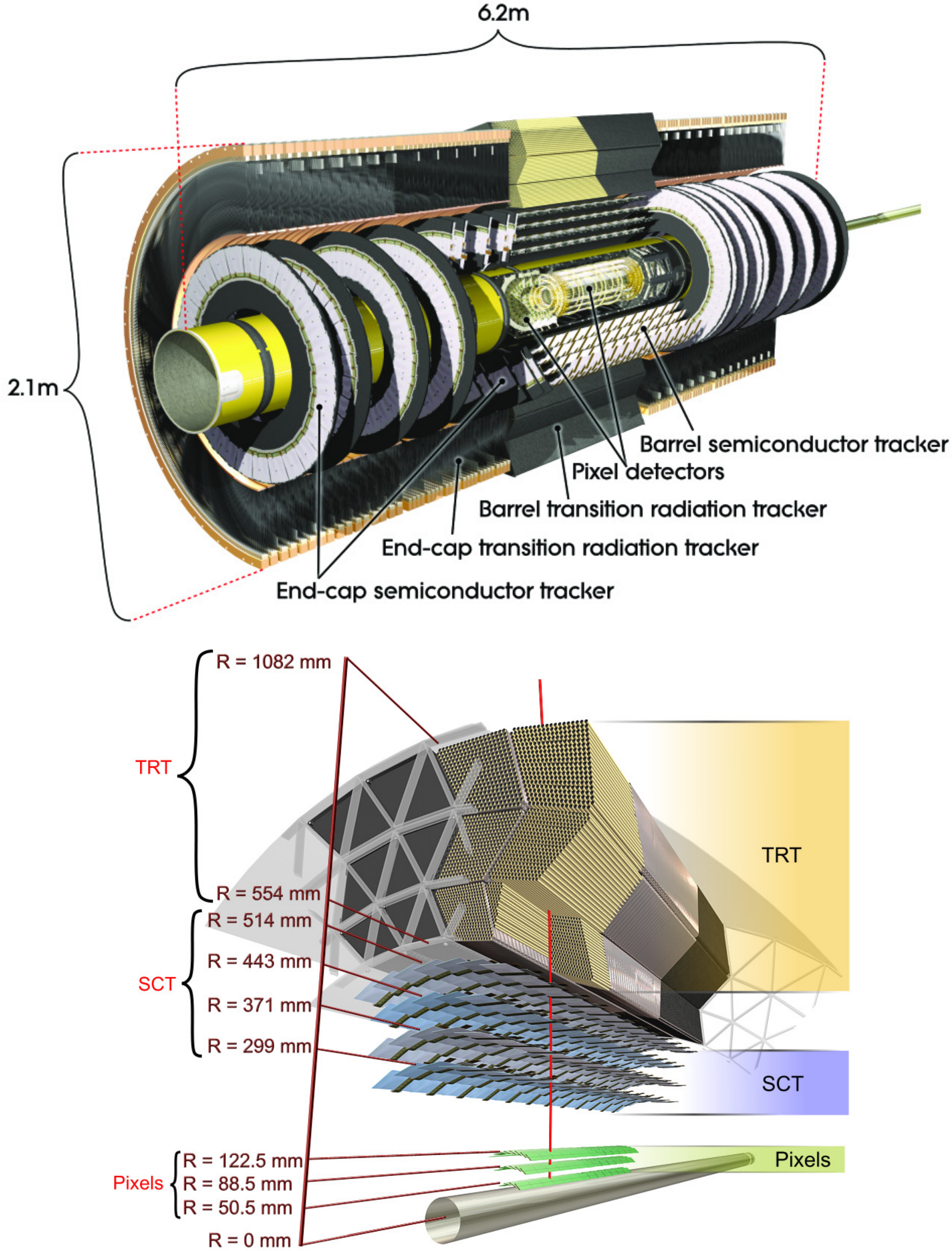

Figure 3.6: Cross-sections of the ATLAS inner detector system [29].

silicon sensors in the Pixel detector. Each strip has a length of 126 mm and a pitch of 80 μm (in the barrel region). The SCT layers are each composed of two sets of silicon strips with axes tilted by 40 mrad with respect to one another. The entire SCT has roughly 60 million readout channels. The pairs of strips locate charged particle positions with an accuracy of 17 μm in the in $r-\phi$ plane, and 580 μm along the z-axis.

The outermost sub-system in the ID, called the TRT (transition radiation tracker) [43], is also the largest. The TRT contains roughly 300,000 straw drift tubes that occupy 70 layers in the barrel and 140 layers in each end cap, providing coverage for $|\eta| < 2.0$. Each straw drift tube contains a gas that is ionized by incident charged particles. The emitted electrons drift in an applied electric field to a wire that runs down the center of the straw to a readout device. A single charged particle will typically register hits in roughly 35 of the straw drift tubes, allowing the particle position to be measured with an accuracy of roughly 130 μm in the $r-\phi$ plane. In addition, the TRT is designed to help with particle identification. As charged particles pass through the TRT they emit transition radiation (TR) photons. The probability of emitting TR photons depends on the Lorentz factor, γ. Thus for particles of a given momentum, electrons will typically emit more photons than charged hadrons. Hence, the number of TR photons detected can be used to discriminate between electrons and charged hadrons.

3.2.2 Calorimeters

The calorimeter system consists of two sub-systems that provide coverage for $|\eta| < 4.9$. A diagram of the sub-systems is shown in Figure 3.7. There is an electromagnetic calorimeter system designed to measure the energy of electrons[1] and photons, and a hadronic calorimeter system designed to measure the energy of hadrons, which are produced in collisions through quark and gluon hadronization. Both systems are classified as non-compensating sampling calorimeters. Incident particles shower in a dense passive material (e.g. lead or iron), and the shower is sampled as it passes through an active detection medium. Detector sensors only recover a fraction of the energy in the shower, but the full energy can be inferred from the observed energy.

1. The electromagnetic calorimeter measures positrons as well as electrons since their showers are almost exactly the same. Positrons are not mentioned explicitly in this section to simplify the text.

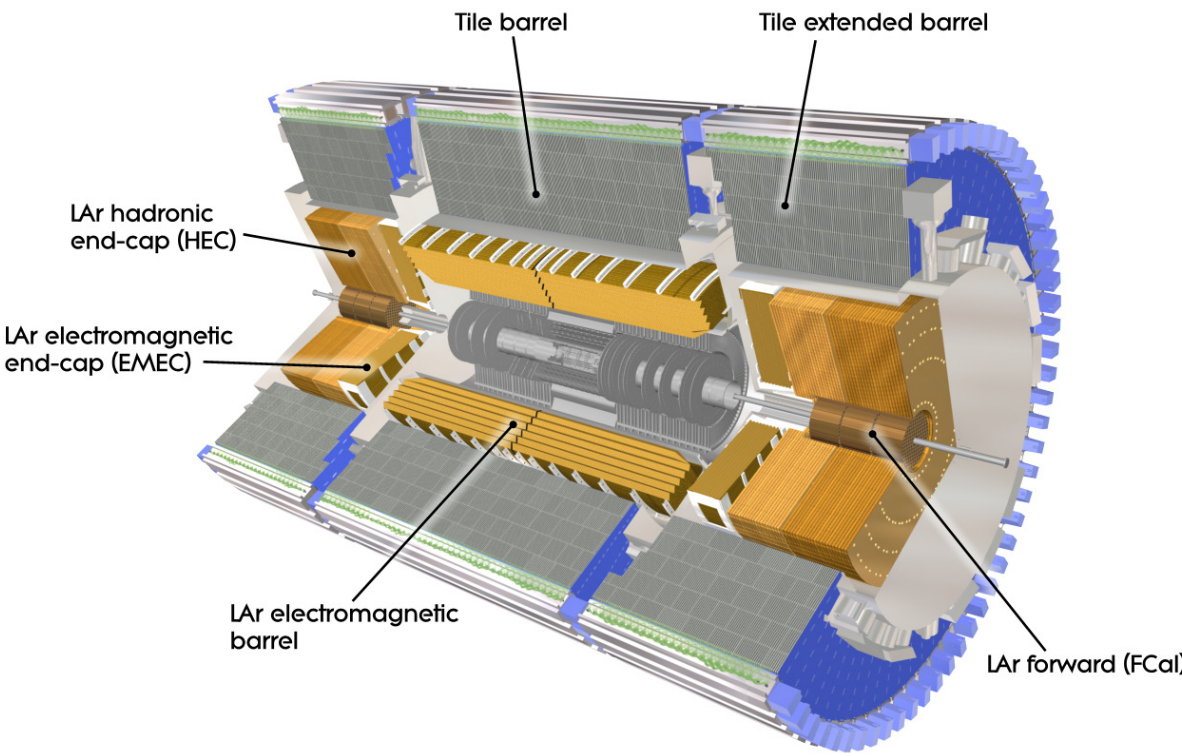

Figure 3.7: Diagram of the ATLAS calorimeter system [29].

The liquid-argon (LAr) electromagnetic (EM) calorimeter sits directly outside the ID and is designed to detect electrons and photons. The calorimeter uses an accordion-like structure of lead as the passive medium. The active medium, LAr, is ionized by charged particles from incident showers and the electrons produced by the ionization are collected on segmented electrodes. The system is divided into a barrel portion that covers the range $|\eta| < 1.475$, and two end cap portions on either side of the barrel covering $1.375 < |\eta| < 3.2$. It is also segmented into three layers with different $\eta - \phi$ granularities as shown in Figure 3.8. The first layer has the finest η segmentation, with an η granularity of 0.003 in the barrel. The second layer has an $\eta - \phi$ granularity of 0.025×0.025 in the barrel, and is responsible for most of the energy measurement. The third layer is coarsely segmented in η but it gives the calorimeter extra depth.

The surrounding calorimeter system known as the hadronic calorimeter is responsible for measuring hadrons that do not shower in the electromagnetic calorimeter. It contains barrel and end cap portions. The barrel portion, called the tile calorimeter, has coverage for $|\eta| < 1.7$. It contains alternating layers of iron as the passive medium and scintillating plastic as the active medium. Each of the cells in the tile calorimeter has an $\eta - \phi$ granularity of roughly 0.1×0.1. The end cap portions of the calorimeter cover the region $1.5 < |\eta| < 3.2$. They use LAr technology similar to the LAr EM calorimeter, but have copper rather than lead as the passive material.

Finally, the LAr forward calorimeters are designed to measure both electromagnetic and hadronic showers. They extend the coverage to $|\eta| = 4.95$.

3.2.3 Muon Chambers

The muon spectrometer (MS) surrounds the calorimeter systems and is designed to measure the trajectories and momenta of muons. It is the outermost detector system of ATLAS. The system contains position sensitive chambers that operate in a 0.5 T toroidal magnetic field that causes charged particles to bend in the $r - z$ plane.

An illustration of the detecting chambers and magnets is shown in Figure 3.9. There is a large barrel toroid, which produces a field that is strongest in the range $|\eta| < 1.4$. There are also smaller toroid magnets in each endcap that produce fields strongest in the range $1.6 < |\eta| < 2.7$. In the range $1.4 < |\eta| < 1.6$, muons are bent by a combination of the barrel

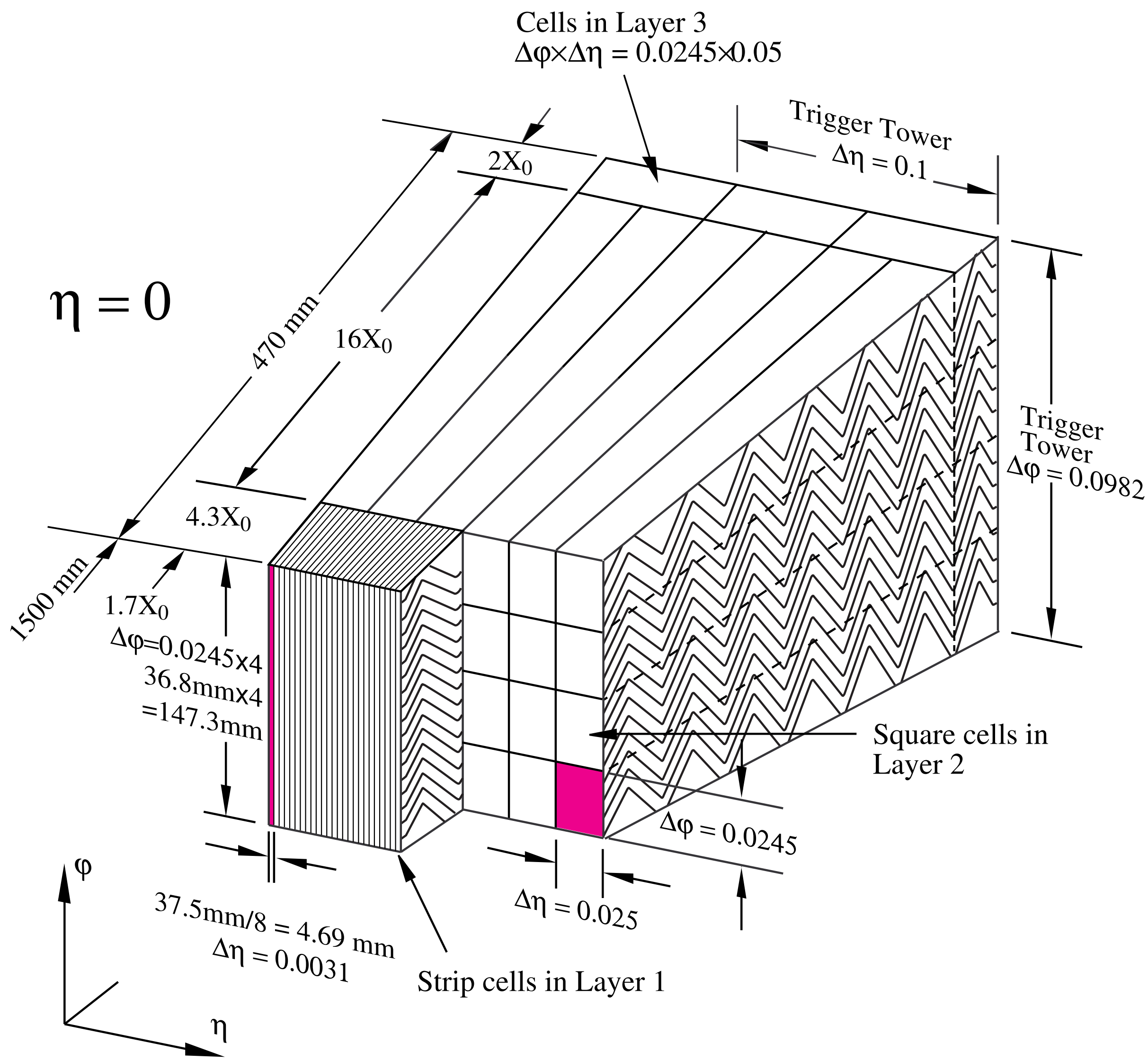

Figure 3.8: Diagram showing the ATLAS EM calorimeter layers in the barrel region [29].

and end cap fields. The detector chambers are arranged into three layers in the barrel, end cap, and transition regions. In the barrel the layers are wrapped cylindrically around the beam axis. In the end caps and transition regions the layers are arranged perpendicular to the beam line.

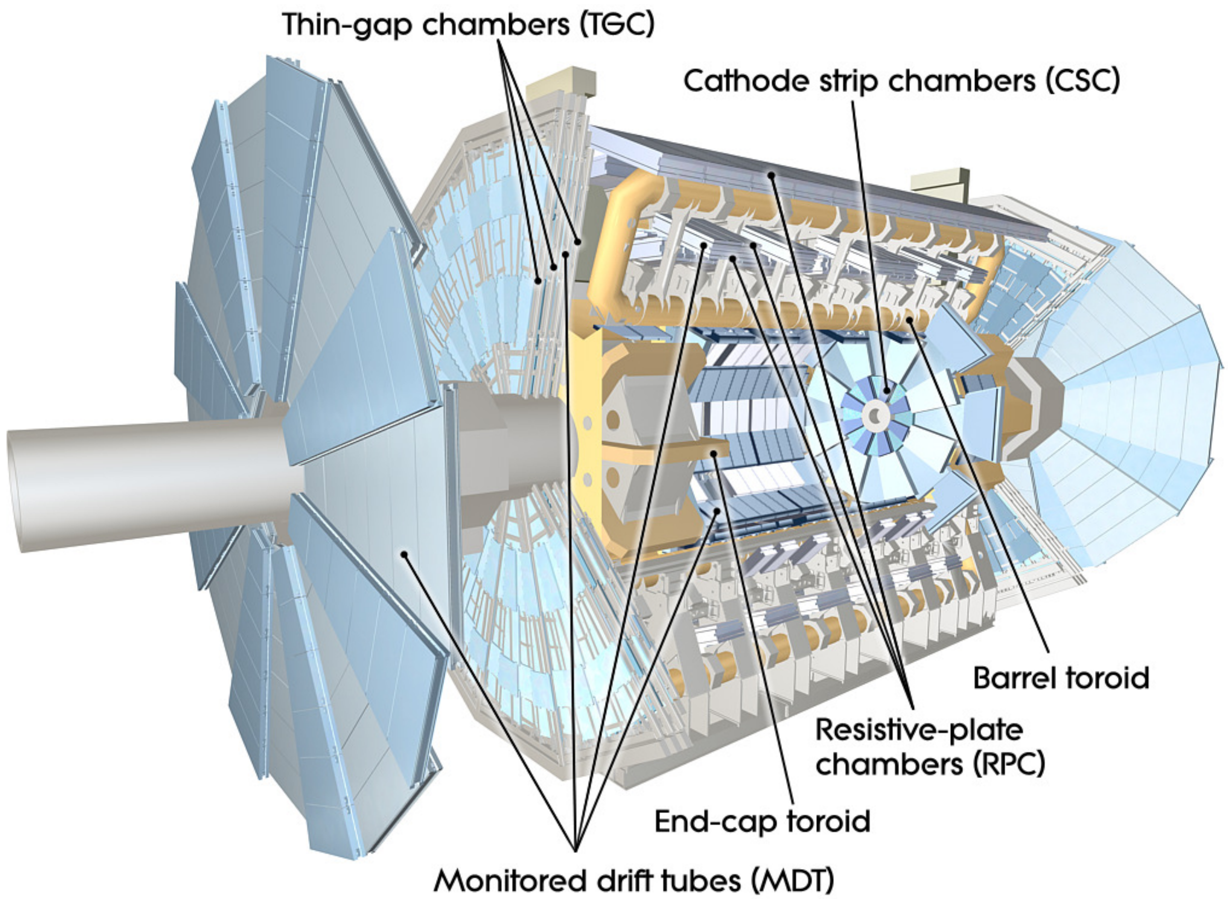

Figure 3.9: Diagram of the ATLAS muon chambers [29].

The MS detector chambers utilize four technologies that each operate by collecting electrons that are produced when incident muons pass through a gaseous mixture. There are Resistive Plate Chambers[44] (RPC) in the barrel that collect charge on parallel resistive plates separated by a small gap. Similarly, the end cap contains Thin Gap Chambers [45] (TGC) consisting of two conducting cathodes separated by a gap, and two parallel wires that collect ionized charge. Both TGC and RPC provide very fast signals for muon hits, and can therefore be used in the ATLAS trigger system to select events containing muons. There are also Muon Drift Tubes [46], which are used over most of the η range, and Cathode Strip

Chambers [47], which are used in the range $2 < |\eta| < 2.7$. These provide track measurements with high spatial resolution.

Chapter 4
HZZ Tensor Structure Analysis

This chapter presents a detailed summary of the analysis for measuring the CP coupling factors characterizing the HZZ vertex. A theoretical background related to this measurement is provided in Chapter 2. The results are in Chapter 5.

The chapter is organized as follows. Section 4.1 contains details related to the $H \to ZZ^* \to 4\ell$ final state. This is followed by a general overview of the analysis method in Section 4.2. Section 4.3 describes the dataset and the simulated datasets that are used for the measurement. Section 4.4 describes the event selection criteria used to clean the data and reduce background. A summary of the statistical method used to make the measurement is given in Section 4.5. The construction of signal and background models is described explicitly in Section 4.6. Systematic uncertainties are summarized in Section 4.7. Finally, a validation check of the asymptotic formulae used to interpret results is given in Section 4.8

4.1 The Four Lepton Final State

The measurement of the Higgs CP-even and CP-odd couplings is done using the $H \to ZZ^* \to 4\ell$ channel. This is considered by some to be the golden channel for studying the Higgs sector because of its clean signature and good invariant mass resolution. The background is dominated by irreducible $q\bar{q} \to ZZ^* \to 4\ell$ decays, with small contributions from $Z+$jets, $t\bar{t}$, and WZ processes. A Feynman diagram for the tree-level t-channel irreducible background decay is given in Figure 4.1. The expected signal-to-background ratio in the $H \to ZZ^* \to 4\ell$ channel is on the order of one (after applying cuts to select signal-like events), which is high compared to other Higgs decay channels.

The main disadvantage of the $H \to ZZ^* \to 4\ell$ channel is that it is a relatively rare decay. The SM Higgs boson branching ratios are shown in Figure 4.2. For a 125.5 GeV Higgs, the branching ratio to ZZ^* is 2.76×10^{-2} [48]. After requiring the decay to four leptons (where leptons are defined here as either electrons or muons) the branching ratio drops to 1.30×10^{-4}. As a result, the total number of events in the four lepton final state is low compared to other Higgs decay channels.

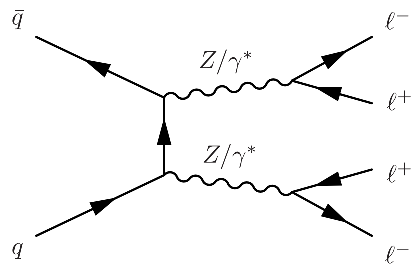

Figure 4.1: Tree-level t-channel diagram for the dominant irreducible $q\bar{q} \to ZZ^* \to 4\ell$ background process.

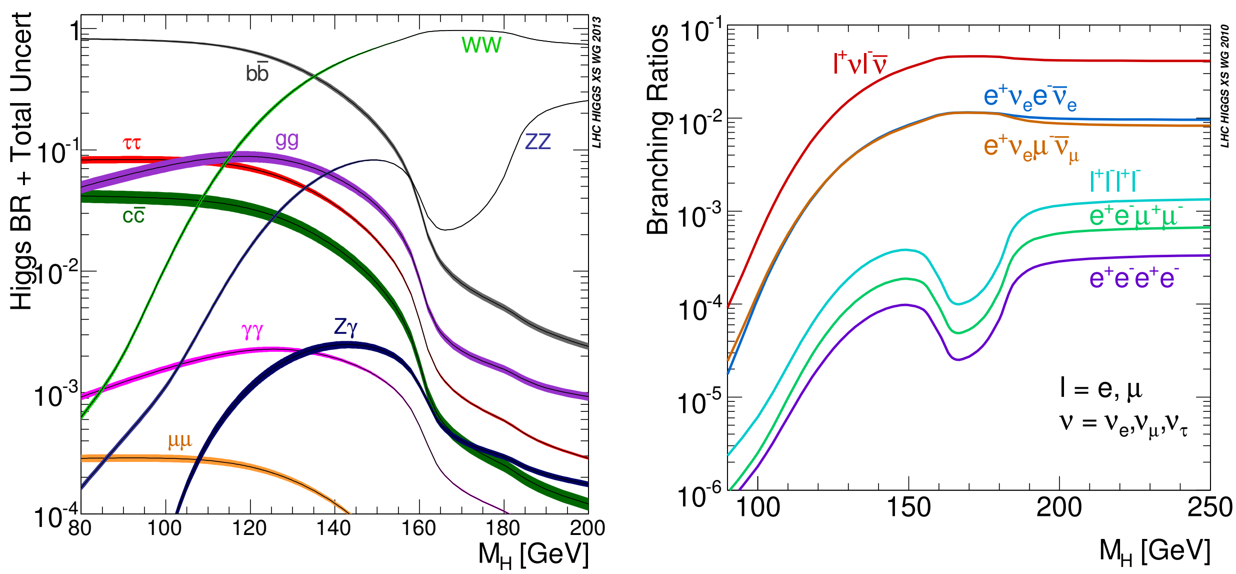

Figure 4.2: SM Higgs boson decay branching ratios as a function of the mass [48]. The branching ratio for the $H \to ZZ^*$ decay is shown on the left in dark blue along with branching ratios for other decays to two gauge bosons or two fermions. The branching ratio for the full $H \to ZZ^* \to 4\ell$ decay is shown on the right in cyan along with other four fermion final states. For reference, the measured mass of the Higgs boson is roughly 125 GeV.

4.1.1 Final State Observables

Four lepton events contain numerous observables that provide sensitivity to the HZZ vertex. In fact, one of the key advantages of working with the $H \to ZZ^* \to 4\ell$ channel is that lepton four vectors can be fully reconstructed by the ATLAS detector. As a result, all of the decay angles that depend on the Spin/CP of the Higgs are accessible. This is not the case for the $H \to WW^* \to \ell\nu\ell\nu$ the channel, for example, because the final state contains two undetected particles (the neutrinos).

Four lepton decays are fully characterized by six decay angles in addition to the invariant mass of the Higgs and the invariant masses of the two Z bosons. The decay angles are illustrated in Figure 4.3 and summarized below using the notation from Ref. [3].

- The angles θ^* and Φ^* (not shown) are the polar and azimuthal angles of the Z boson momentum vectors with respect to the collision axis. These angles are defined in the rest frame of the Higgs (denoted by a generic resonance X in the Figure). The angle Φ^* defines a global rotation in the transverse plane. Since there is no initial state vector in the transverse plane, the production is isotropic in this variable and it is not of interest. The parameter $\cos\theta^*$ is used instead of θ^* in this analysis to match to notation in Ref. [3].

- The angles Φ and Φ_1 are the azimuthal angles of the Z boson decay planes. The angle Φ_1 is the azimuthal angle of the Z_1 decay plane, and Φ is the azimuthal angle between the Z_1 and Z_2 decay planes. These are also defined in the rest frame of the Higgs.

- The angles θ_1 and θ_2 are helicity angles characterizing the Z decays. Each θ_i is defined in the reference frame of the Z_i boson. In Figure 4.3, θ_1 is equal to π minus the angle between the momentum vectors for μ_- and Z_2, and θ_2 is equal to π minus the angle between the momentum vectors for e^- and Z_1. The parameters $\cos\theta_1$ and $\cos\theta_2$ are used instead of θ_1 and θ_2 in this analysis to match the notation in Ref. [3].

The final state observables can be divided into two categories. The observables associated with the decay of the Higgs ($\cos\theta_1$, $\cos\theta_2$, Φ, and the invariant masses of the two Z bosons) depend on the values of the CP coupling factors. The observables associated with the production of the Higgs ($\cos\theta^*$, Φ^*, Φ_1, and the invariant mass of the Higgs) are independent

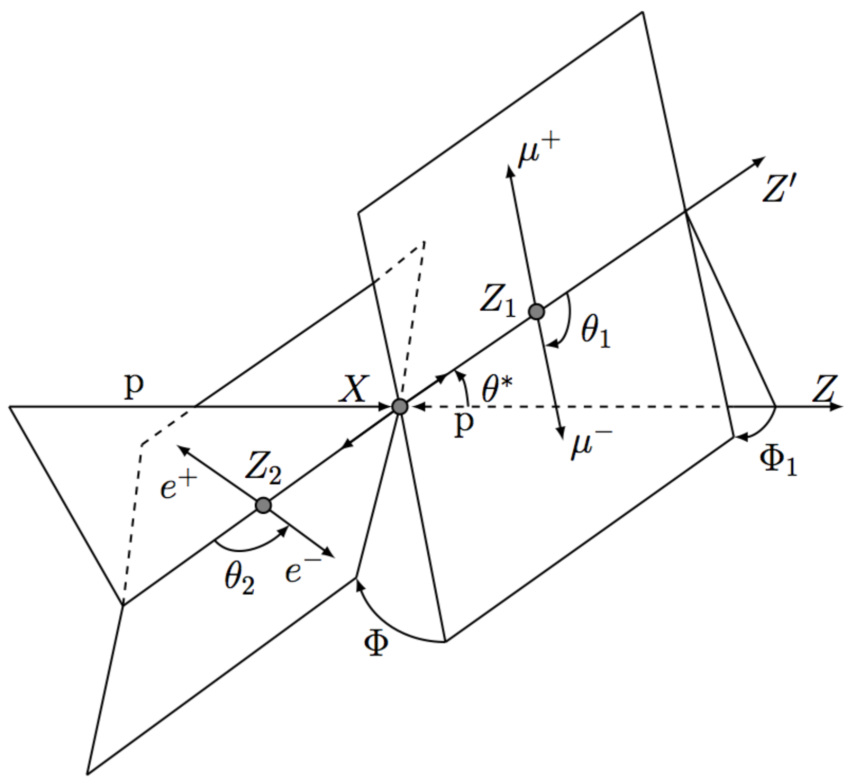

Figure 4.3: Diagram of the production and decay angles in the $H \to ZZ^* \to 4\ell$ decay. The X represents a generic resonance. In the SM, this would be a 0^+ Higgs boson.

of the coupling factors, but they can be useful background discriminants. The the transverse momentum and pseudo-rapidity of the reconstructed Higgs are additional production observables used in this analysis for background discrimination.

4.2 Overview

The rest of this chapter describes the analysis method in detail. A general overview of the method is provided here. The analysis is done using the four lepton final state, which is summarized in the previous section. An event selection is applied to the Run I data to reduce the size of the dataset and to identify events that are consistent with a single resonance decaying to four leptons. This selection is designed to reduce the amount of background, which consists of non-Higgs SM processes that can lead to the reconstruction of four leptons in the detector. There are a total of 45 events in the dataset passing the full event selection.

A model of the final state observables is built using fully reconstructed simulated events that pass the same selection criteria. This model consists of separate components for the signal and background processes. Each component is built from a different simulated dataset. The CP coupling factors, $\frac{\tilde{\kappa}_{AVV}}{\kappa_{SM}} \tan\alpha$ and $\frac{\tilde{\kappa}_{HVV}}{\kappa_{SM}}$, are incorporated in the signal component of the model. In this way, the model describes the distribution of final state observables for any possible CP parameterization. The CP parameters are measured by fitting the full model to unbinned data passing the selection.

Before fitting to data, validation checks are performed to ensure that the method works as expected. This is generally done by fitting to simulated data which has not been used to construct the model and checking that the results are consistent with the expectation. All of the details are given in the following sections.

4.3 Data and Simulated Data

The measurement in this thesis is based on *pp* collision data collected by the ATLAS detector during Run I in 2011 and 2012. The data are categorized into two sub-sets based on the center of mass collision energy. There is a 2011 dataset with center of mass energy $\sqrt{s} = 7$ TeV, and a 2012 dataset with center of mass energy $\sqrt{s} = 8$ TeV. These datasets are summarized in Table 4.1. Events are only used when all relevant parts of the detector are working nominally.

Roughly 94% of the data pass this quality requirement. Separate efficiencies for the 2011 and 2012 datasets are provided in the table. After applying the requirement the 2011 dataset contains a total integrated luminosity of 4.5 fb^{-1}, and the 2012 dataset contains a total integrated luminosity of 20.3 fb^{-1}.

Year	$\sqrt{s}$	Peak luminosity [cm^{-1} s^{-1}]	Pile-up $\langle\mu\rangle$	Data quality efficiency	Integrated luminosity [fb^{-1}]
2011	7 TeV	3.65×10^{33}	9.1	90%	4.5
2012	8 TeV	7.73×10^{33}	20.3	95%	20.3

Table 4.1: Summary of the 2011 and 2012 ATLAS datasets used for the measurement.

4.3.1 Signal Monte Carlo

Monte Carlo (MC) events are generated to simulate the production and decay of the Higgs boson using a combination of event generators. The parton interaction producing the Higgs is simulated at next-to-leading order (NLO) using the PowHeg generator and AU2_CTEQ6L1 parton distribution functions. The p_{T} distribution from PowHeg at generator level currently has the best agreement with the theoretical p_{T} distribution evaluated at next-to-next-to-leading logarithm (NNLL) and NLO [49]. The decay of the Higgs to four leptons is simulated using the JHU v.4.2.1 generator [3], which is derived from the generic scattering amplitude introduced in Chapter 2. The Pythia8 generator is used to model parton showers as well as initial and final state radiation. Interactions of the final state particles with the detector are simulated using Geant4 [50], and events are reconstructed with the ATLAS Athena software. Interference in final states with same-flavor leptons is included in the JHU model. The effect of interference is validated against the MadGraph and Prophecy4F generators, and differences are found to be negligible.

A variety of signal samples corresponding to different CP-even and CP-odd coupling configurations are generated. Table 4.2 lists the signal samples used for this analysis. Each sample is produced assuming the mass of the Higgs is 125.5 GeV. The parameters in the table are given in the JHU notation from Ref. [3] because the Higgs decay is simulated using the JHU generator. The configuration $g_1 = g_2 = g_4 = 1$ in the table corresponds to $\frac{\tilde{\kappa}_{AVV}}{\kappa_{SM}} \tan\alpha = \frac{\tilde{\kappa}_{HVV}}{\kappa_{SM}} = 1$ in an effective Lagrangian. Similarly, the configuration with

($g_1 = 1, g_2 = g_4 = 1+i$) corresponds to $\frac{\tilde{\kappa}_{HVV}}{\kappa_{SM}} = \frac{\tilde{\kappa}_{AVV}}{\kappa_{SM}} \tan\alpha = 1+i$. In the JHU framework the tensor couplings g_1, g_2, and g_4 are allowed to be complex, but this corresponds to a non-Hermitian effective Lagrangian. Thus, the sample with complex couplings is reweighted using a procedure described below to remove the imaginary contributions before it is used in the analysis. This sample contains the most events so it is used to construct the probability model for the measurement (details follow in Section 4.6.1). The other two samples in the table are used for validation.

Sample coupling configuration	$\sqrt{s}$	Events generated
SM 0^+ Higgs	7 TeV	500,000
SM 0^+ Higgs	8 TeV	500,000
$g_1 = g_2 = g_4 = 1$	7 TeV	400,000
$g_1 = g_2 = g_4 = 1$	8 TeV	400,000
$g_1 = 1, g_2 = g_4 = 1+i$	7 TeV	2,940,000
$g_1 = 1, g_2 = g_4 = 1+i$	8 TeV	3,000,000

Table 4.2: List of the signal MC samples used in analysis. The decay of the Higgs to four leptons is simulated using the JHU generator, so the coupling configurations are written using the JHU notation in Ref. [3]. The corresponding values in the effective Lagrangian notation are provided in the text.

To measure the CP-even and CP-odd couplings of the HZZ vertex it is useful to have simulated data corresponding to any possible coupling configuration. Fortunately a single base sample can be reweighted to any target coupling configuration by assigning a weight to each event equal to

$$w_i = \frac{|\mathcal{M}(\boldsymbol{x}_i|\text{target couplings})|^2}{|\mathcal{M}(\boldsymbol{x}_i|\text{base couplings})|^2}, \tag{4.1}$$

where $\mathcal{M}$ is the matrix element and $\boldsymbol{x}_i$ contains the generator-level four-vector for all four final state leptons in event i. The matrix element is calculated at LO using JHUGen v4.2.1 [3]. Some validation checks for this method are provided at the end of Section 4.4 after the event selection is defined.

4.3.2 ZZ^* Background Monte Carlo

The largest background associated with $H \to ZZ^* \to 4\ell$ signal is due to non-resonant SM $ZZ^* \to 4\ell$ decays. This is an irreducible background with the same final state as the signal. MC events are produced using the PowHeg generator to estimate the ZZ^* background. Parton showers and initial/final state radiation are modeled using Pythia8. A generator-level filter is applied to remove events that do not have an invariant four lepton mass between 100 and 150 GeV. Event reconstruction is done using the full simulation of the ATLAS detector and trigger. Table 4.3 lists the ZZ^* background samples that are used in this analysis.

Sample final State	$\sqrt{s}$	Events generated
$4e$	7 TeV	2,000,000
4μ	7 TeV	2,000,000
$2e$ and 2μ	7 TeV	3,995,000
$4e$	8 TeV	2,145,000
4μ	8 TeV	2,150,000
$2e$ and 2μ	8 TeV	4,295,000

Table 4.3: List of the ZZ^* background samples used in the analysis. Separate samples are generated for final states with different leptons flavors. For example, the "$2e$ and 2μ" final state corresponds to the case where one Z boson decays to e^+e^- and the other Z boson decays to $\mu^+\mu^-$

4.3.3 Reducible Background Estimation

Reducible background associated with $H \to ZZ^* \to 4\ell$ signal comes from $Z+$jets, $t\bar{t}$, and WZ. These processes can leak into the signal region if there are fake or non-isolated leptons in the final state, but they make a relatively small contribution to the total background. Monte Carlo samples are generated for each of these processes and data-driven techniques are used to estimate the number of events passing the event selection requirements.

MC samples for the $Z+$jets background are generated using the ALPGEN generator [51] interfaced with Pythia8 for modeling hadronization and parton showers. The production is divided into two categories. There is a $Z+$light jets sample, which is dominated by events where a Z boson is produced along with light u, d, or s quarks. This sample also includes Zcc events where the c is approximated to be massless and Zbb events where the b quarks are produced in parton showers. The second sample is a pure Zbb sample, which incorporates matrix element calculations that take into account the mass of the b quark. The overlap between these two samples is removed using the MLM matching scheme [52]. MC for the $t\bar{t}$ background is generated using PowHeg interfaced with Pythia8 for hadronization and parton showers. The Photos [53] generator is used to incorporate radiative corrections from quantum electrodynamics. Finally, WZ MC samples are generated using Sherpa [54]. All of these background samples are reconstructed using the full ATLAS simulation.

The relative contributions from each of the reducible background components are determined using data-driven methods. This is done with the following general procedure. The reducible background composition (both in data and MC) is studied in control regions, which are dominated by a given background process yet kinematically similar to the signal region. These regions are defined by inverting or relaxing event selection or lepton identification requirements. The expected background composition in the signal region is then computed by extrapolating from the control regions to the signal region using transfer factors, which are typically calculated by MC based on the efficiency of the inverted or relaxed criteria. The relative contributions from the reducible background components vary depending on the flavor of the low p_{T} leptons in the final state. Thus, different methods are used depending on whether the reconstructed sub-leading Z decays to a pair of electrons or muons. Detailed descriptions of both methods can be found in Ref. [55].

4.4 Event Selection

A series of selection requirements are used to clean the dataset before it is used for the measurement. The selection is applied to both data and reconstructed MC. Events are required to satisfy a trigger designed to identify at least one or two lepton candidates in the final state. The lepton candidates in each passing event are then reconstructed and required to some pass some quality criteria. Additional cuts based on the final state kinematics are then used to define a signal region with reduced noise from background. These selections are summarized in the following three sections. More details on the trigger requirements, lepton reconstruction, and event selection can be found in Ref. [55].

4.4.1 Trigger

The ATLAS trigger system is used to identify potentially interesting events before they are saved to disk. This is done using kinematic information from preliminary online object reconstruction. The events used in this analysis are required to satisfy either a single lepton trigger designed to identify at least one lepton candidate, or a di-lepton trigger designed to identify at least two lepton candidates.

The triggers used depend on the data-taking period, mainly through the luminosity, and the final state lepton flavors. The list of ATLAS trigger names is given in Table 4.4. For the 2012 dataset, the single lepton triggers have a p_{T} threshold of 24 GeV. The di-lepton triggers are capable of handling lower p_{T} thresholds between 8 and 24 GeV. Some of the single lepton triggers used in 2012 have an extra isolation cut (denoted by an "i" in the trigger name), which requires that the sum of the p_{T} of tracks with $p_{\mathrm{T}} > 1$ GeV in a cone of radius $R = 0.2$ around the lepton candidate must be less than 10% of the lepton p_{T}. For the 2011 dataset the single lepton triggers have a minimum p_{T} threshold of 18 GeV, and the di-lepton triggers have p_{T} thresholds between 6 and 12 GeV. Different triggers are used for the different data-taking periods labeled B through M.

4.4.2 Lepton Identification

Lepton candidates in each event are required to pass a series of quality cuts before they are identified as electrons or muons. The electron identification requirements help reduce the background due to hadronic jets faking electrons, non-isolated electrons, and electrons produced by photon conversions. Muon identification requirements help reduce background from muons produced by heavy flavor jets.

In general, electron candidates are required to have well-reconstructed ID tracks that point to a cluster in the EM calorimeter. The quality criteria are based on variables that provide good separation between isolated electrons and jets. For the 2012 dataset, identification is done using a multivariate maximum likelihood technique. This allows multiple variables to be evaluated simultaneously when making an identification decision. For the 2011 dataset, the identification is done using a simpler rectangular cut-based technique. The cuts are optimized separately in 10 η bins across the EM calorimeter and 11 E_{T} bins ranging from 5 to 80 GeV.

Data Period	Final State	ATLAS Trigger Names
2011 B-I	$4e$	EF_e20_medium OR EF_2e12_medium
	4μ	EF_mu18_MG OR EF_2mu210_loose
	$2\mu 2e$, $2e2\mu$	$4e$ OR 4μ OR EF_e10_medium_mu6
2011 J	$4e$	EF_e20_medium OR EF_2e12_medium
	4μ	EF_mu18_MG_medium OR EF_2mu210_loose
	$2\mu 2e$, $2e2\mu$	$4e$ OR 4μ OR EF_e10_medium_mu6
2011 K	$4e$	EF_e22_medium OR EF_2e12T_medium
	4μ	EF_mu18_MG_medium OR EF_2mu210_loose
	$2\mu 2e$, $2e2\mu$	$4e$ OR 4μ OR EF_e10_medium_mu6
2011 L-M	$4e$	EF_e22vh_medium1 OR EF_2e12Tvh_medium
	4μ	EF_mu18_MG_medium OR EF_2mu210_loose
	$2\mu 2e$, $2e2\mu$	$4e$ OR 4μ OR EF_e10_medium_mu6
2012	$4e$	e24vhi_medium1 OR e60_medium1 OR 2e12Tvh_loose1 OR 2e12Tvh_loose1_L2StarB
	4μ	mu24i_tight OR mu36_tight OR 2mu13 OR mu18_mu8_EFFS
	$2\mu 2e$, $2e2\mu$	$4e$ OR 4μ OR e12Tvh_medium1_mu8 OR e24vhi_loose1_mu8

Table 4.4: Summary of the ATLAS trigger configurations used to select events in the signal region. The configuration varies depending on the data-taking period and final state. The 2011 data is divided into periods B through M with generally increasing peak luminosity. The 2012 data is all considered to be part of a single period. The triggers listed for each final state are OR'd together. Mixed flavor final states incorporate the 4μ and $4e$ triggers in addition to one or two triggers designed to select events with electron-muon pairs. The triggers with "2e" or "2mu" in the title are designed to select events with single flavor lepton pairs.

Muons are identified using a so-called STACO algorithm [56] that utilizes information from the MS, ID, and EM calorimeter. ATLAS defines four types of muon candidates that differ in how they are reconstructed. All four are used in this analysis. Each type is explained below:

Combined muons (CB): Tracks in the MS are combined with tracks in the ID.

Segment tagged muons (ST): Tracks in the ID are used if they can be extropolated to tracks in the MS.

Stand-alone muons (SA): Tracks in the MS are extrapolated to the interaction point, taking into account the effects from multiple scattering and energy loss in the calorimeters. The type of reconstruction is used in this analysis for the region $2.5 < |\eta| < 2.7$ to increase the overall acceptance by extending to the acceptance boundary of the MS.

Calorimeter tagged muons (CT): Tracks in the ID are combined with energy depositions in the calorimeters that are consistent with minimum ionization. This reconstruction is optimized for muons with $p_{\mathrm{T}} > 15$ GeV. Calorimeter tagged muons are used in this analysis for the region $|\eta| < 0.1$ where there are no muon chambers.

4.4.3 Event Selection

An event selection is used to select events that are compatible with the $H \to ZZ^{*} \to 4\ell$ decay. The selection is based entirely on lepton candidates; there are no requirements for reconstructed jets or missing energy[1]. Candidate lepton quadruplets are identified in each event by selecting all possible sets of two opposite sign same flavor lepton pairs. Then each quadruplet is required to pass a series of kinematic cuts. All four leptons in the quadruplet must have a longitudinal distance $|z_0| < 10$ mm from the primary vertex in the event. The primary vertex is defined as the vertex with at least three associated tracks that has the highest $\sum p_{\mathrm{T}}^2$, where the sum is over tracks that are associated with the vertex. To reduce background from cosmic rays, the distance from the primary vertex in the transverse plane,

1. There is one exception to this rule. Photon candidates are sometimes used to reconstruct final state observables if they appear to be radiated from final state leptons. This method is described later in this section.

d_0, must satisfy must also satisfy $|d_0| < 1$ mm for all leptons in the quadruplet. The distance d_0 is sometimes called the impact parameter.

Muons in each quadruplet are required to have $p_\mathrm{T} > 6$ GeV and $|\eta| < 2.7$. Electrons are required to have $E_\mathrm{T} > 7$ GeV and $|\eta| < 2.47$. Furthermore, the highest, second highest, and third highest p_T leptons must satisfy $p_\mathrm{T} > 20$, 15, and 10 GeV, respectively. Each quadruplet is allowed to have only one SA and one CT muon. SA muons are only considered if they have $|\eta| > 2.5$ and CT muons are only considered if they have $|\eta| < 0.1$ and $p_\mathrm{T} > 15$ GeV. Since CT muons can be faked by electrons depositing energy in the calorimeter, they are rejected if they share an ID track with an electron. The leptons in each quadruplet are required to be well-separated. Same flavor leptons must be separated by a distance $\Delta R > 0.1$, and different flavor leptons must be separated by $\Delta R > 0.2$.

The invariant masses are then calculated for the di-leptons in each quadruplet. The di-lepton with mass closest to the Z pole is called the leading di-lepton (or the leading Z), and is required to have a mass m_{12} between 50 and 106 GeV. The other di-lepton with a mass farther from the Z pole is called the sub-leading di-lepton (or the sub-leading Z), and is required to have a mass m_{34} between 12 and 65 GeV. If an event has more than one quadruplet satisfying all of these criteria, then the one with m_{12} closest to the Z pole is retained. If there are multiple quadruplets with the same value for m_{12}, then the one with the highest m_{34} is selected. The selected quadruplet must have a combined four lepton mass, $m_{4\ell}$, that is between 115 and 130 GeV.

Some additional isolation requirements are then applied to the selected quadruplet using discriminants called the normalized track isolation and the normalized calorimetric isolation. The normalized track isolation is defined as the p_T sum of tracks in a cone of $\Delta R < 0.2$ around the lepton divided by the lepton p_T. Tracks are only included in this sum if they satisfy basic quality criteria. For electrons, tracks must have at least nine hits in the Pixel and SCT detectors (silicon hits), a hit in the inner most Pixel layer, and $p_\mathrm{T} > 0.4$ GeV. Note that the maximum number of possible silicon hits in the barrel region is 11 (three in the Pixel detector and eight in the SCT), which means there can be a maximum of two missing hits. For muons the tracks must have at least four silicon hits and $p_\mathrm{T} > 1$ GeV. The tracks associated with any of the leptons in the quadruplet (including the lepton itself) are excluded from the sum. Both electrons and muons are required to have a normalized track isolation below 0.15. The normalized calorimetric discriminant is defined similarly but using energy deposits in the calorimeter instead of tracks. For muons it is defined as the E_{T} sum of calorimeter cells in a cone of radius $R = 0.2$ divided by the muon p_{T}. For electrons it is defined as the E_{T} sum of topological clusters in a cone of radius $R = 0.2$ divided by the electron p_{T}. In both cases, the energy depositions from leptons in the quadruplet are excluded from the sum. Muons and electrons are required to have normalized calorimeter isolations below 0.3 and 0.2, respectively.

Finally, a cut is placed on the significance of the impact parameter, defined as d_0/σ_{d_0}. This value is required to be below 3.5 for muons and 6.5 for electrons. The higher cut is used for electrons because electrons are affected more by bremsstrahlung.

Events passing the selection are categorized based on the lepton flavors in the final state. The 4μ and $4e$ categories contain events that have four muons and four electrons, respectively. The $2\mu 2e$ category contains events where the leading di-lepton consists of muons and the sub-leading di-lepton consists of electrons. Similarly, the $2e2\mu$ category contains events where the leading di-lepton consists of electrons and the sub-leading di-lepton consists of muons.

Final State Radiation Recovery

Leptons in $H \to ZZ^* \to 4\ell$ decays can lose energy by radiating low E_{T} photons. This process is called Final State Radiation (FSR). When FSR photons are neglected in the signal, the reconstructed $m_{4\ell}$ is more likely to fall below the 115 GeV signal region threshold. Since this process is modeled well by Pythia8, FSR photons can be identified and incorporated into the four lepton measurement to recover some signal events.

The identification of FSR photons is divided into two searches. There is a collinear search that is used only for muons, and a non-collinear search used for both muons and electrons. Details can be found in Refs. [57] and [55]. The collinear search looks for clusters in the LAr calorimeter satisfying $\Delta R_{\mathrm{cluster},\mu} < 0.08$ and 1.5 GeV $< E_{\mathrm{T,cluster}} <$ 3.5 GeV, where $E_{\mathrm{T,cluster}}$ is the transverse energy of the cluster calculated with respect to the beams. It also includes fully reconstructed photons satisfying $\Delta R_{\gamma,\mu} < 0.15$ and $E_{\mathrm{T},\gamma} >$ 3.5 GeV. If a collinear photon is found near a muon within a cone of radius $R = 0.05$, then 400 MeV of energy is removed from the photon to account for the average contribution from muon ionization. The non-collinear search includes fully reconstructed photons that are isolated and have $\Delta R_{\gamma,\ell} > 0.15$ and $E_{\mathrm{T},\gamma} >$ 10 GeV.

FSR recovery is only allowed for one photon per event. The photon must be associated with one of the leptons from the leading Z decay. If the leading Z decays to muons then priority is given to the highest E_{T} collinear photon provided that 66 GeV $< m_{\mu\mu} <$ 89 GeV and $m_{\mu\mu\gamma} <$ 100 GeV. If the leading Z decays to electrons or if no collinear photons satisfy these requirements, then the highest E_{T} non-collinear photon is used as long as $m_{\ell\ell} <$ 80 GeV and $m_{\ell\ell\gamma} <$ 100 GeV. These mass cuts are designed to remove background from Initial State Radiation (ISR), neutral pions, and muon ionization. They are applied to both data and MC events. FSR photons satisfying these requirements are identified in 4.5% (0.4%) of the signal MC events in the 4μ ($4e$) final state passing the nominal event selection but with a looser $m_{4\ell}$ window between 90 and 140 GeV. After applying the nominal $m_{4\ell}$ window cut between 115 and 130 GeV, FSR recovery causes the signal yield to increase by 1.1% (0.3%) in the 4μ ($4e$) final state.

Z Mass Constraint

The leading di-lepton is predominantly produced by the decay of an on-shell Z in signal events. This information can be exploited to constrain the measurement of the di-lepton mass and thereby improve the mass resolution. The constraint is incorporated using a maximum likelihood fit technique that is summarized below.

The likelihood for observing a di-lepton with true four-momenta $(\mathbf{p}_1^{\mathrm{true}}, \mathbf{p}_2^{\mathrm{true}})$ and reconstructed four-momenta $(\mathbf{p}_1^{\mathrm{reco}}, \mathbf{p}_2^{\mathrm{reco}})$ is given by

$$\begin{aligned} L(\mathbf{p}_1^{\mathrm{true}},&\mathbf{p}_2^{\mathrm{true}}, \mathbf{p}_1^{\mathrm{reco}}, \mathbf{p}_2^{\mathrm{reco}}) = \\ &B(\mathbf{p}_1^{\mathrm{true}}, \mathbf{p}_2^{\mathrm{true}}) \times R_1(\mathbf{p}_1^{\mathrm{true}}|\mathbf{p}_1^{\mathrm{reco}}) \times R_2(\mathbf{p}_2^{\mathrm{true}}|\mathbf{p}_2^{\mathrm{reco}}), \end{aligned} \tag{4.2}$$

where B is the generator-level probability density function of the Z line shape and $R_{1,2}$ are the detector response functions for the two leptons, which relate the reconstructed four-momenta to the true four-momenta. These response functions are calculated with MC simulations using a method described below. The reconstructed four-momenta, $\mathbf{p}_1^{\mathrm{reco}}$ and $\mathbf{p}_2^{\mathrm{reco}}$, are measured in the detector. Furthermore, the true masses of the leptons are known. This leaves a total of six unknown variables in the likelihood: the energy, η, and ϕ from each of the true four-momenta, $\mathbf{p}_1^{\mathrm{true}}$ and $\mathbf{p}_2^{\mathrm{true}}$. Since lepton angles are measured precisely in the ATLAS detector, the true η and ϕ are approximated well by their reconstructed values. After applying this approximation the only unknowns remaining in Equation 4.2 are the true lepton energies E_1^{true} and E_2^{true}. In this way, the likelihood function can be used to determine the most likely true energies. The resulting constrained four-vectors consisting of the best-fit energies, the lepton masses, and the reconstructed η and ϕ values, are used in the final reconstruction of the four lepton system.

The different functions in the likelihood are implemented as follows. The probability density function B is modeled by a relativistic Breit-Wigner function with the mean parameter set to the Z boson mass and the width parameter set to the natural width, Γ_Z. The response functions are each modeled by Gaussian distributions of the form $R_i = \text{Gaussian}(E_i^{\text{true}}|E_i^{\text{reco}}, \sigma_i)$, where the mean parameter is set to the reconstructed lepton energy and the width σ_i is set to the lepton energy resolution obtained from simulation. The validation of this method is described in Ref. [55]. Figure 4.4 shows a distribution of $m_{4\ell}$ before and after applying FSR recovery and the Z mass constraint. The best resolution is obtained when both corrections are applied.

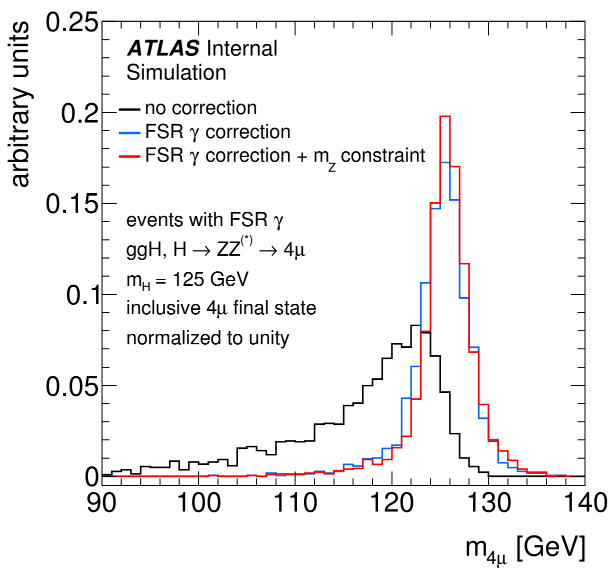

Figure 4.4: Distribution of $m_{4\ell}$ in the 4μ final state for events with identified FSR photons. The mass distribution is shown before any correction (black), after FSR recovery (blue), and after applying the Z mass constraint in addition to FSR recovery (red).

Event Yields

The full event selection is applied to the signal and background MC as well as the data. The resulting event yields are given in Table 4.5. The total expected signal and background yields scaled to the integrated luminosities for the 2011 and 2012 datasets are 18.02 and 14.61, respectively. Here, the signal is assumed to be a SM Higgs with a mass equal to 125.5 GeV. There are 45 events observed in data, which corresponds to a signal-to-background ratio of 2.1.

Final State	Signal	ZZ^*	Reducible Background	Total Expected	Observed
2012, $\sqrt{s} = 8$ TeV					
4μ	5.81	3.36	0.97	10.14	13
$2e2\mu$	3.72	2.33	0.84	6.89	9
$2\mu 2e$	3.00	1.59	0.52	5.11	8
$4e$	2.91	1.44	0.52	4.87	7
Combined	15.44	8.72	2.85	27.01	37
2011, $\sqrt{s} = 7$ TeV					
4μ	1.02	0.65	0.14	1.81	3
$2e2\mu$	0.64	0.45	0.13	1.22	2
$2\mu 2e$	0.47	0.29	0.53	1.29	1
$4e$	0.45	0.26	0.59	1.30	2
Combined	2.58	1.65	1.39	5.62	8

Table 4.5: The number of events expected and observed in each final state after the full event selection. The expected signal yields correspond to a 125.5 GeV Higgs with SM cross-section. The full dataset contains 45 passing events (expected 32.63) and a signal-to-background ratio of 2.1 (expected 1.2).

Matrix Element Reweighting Validation

A matrix element reweighting procedure is used to map a base signal MC sample to target CP coupling configurations, as described in Section 4.3.1. This procedure is validated using fully reconstructed MC events passing the event selection. The ($g_1 = 1, g_2 = g_4 = 1 + i$) signal MC sample listed in Table 4.2 is reweighted to the 0^+ coupling configuration and the resulting distributions are compared to the independent sample generated with the 0^+ assumption. Comparisons for the most relevant observables are shown in Figures 4.5 and 4.6. The first of the figures contains distributions of observables associated with Higgs production. Here the matrix element reweighting procedure has almost no impact because the observables are independent from the CP couplings at parton-level. The second figure contains observables associated with the Higgs decay, which have a greater dependence on the CP couplings. It can be seen in the figure that reweighting the ($g_1 = 1, g_2 = g_4 = 1+i$) MC sample effectively reproduces the 0^+ distributions. Differences between the matrix element reweighted distributions and the independent 0^+ distributions are found to be consistent with the statistical uncertainty in the samples.

4.5 Measurement Strategy

The measurement of non SM couplings is done using a nine-dimensional matrix element method, which is essentially a profile-likelihood method based on nine discriminant observables. The coupling values and uncertainties are obtained by maximizing a profile-likelihood ratio that is generically given by

$$\Lambda(\boldsymbol{\alpha}) = \frac{L\left(\boldsymbol{\alpha}, \hat{\hat{\boldsymbol{\theta}}}(\boldsymbol{\alpha})\right)}{L\left(\hat{\boldsymbol{\alpha}}, \hat{\boldsymbol{\theta}}\right)}, \tag{4.3}$$

where L represents a likelihood function, $\boldsymbol{\alpha}$ represents a vector of parameters of interest, and $\boldsymbol{\theta}$ represents a vector of nuisance parameters. The parameters of interest in $\boldsymbol{\alpha}$ are the CP coupling factors $\frac{\tilde{\kappa}_{AVV}}{\kappa_{SM}} \tan\alpha$ and $\frac{\tilde{\kappa}_{HVV}}{\kappa_{SM}}$. The nuisance parameters $\boldsymbol{\theta}$ correspond to either systematic uncertainties or unconstrained signal model parameters that are not relevant to the measurement of $\boldsymbol{\alpha}$. The $\hat{\boldsymbol{\alpha}}$ and $\hat{\boldsymbol{\theta}}$ terms in the denominator represent the global maximum likelihood estimates for $\boldsymbol{\alpha}$ and $\boldsymbol{\theta}$, respectively. The denominator is therefore a constant term that is included to scale the profile-likelihood so that the maximum (at $\boldsymbol{\alpha} = \hat{\boldsymbol{\alpha}}$) corresponds to a value of one. In the numerator, the nuisance parameters $\boldsymbol{\theta}$ are profiled. This means that at each value of $\boldsymbol{\alpha}$ the likelihood is maximized with respect to $\boldsymbol{\theta}$. The maximum likely

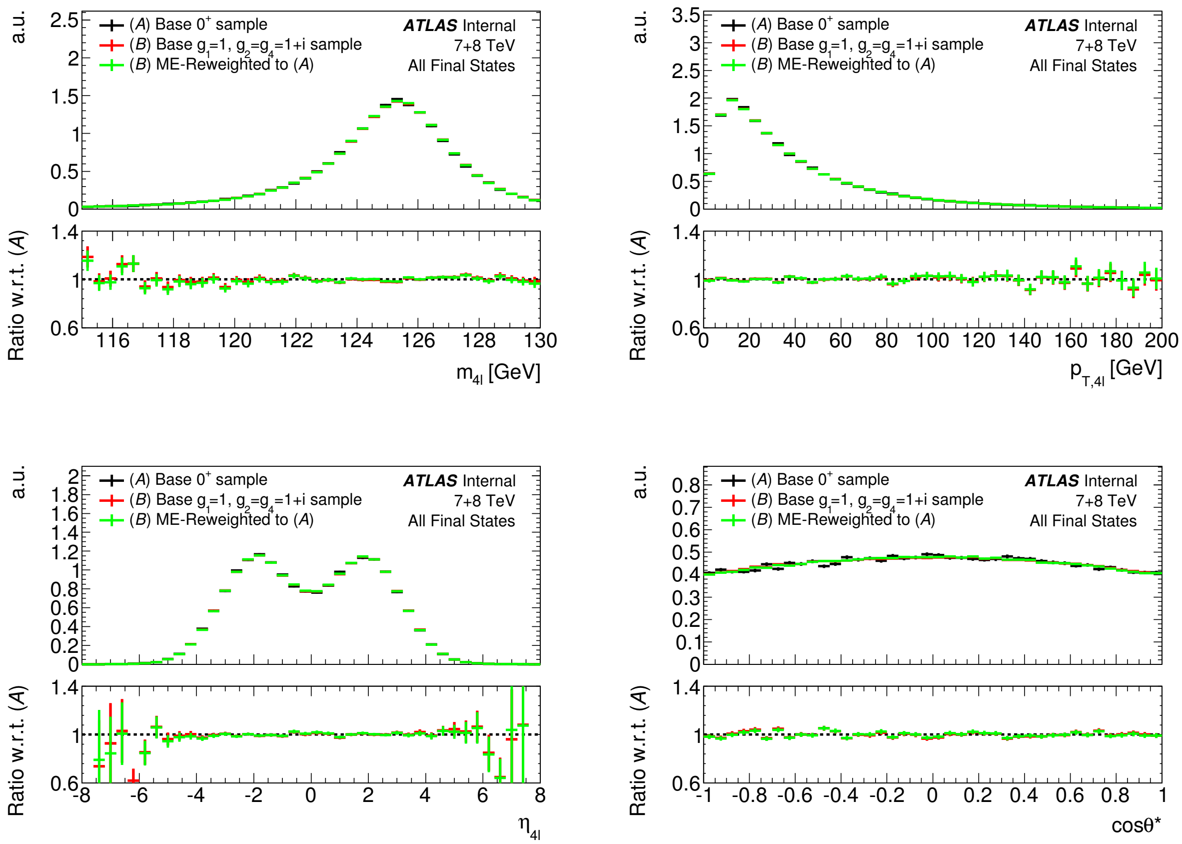

Figure 4.5: Validation plots for the matrix element reweighting procedure for observables that do not depend on the CP-even and CP-odd couplings. The base ($g_1 = 1, g_2 = g_4 = 1 + i$) sample is shown before (red) and after (green) matrix element reweighting to 0^+. The reweighted distribution is found to be consistent with an independent 0^+ sample (black), confirming that the reweighting procedure can be used to map the CP couplings to different values in the MC.

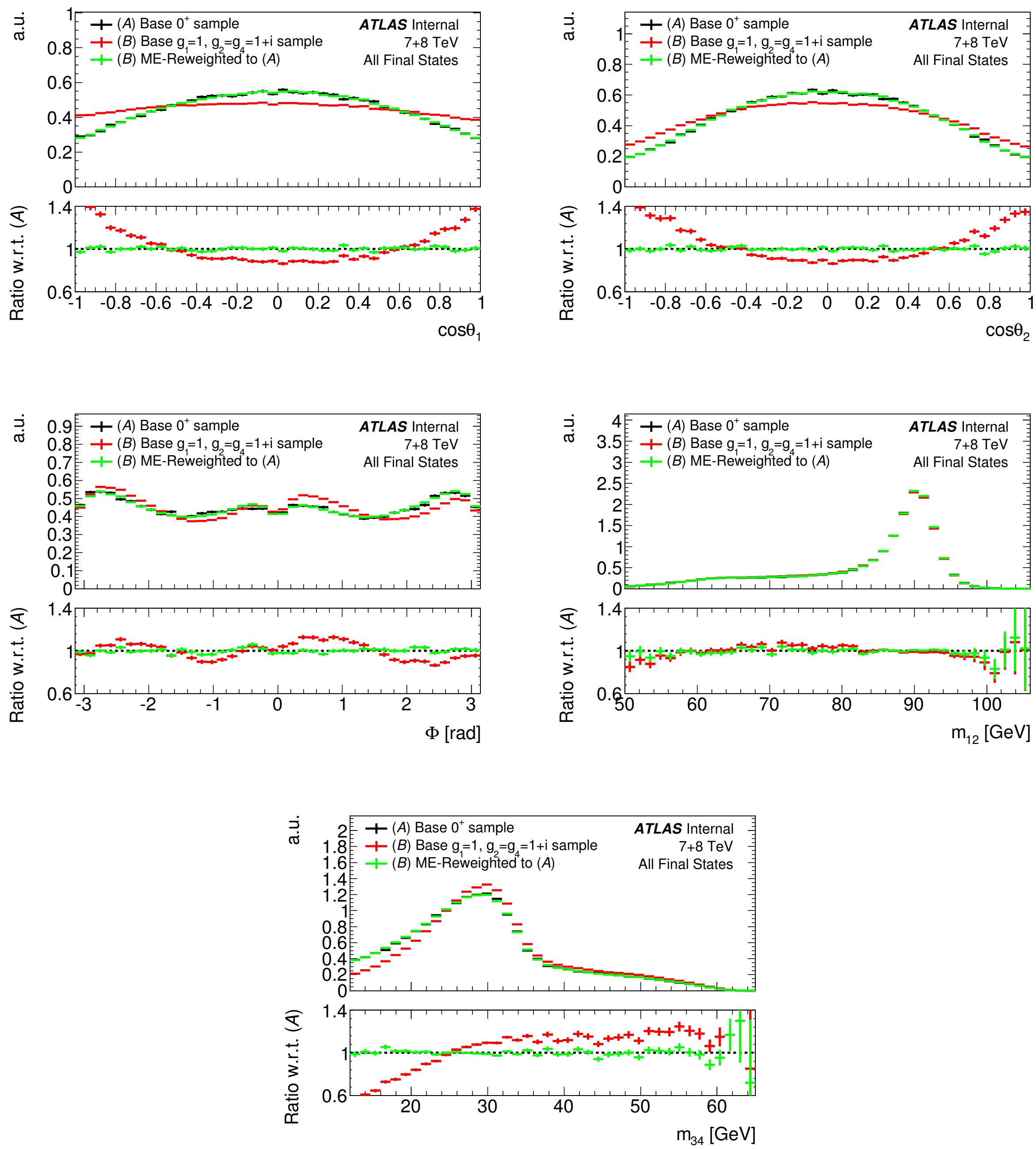

Figure 4.6: Validation plots for the matrix element reweighting procedure for observables that depend on the CP-even and CP-odd couplings. The base ($g_1 = 1, g_2 = g_4 = 1 + i$) sample is shown before (red) and after (green) matrix element reweighting to 0^+. The reweighted distribution is found to be consistent with an independent 0^+ sample (black), confirming that the reweighting procedure can be used to map the CP couplings to different values in the MC.

$\boldsymbol{\theta}$ corresponding to a particular value $\boldsymbol{\alpha}$ is represented in the equation by $\hat{\hat{\boldsymbol{\theta}}}(\boldsymbol{\alpha})$.

The likelihood function L is constructed from probability density functions (pdfs) that depend on nine discriminant observables. Fitting is done to unbinned data. Pdfs are generally constructed by binning simulated data and in some cases smoothing the resulting shape (more details on the method are included later in Section 4.6). There are separate terms included for each final state so that the likelihood can be used to simultaneously fit all of the data passing the event selection. The final states here are defined based on the lepton flavor combination and center of mass energy. The likelihood can be written as

$$L(\boldsymbol{\alpha}, \boldsymbol{\theta}) \propto \sum_i \text{Poisson}(n_i | N_{\text{tot},i}(\boldsymbol{\theta})) \prod_{j=1}^{n_i} f_i(\boldsymbol{x}_{ij} | \boldsymbol{\alpha}, \boldsymbol{\theta}), \tag{4.4}$$

where the sum i runs over the eight final states, n_i represents the number of observed events in final state i as shown in Table 4.5, f_i represents the pdf for final state i, and $\boldsymbol{x}_{ij}$ represents the nine measured observables in event j of final state i. The Poisson term in the sum is included to constrain the measurement based on the total number of events in each final state, and the mean parameter $N_{\text{tot},i}(\boldsymbol{\theta})$ represents the total expected SM yield in final state i (calculated using theoretical SM cross-sections for signal and background). Constraint terms corresponding to systematic uncertainties are neglected here for simplicity, but they are included in the measurement. Note that the pdfs f_i are very similar for different flavor final states. Slight differences arise because the detector resolution and acceptance are different for electrons and muons.

Each pdf f_i can be decomposed into three components corresponding to the signal, SM ZZ, and reducible background processes. For a particular final state i, the probability of observing an event with observable values $\boldsymbol{x}$ is given by

$$f_i(\boldsymbol{x} | \boldsymbol{\alpha}, \boldsymbol{\theta}) = \frac{N_{\text{sig},i}(\boldsymbol{\alpha}, \boldsymbol{\theta}) f_{\text{sig},i}(\boldsymbol{x} | \boldsymbol{\alpha}, \boldsymbol{\theta}) + N_{ZZ,i}(\boldsymbol{\theta}) f_{ZZ,i}(\boldsymbol{x} | \boldsymbol{\theta}) + N_{\text{red},i}(\boldsymbol{\theta}) f_{\text{red},i}(\boldsymbol{x} | \boldsymbol{\theta})}{N_{\text{sig},i}(\boldsymbol{\alpha}, \boldsymbol{\theta}) + N_{ZZ,i}(\boldsymbol{\theta}) + N_{\text{red},i}(\boldsymbol{\theta})}, \tag{4.5}$$

where $f_{\text{sig},i}$ is the pdf for signal, $f_{ZZ,i}$ is the pdf for the SM ZZ background, and $f_{\text{red},i}$ is the pdf for the reducible background. The terms $N_{\text{sig},i}$, $N_{ZZ,i}$, and $N_{\text{red},i}$ are the corresponding expected event yields for each process so that the sum of these expected yields is equal to $N_{\text{tot},i}$. The denominator in the equation is included to normalize $f_i(\boldsymbol{x} | \boldsymbol{\alpha}, \boldsymbol{\theta})$. Both the pdfs and expected yields depend on the nuisance parameters $\boldsymbol{\theta}$. However, the CP coupling factors $\boldsymbol{\alpha}$ only enter in the signal pdf. Interference between signal and the SM background is expected to have a negligible impact on the measurement and it is therefore neglected. The pdfs $f_{\text{sig},i}$, $f_{ZZ,i}$, and $f_{\text{red},i}$ are constructed using a mixture of simulated data and theoretical calculations. These procedures are described in detail in the following section.

The signal terms N_{sig} and f_{sig} can vary depending on the choice of model. To maintain generality, the signal strength μ and Higgs mass m_H are treated as unconstrained signal model nuisance parameters. The vector $\boldsymbol{\theta}$ can be rewritten as $(\mu, m_H, \boldsymbol{\theta}_{\text{syst}})$, where $\boldsymbol{\theta}_{\text{syst}}$ only contains nuisance parameters from systematic uncertainties. Since μ is unconstrained, the $N_{\text{sig},i}(\boldsymbol{\alpha}, \boldsymbol{\theta})$ term in the probability model is rewritten as $\mu N^{\text{SM}}_{\text{sig},i}(m_H, \boldsymbol{\theta}_{\text{syst}})$, where $N^{\text{SM}}_{\text{sig},i}$ is the expected signal yield under the SM assumption (thus neglecting the dependence on $\boldsymbol{\alpha}$).

Fitting is done by minimizing $-2\ln\Lambda(\boldsymbol{\alpha})$ instead of maximizing $\Lambda(\boldsymbol{\alpha})$ to simplify computation. The asymptotic approximation [58] is used to estimate the 68% and 95% confidence level (CL) intervals. According to this approximation, values of $\boldsymbol{\alpha}$ corresponding to $-2\ln\Lambda(\boldsymbol{\alpha}) > 1$ (3.84) are excluded at 68% (95%) CL. The validity of this approximation is discussed in Section 4.8.

4.6 Signal and Background Models

The pdfs for signal and background are constructed using nine discriminant observables,

$$\boldsymbol{x} = (m_{4\ell}, p_{T4\ell}, \eta_{4\ell}, \cos\theta^*, \cos\theta_1, \cos\theta_2, \Phi, m_{12}, m_{34}),$$

where $p_{T4\ell}$ and $\eta_{4\ell}$ are the reconstructed transverse momentum and pseudo-rapidity of the four lepton system, respectively, and the other observables are defined earlier in the chapter. Of these observables, only $\cos\theta_1$, $\cos\theta_2$, Φ, m_{12}, and m_{34} have distributions that depend on the CP coupling factors at parton-level. The others are included in the model because they help discriminate signal from background. Note that the azimuthal angles Φ_1 and Φ^* are neglected from the model because they offer no sensitivity to the CP parameters at parton-level and they are poor background discriminants.

The signal and background pdfs are designed to represent nine-dimensional distributions of fully reconstructed data. These distributions are generally derived by populating histograms with simulated events passing the selection. The histograms are smoothed using various methods (described in more detail later in this section). Then they are used to build the probability model in Equation 4.5 so that fits can be performed to unbinned data.

The simulated data samples available do not have sufficient statistics for populating full nine-dimensional histograms with complete correlation information. Thus, the observable-space is simplified by removing small correlations and thereby factoring the nine-dimensional shape into multiple histograms that each depend on a subset of the nine observables. In this way, the simulated data can be used to construct both signal and background shapes. For the signal pdf the matrix element is also used as input to help retain more correlation information, using a method described later in this section. Validation checks are done to ensure that neglecting small correlations does not bias measurements of the CP coupling parameters.

The correlations among the nine observables are measured using MC events that pass the selection to determine how the observable space can be factored. Figures 4.7 and 4.8 show the Pearson's correlations [59] between all pairs of observables for a particular BSM signal hypothesis and for the SM ZZ background. The Pearson's correlation is a measure of the linear correlation between observables: a value of 1 corresponds to a total positive correlation, 0 corresponds to no correlation, and -1 corresponds to a total negative correlation. One drawback of this correlation metric is that it is not sensitive to symmetric functional dependencies between observables. Such correlations should be visible in two-dimensional distributions of the observables, which are plotted for the 4μ 8 TeV final state in Figures 4.9 and 4.10. The distributions in other final states are found to be similar. The correlations most relevant for sensitivity to the tensor structure are those between $\cos\theta_1$ and $\cos\theta_2$, and between m_{12} and m_{34}. Note that the correlation between m_{12} and m_{34} is partially due to the event selection requirements that m_{12} be greater than m_{34} and that the sum of m_{12} and m_{34} be less than 130 GeV. A correlation between $p_{T4\ell}$ and $\eta_{4\ell}$ also exists, as expected. Each of these three dominant correlations are included in the signal and background components of the probability model. In the figures there are also small correlations between $m_{4\ell}$ and both m_{12} and m_{34}. These correlations are entirely due to the event selection requirements[2].

2. At parton-level the invariant mass of the Higgs and the invariant masses of the Z bosons are uncorrelated

They are therefore neglected in the detector-level probability model because they do not contribute to the sensitivity of the measurement.

In signal events there is also a small correlation between the helicity angles $(\cos\theta_1, \cos\theta_2)$ and Φ. This is particularly noticeable for the 0^- model and can be seen in Figure 4.11, which shows a comparison of Φ distributions in different slices of $\cos\theta_1$ and $\cos\theta_2$. The $\cos\theta_1$ and $\cos\theta_2$ slices used in the figure are chosen to make the correlation most visible. A similar comparison is shown for the ZZ background in Figure 4.12. Here it is not as significant.

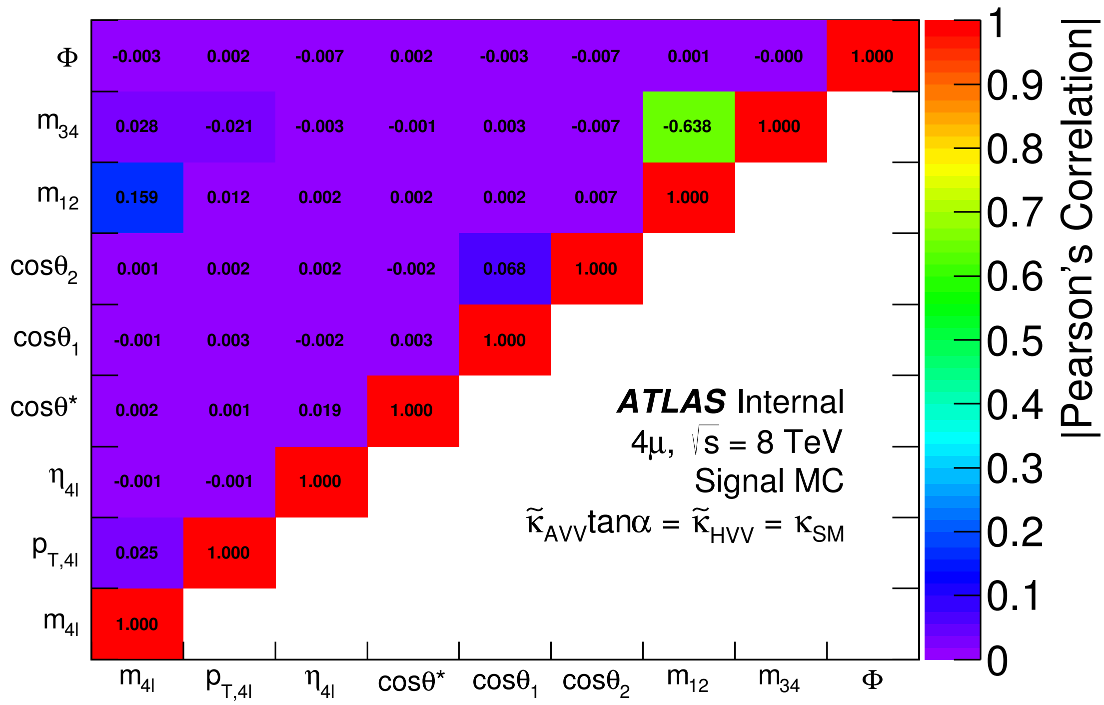

Figure 4.7: Pearson's correlation matrix for signal MC with $\frac{\tilde{\kappa}_{AVV}}{\kappa_{SM}}\tan\alpha = \frac{\tilde{\kappa}_{HVV}}{\kappa_{SM}} = 1$. This parameterization is chosen because it includes both CP-odd and CP-even BSM couplings. The matrices show the correlations between all sets of observables for $\sqrt{s} = 8$ TeV. Only events in the 4μ state are used, but the correlations are found to be similar between all final states.

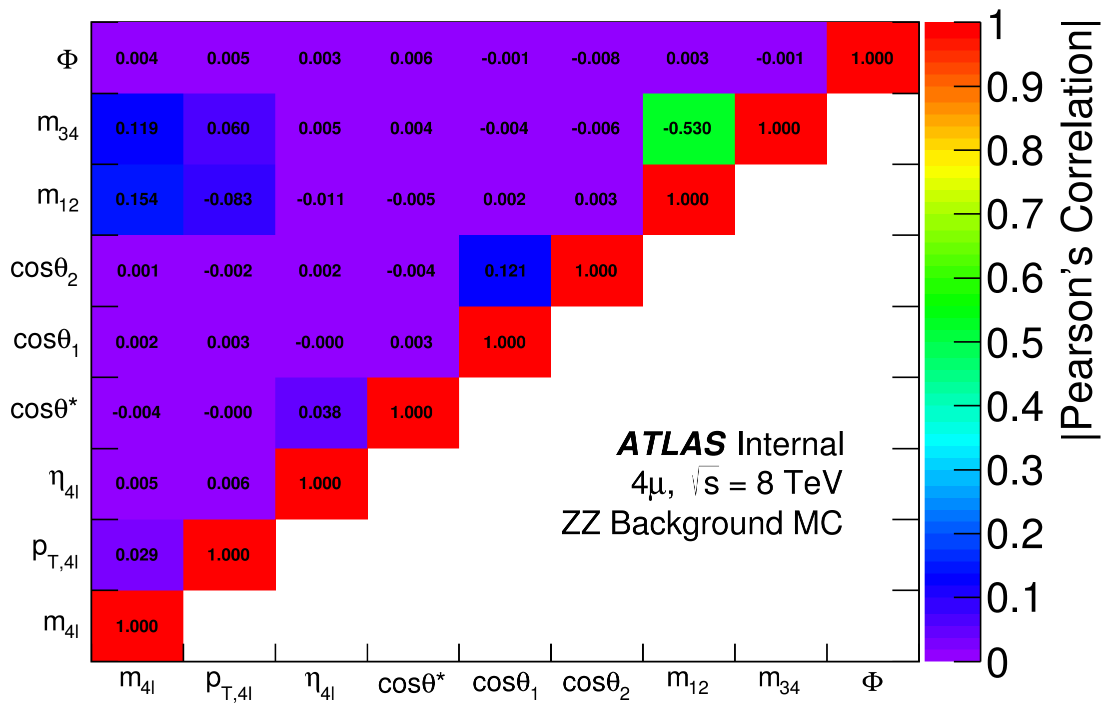

Figure 4.8: Pearson's correlation matrices for ZZ background MC. The matrices show the correlations between all sets of observables for $\sqrt{s} = 8$ TeV. Only events in the 4μ state are used, but the correlations are found to be similar in all final states.

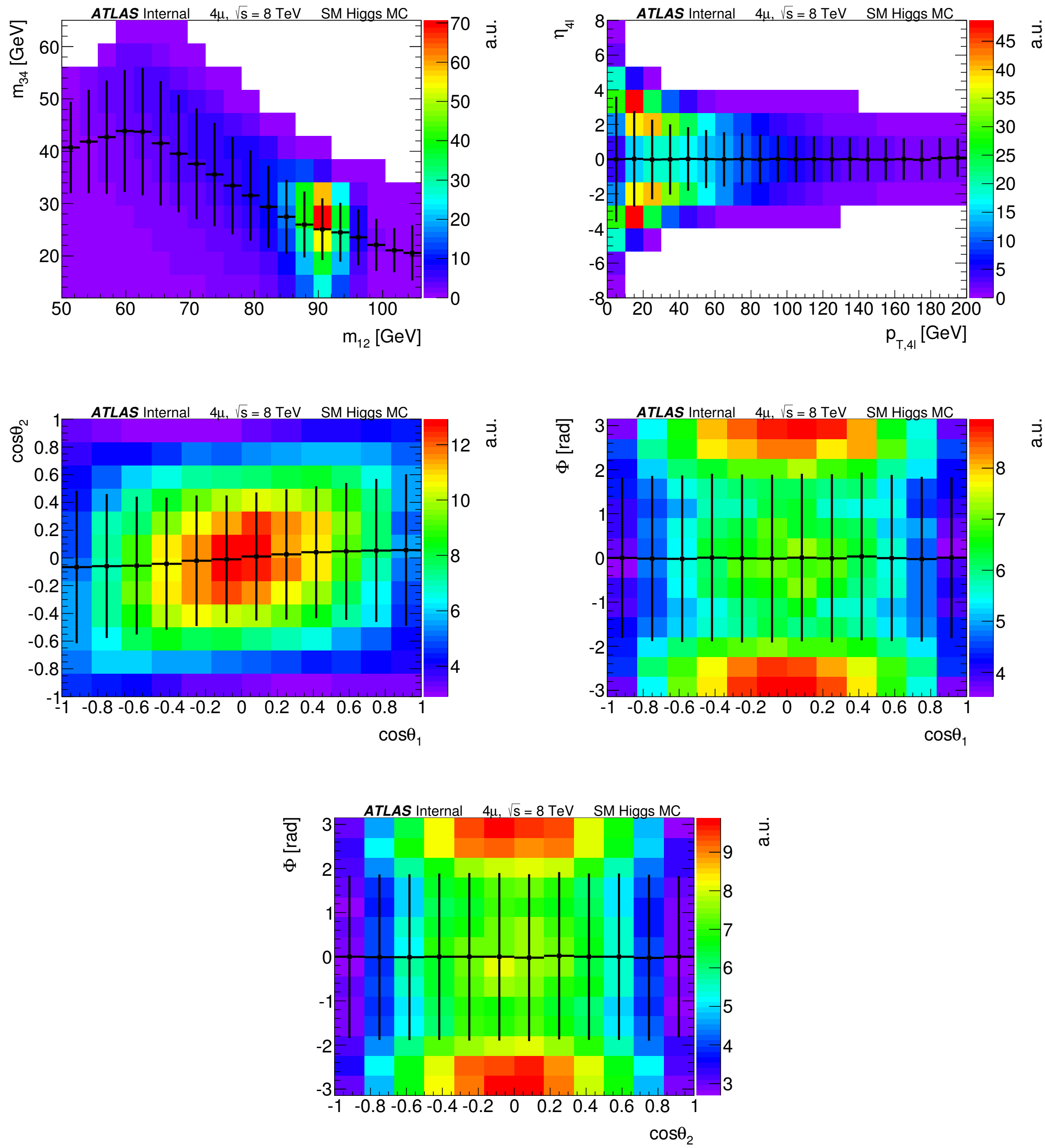

Figure 4.9: Two-dimensional distributions of the kinematic observables derived from SM signal MC in the 4μ final state for $\sqrt{s} = 8$ TeV. The black points with error bars show the mean and RMS for each bin in the horizontal axes. The distributions in other final states are found to be similar.

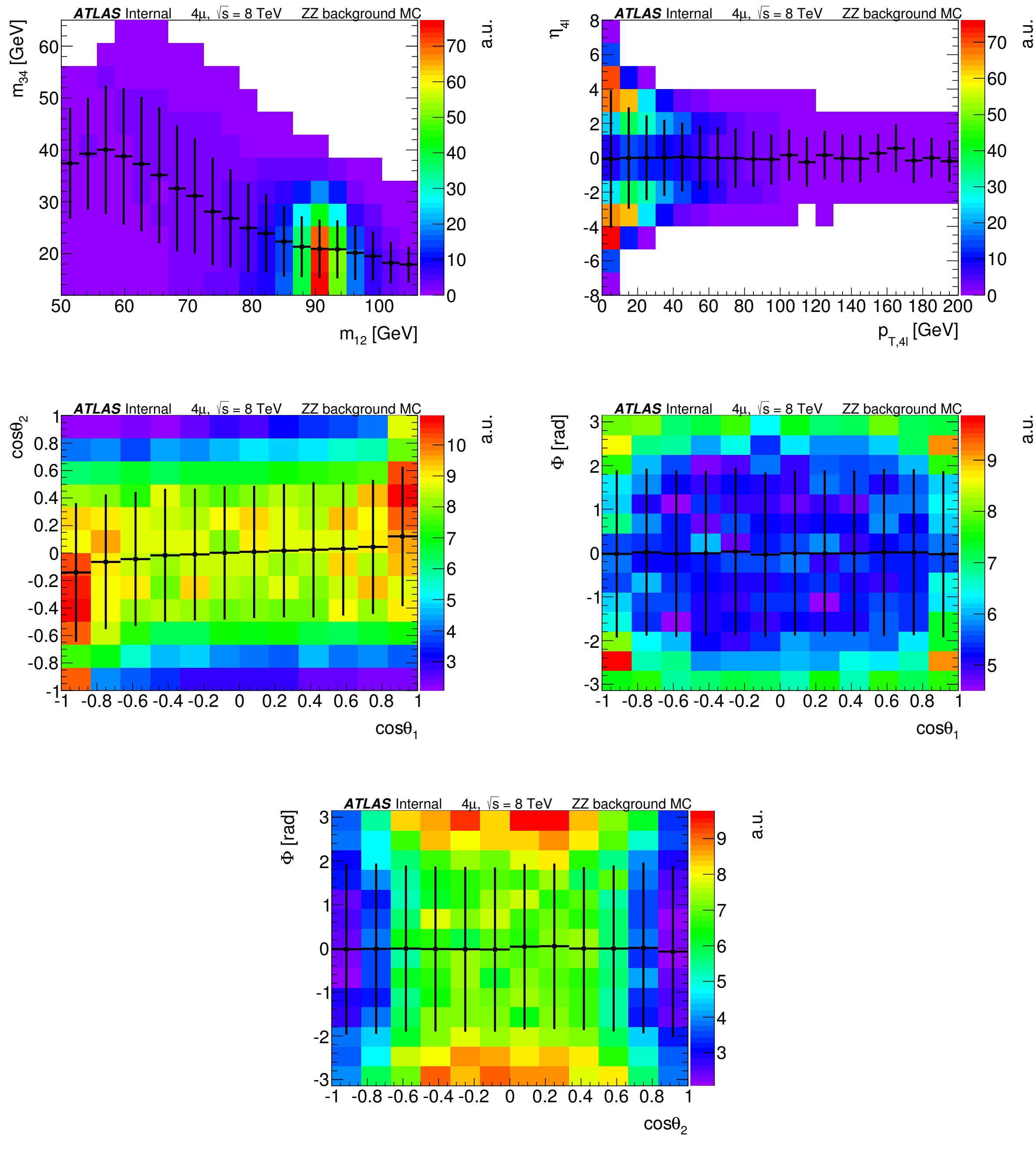

Figure 4.10: Two-dimensional distributions of the kinematic observables derived from ZZ background MC in the 4μ final state with $\sqrt{s} = 8$ TeV. The black points with error bars show the mean and RMS for each bin in the horizontal axes. The distributions in other final states are found to be similar.

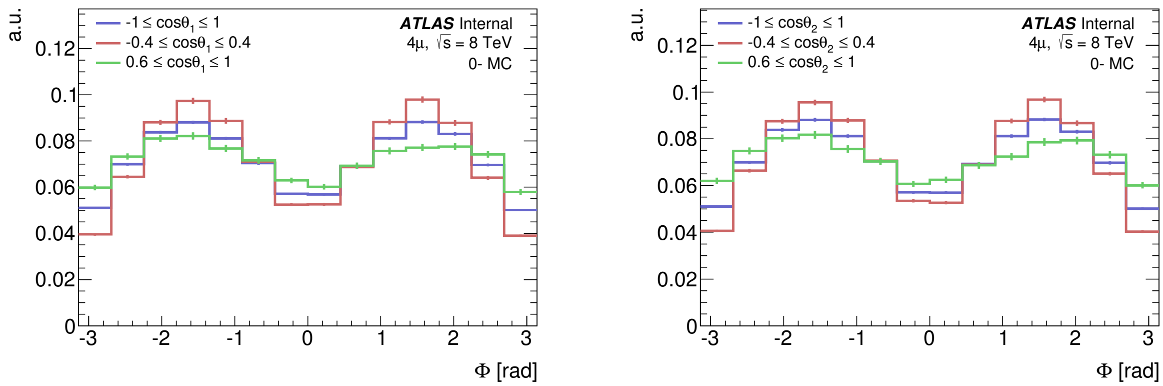

Figure 4.11: Distributions of Φ in different slices of $\cos\theta_1$ and $\cos\theta_2$ derived from 0^- signal MC in the 4μ final state with $\sqrt{s} = 8$ TeV. The $\cos\theta_1$ and $\cos\theta_2$ ranges are chosen to make the correlations between Φ and the two helicity angles visible. A similar correlation is present in all final states.

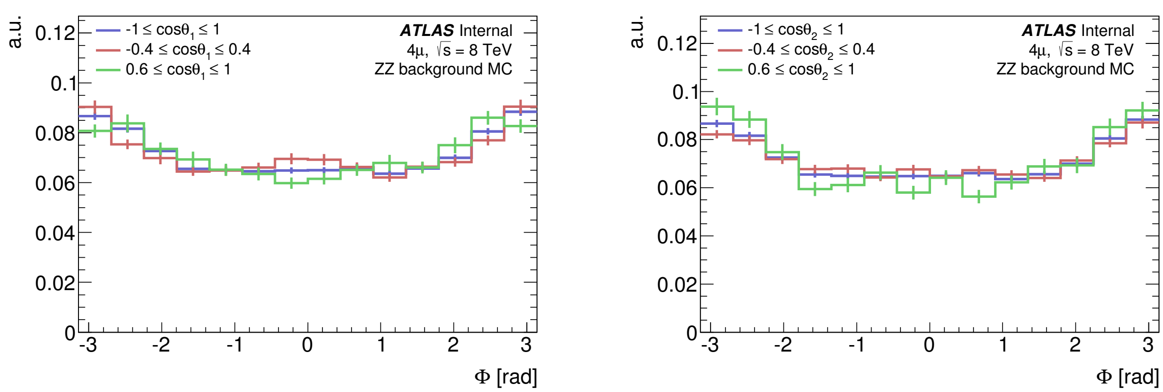

Figure 4.12: Distributions of Φ in different slices of $\cos\theta_1$ and $\cos\theta_2$ derived from ZZ background MC in the 4μ final state with $\sqrt{s} = 8$ TeV. A correlation between Φ and the two helicity angles is visible, but not as pronounced as it is in signal.

4.6.1 Signal Model

The signal pdf is derived using the fully reconstructed MC samples with ($g_1 = 1, g_2 = g_4 = 1+i$), listed in Table 4.2. The pdf is factored into four distributions, which altogether depend on the set of all nine observables. Histograms of $m_{4\ell}$, $\cos\theta^*$, and $p_{T4\ell}$ vs. $\eta_{4\ell}$ are produced by binning the MC events that pass the event selection. The one-dimensional histograms of $m_{4\ell}$ and $\cos\theta^*$ each consist of 20 bins of equal width. The observables $p_{T4\ell}$ and $\eta_{4\ell}$ consist of 20 and 12 bins of equal width, respectively.

The fourth distribution, which depends on observables $\cos\theta_1$, $\cos\theta_2$, Φ, m_{12}, and m_{34}, is the component of the signal pdf that provides sensitivity to the CP coupling parameters. There are not enough MC events to populate a five-dimensional histogram. Thus, the LO matrix element for signal [3] is used to produce an analytical parton-level distribution, which is used as a base description of the five-dimensional shape. This shape is then corrected for the event selection and for the acceptance, efficiency and resolution of the ATLAS detector using correction histograms that are derived from MC, as described below. To illustrate the approximate size of the detector corrections that are needed, the parton-level distributions from the matrix element are compared to fully reconstructed MC after the event selection for each of the five observables in Figures 4.13 and 4.14.

The purpose of the detector corrections is to alter the five-dimensional parton-level distribution so it is fully compatible with the reconstructed MC after the event selection. In general, a correction is applied by dividing a binned MC histogram by the uncorrected parton-level prediction. The corrections are derived for two or three observables at a time because there is not enough MC to produce a five-dimensional histogram. This is done for observable subsets that are mostly uncorrelated, namely (m_{12}, m_{34}) and $(\cos\theta_1, \cos\theta_2, \Phi)$. For example, a correction is first produced for (m_{12}, m_{34}) by filling a two-dimensional histogram of the measured values of m_{12} vs. m_{34} with reconstructed MC events passing the event selection. The uncorrected model based on the matrix element is also projected onto m_{12} vs. m_{34} and the MC histogram is divided by this uncorrected projection. The result is a two-dimensional correction histogram. When it is multiplied by the uncorrected five-dimensional model, the resulting shape has an m_{12} vs. m_{34} projection that is identical to reconstructed MC, by definition. Next, the procedure is repeated but with a three-dimensional histogram of the measured values of $\cos\theta_1$, $\cos\theta_2$, and Φ. When this additional correction is applied,

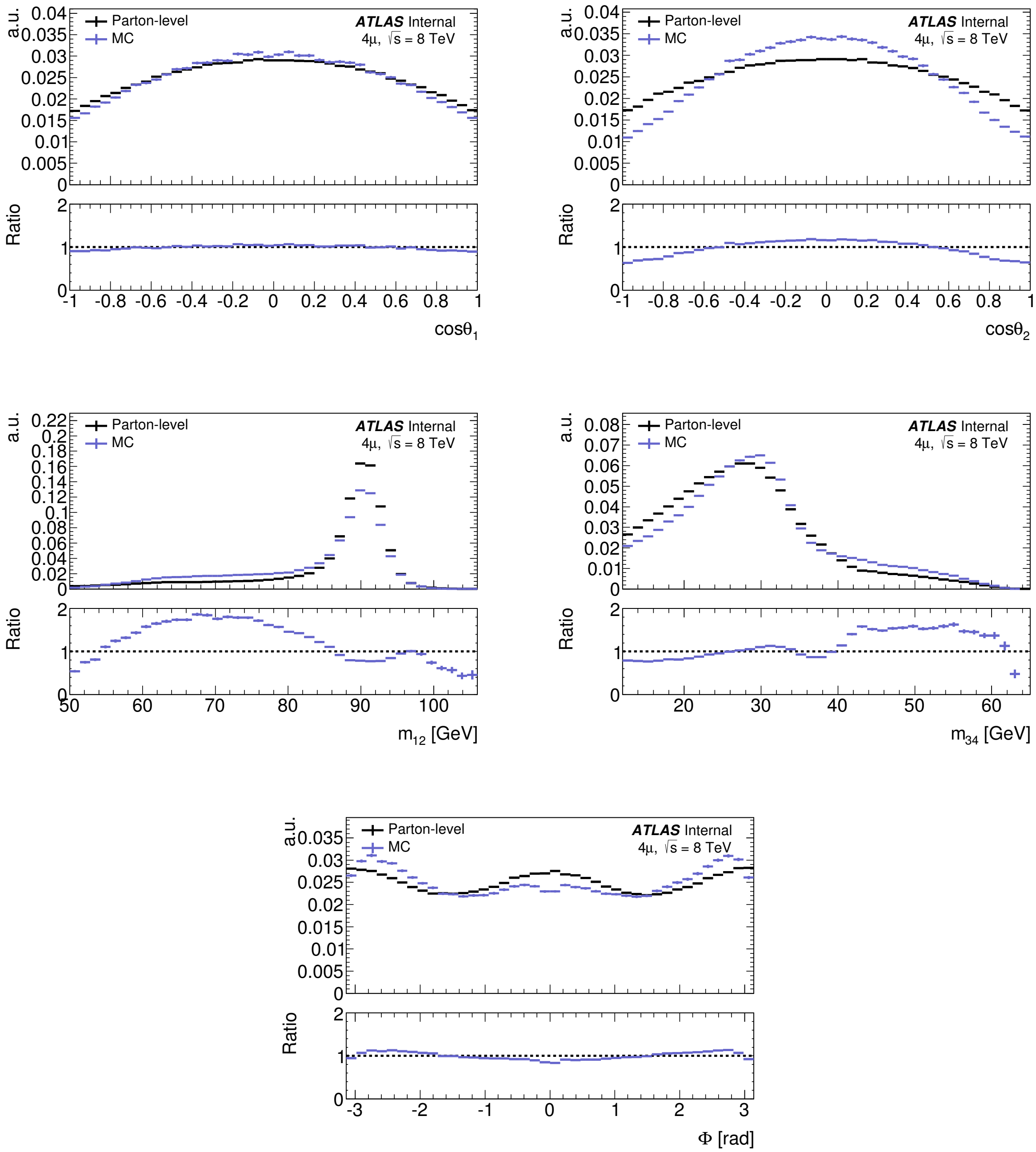

Figure 4.13: Distributions of the parton-level matrix element model compared to fully reconstructed MC in the 4μ final state with $\sqrt{s} = 8$ TeV.

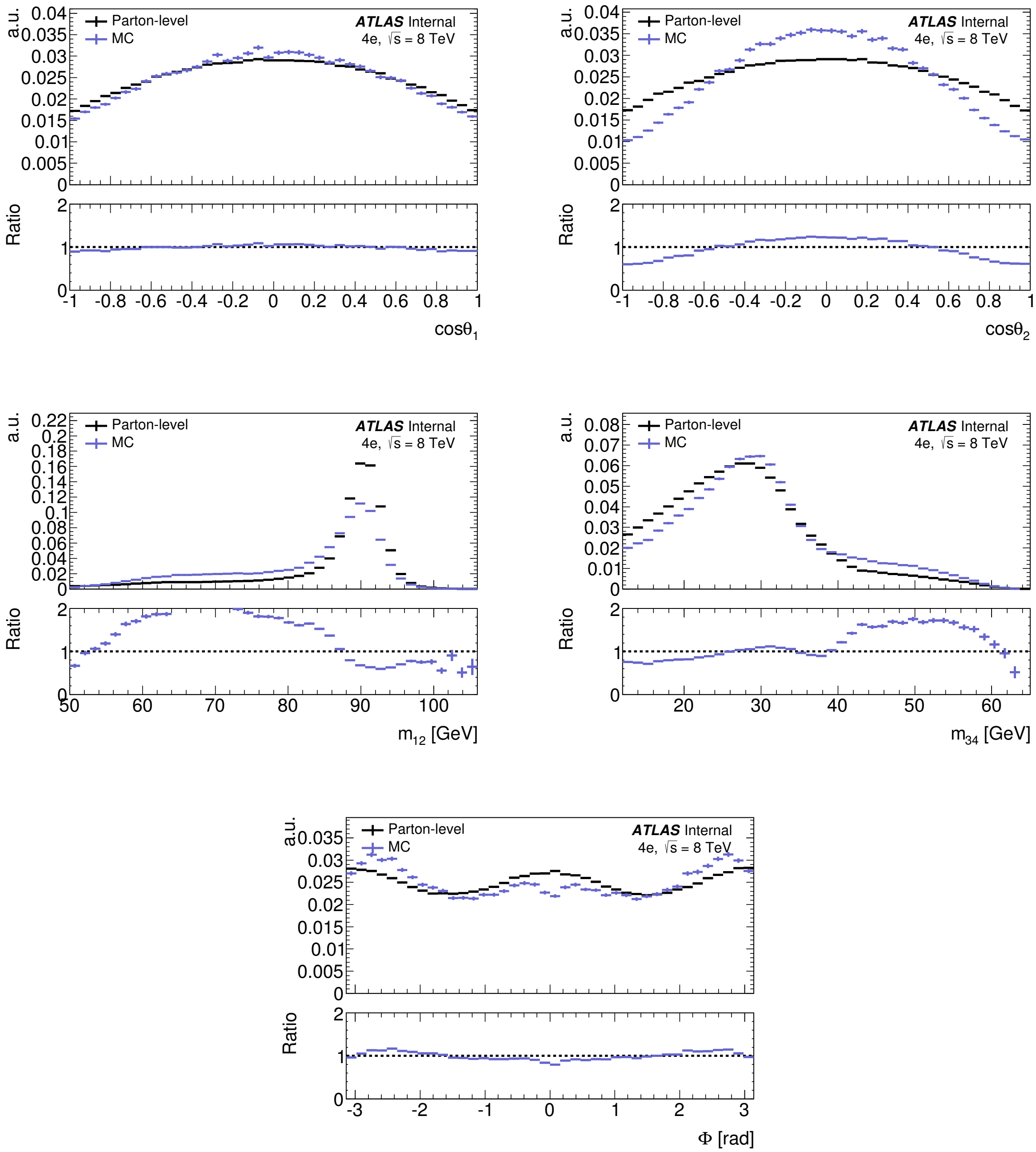

Figure 4.14: Distributions of the parton-level matrix element model compared to fully reconstructed MC in the $4e$ final state with $\sqrt{s} = 8$ TeV.

the m_{12} vs. m_{34} projection can change shape slightly due to small correlations between the (m_{12}, m_{34}) and $(\cos\theta_1, \cos\theta_2, \Phi)$ observable subsets. This is a small effect, but to ensure good agreement with the MC these two corrections are re-calculated and re-applied for three iterations. The correction histograms are produced using bins of equal width for each observable: $\cos\theta_1$, $\cos\theta_2$, and m_{34} are each divided into 12 bins, Φ is divided into 14 bins, and m_{12} is divided into 20 bins. The performance of this method is evaluated using quantitative comparisons of the reconstructed MC and the corrected parton-level prediction and the distributions are found to be consistent within the statistical uncertainty of the MC.

The detector corrections are found to depend slightly on the CP coupling factors due to kinematic differences associated with different signal hypotheses. For example, a correction derived from SM Higgs MC would not be valid for correcting the parton-level prediction for large $\frac{\tilde{\kappa}_{AVV}}{\kappa_{SM}} \tan\alpha$. Therefore the corrections are re-derived for each tested CP coupling configuration $\boldsymbol{\alpha}$ using the matrix element reweighted MC samples introduced in Section 4.3.1.

The full signal pdf is a product of the corrected five-dimensional distribution and the one- and two-dimensional MC histograms of $m_{4\ell}$, $\cos\theta^*$, and $p_{T4\ell}$ vs. $\eta_{4\ell}$. The one-dimensional histograms are smoothed by connecting the center of each consecutive bin with a straight line. Smoothing distributions with more than one dimension is generally more complicated. Several smoothing methods were tested and found to have no impact on expected results. Thus, no smoothing is applied for histograms with more than one dimension for simplicity.

Variations in the Higgs mass value, m_H, can change the shape of the signal pdf, primarily by shifting the distribution of $m_{4\ell}$. This dependence is included in the pdf so that m_H can be unconstrained in the fit. This is done by linearly interpolating the pdf shape between three mass points. A nominal pdf is produced assuming $m_H = 125.5$ GeV. Then two shifted pdfs are produced corresponding to shifts in m_H of ± 2 GeV. The full pdf is taken to be a linear combination of these three shapes. Some of the nuisance parameters corresponding to systematic uncertainties also impact the shape of the signal pdf, and these are incorporated in a similar way.

In principle there would be sufficient statistics for deriving a signal pdf entirely from MC if the five-dimensional component were factored into multiple histograms, each with fewer dimensions. This would simplify the model construction by removing the need to use the analytical parton-level pdf, but it would decrease sensitivity to CP parameters because the pdf would contain less correlation information. The impact on sensitivity is tested by fitting to SM signal MC before and after factoring the five-dimensional component it into multiple parts. Resulting distributions of $-2\ln\Lambda$ are shown in Fig. 4.15. No backgrounds or systematics are included in these fits. Removing the correlation between $(\cos\theta_1, \cos\theta_2, \Phi)$ and (m_{12}, m_{34}) causes the expected 95% CL interval on $\frac{\tilde{\kappa}_{AVV}}{\kappa_{SM}}\tan\alpha$ to grow by only 2%. This means that this particular correlation has a relatively small impact on the sensitivity of the analysis. Neglecting other correlations has a more significant impact.

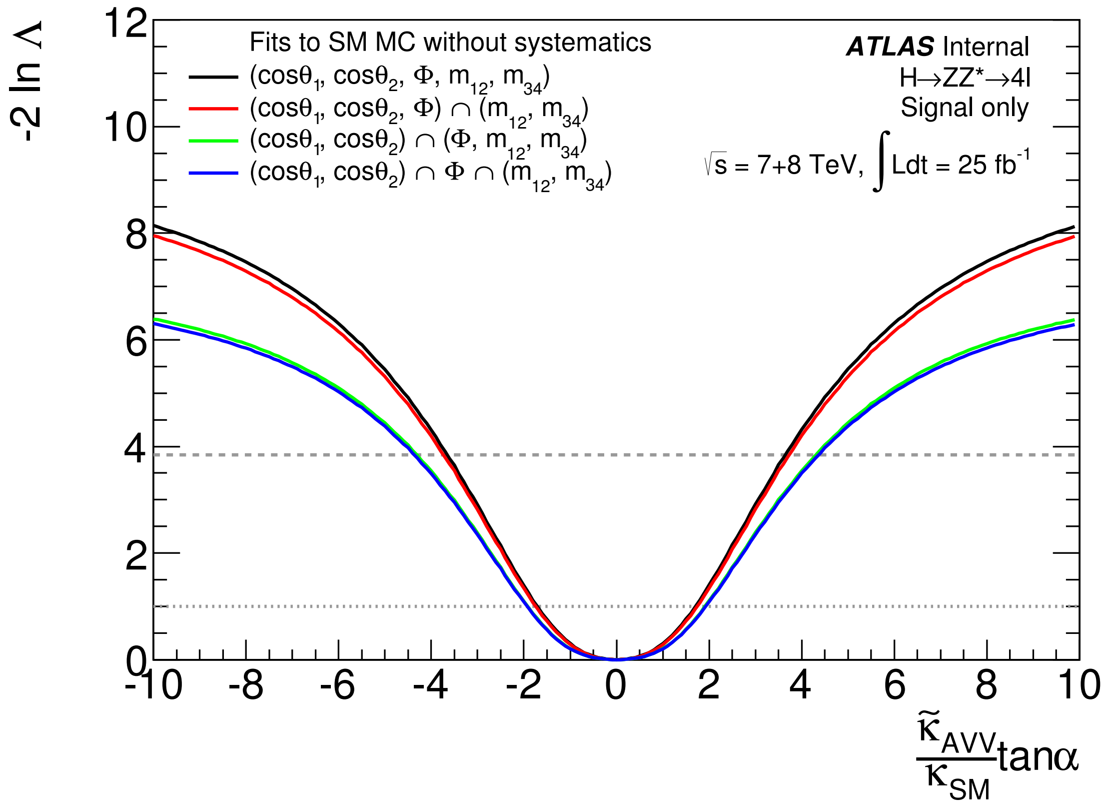

Figure 4.15: Comparison of $-2\ln\Lambda$ for different factorizations of the signal model. The fits are done to unbinned signal MC events that are scaled to the integrated luminosity from Run I, combining all final states. Only the 5 observables most sensitive the parameter $\frac{\tilde{\kappa}_{AVV}}{\kappa_{SM}}\tan\alpha$ are included, namely $\cos\theta_1$, $\cos\theta_2$, Φ, m_{12}, and m_{34}. The dropped correlations are represented by the $\cap$ symbol in the legend.

4.6.2 Background Model

The SM ZZ background pdf is treated similarly to the signal pdf, but factored into six distributions rather than four. No analytical parton-level prediction is used in this case, so each of the six components is a histogram derived directly from MC. Histograms of $m_{4\ell}$, $\cos\theta^*$, Φ, $(p_{T4\ell}, \eta_{4\ell})$, $(\cos\theta_1, \cos\theta_2)$, and (m_{12}, m_{34}) are produced by binning fully MC events passing the selection, using the same bin widths used for the signal model. The one-dimensional histograms are smoothed by linearly interpolating between bin centers. A kernel density estimation [60, 61] is used to produce a smooth distribution for $m_{4\ell}$, where each event in the $m_{4\ell}$ histogram is replaced with a Gaussian kernel that has a integral equal to the event weight. The kernel width parameter ρ that controls the width of each Gaussian is optimized by minimizing the χ^2 of the smooth distribution with respect to a distribution of independent ZZ MC events. The complete ZZ pdf is the product of the individual histograms after smoothing. The same procedure is used to construct the reducible background model.

4.6.3 Model Validation

To test the general validity of the probability model, a large sample of pseudo-data is generated from the model and then plotted in comparison with MC. Figures 4.16–4.23 show distributions for all eight analysis channels (four lepton flavor final states at 7 and 8 TeV). In each plot the pseudo-data and MC are binned and projected onto a single observable. The solid blue line represents the full model with signal and background, while the dashed and dotted blue lines represent the individual contributions from the two background components. The solid stacked distributions come from MC. Note that the MC distributions are populated using a sample of events that are independent from those used to derive the signal pdf, so statistical fluctuations are expected.

It is interesting to see how much sensitivity is lost if a small number of observables are integrated out of the likelihood fit. Figure 4.24 shows a comparison of $-2\ln\Lambda(\frac{\tilde{\kappa}_{AVV}}{\kappa_{SM}}\tan\alpha)$ distributions produced before and after removing the observables $p_{T4\ell}$, $\eta_{4\ell}$, $\cos\theta^*$, and $m_{4\ell}$ from the likelihood. The fits are done to unbinned signal and background MC events that correspond to the integrated luminosity from Run I. Systematic uncertainties are not included. Of the four observables tested, $m_{4\ell}$ has the greatest impact on the likelihood because it is

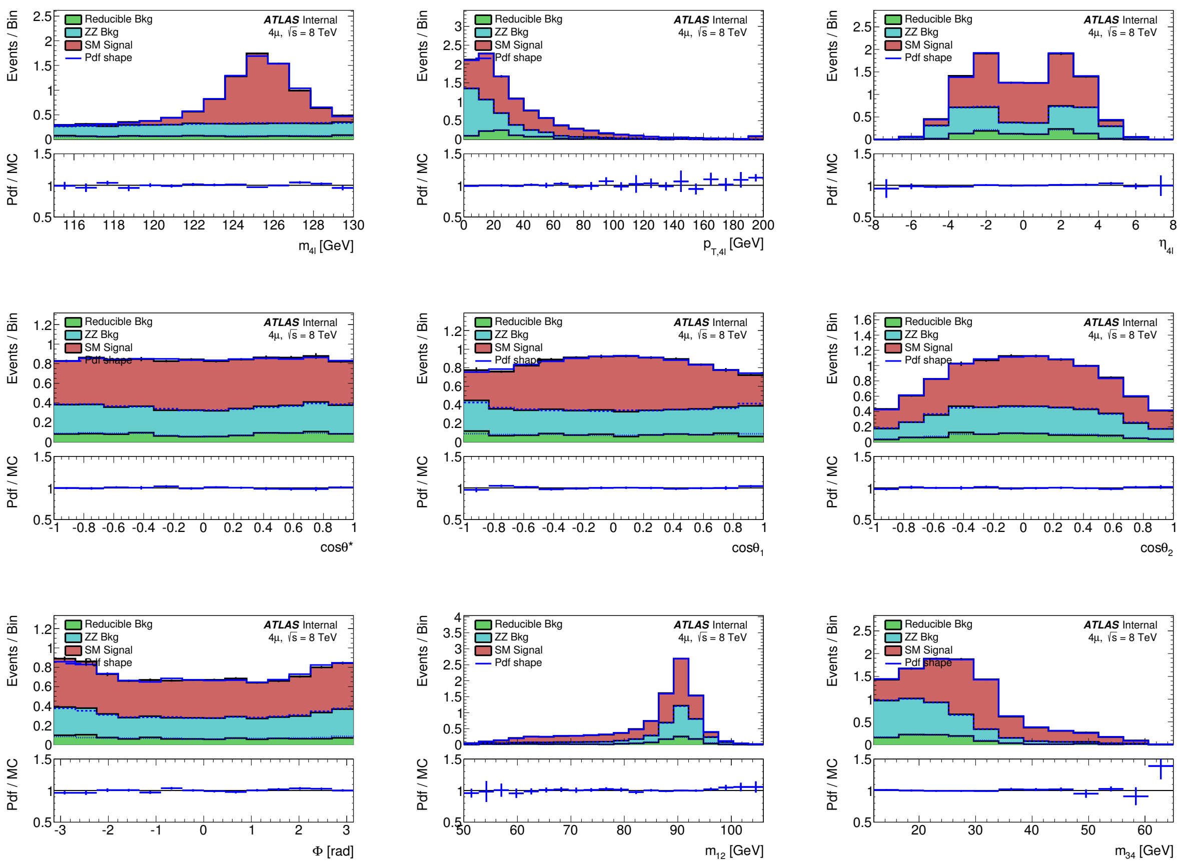

Figure 4.16: Comparison of the probability model to MC for SM Higgs signal in the 4μ final state with $\sqrt{s}$ = 8 TeV. The blue histograms are populated using a large set of pseudo-data generated from the model. The dashed and dotted blue histograms show the separate contributions from the SM ZZ and reducible backgrounds. The model is compared against independent MC events, so statistical fluctuations are expected.

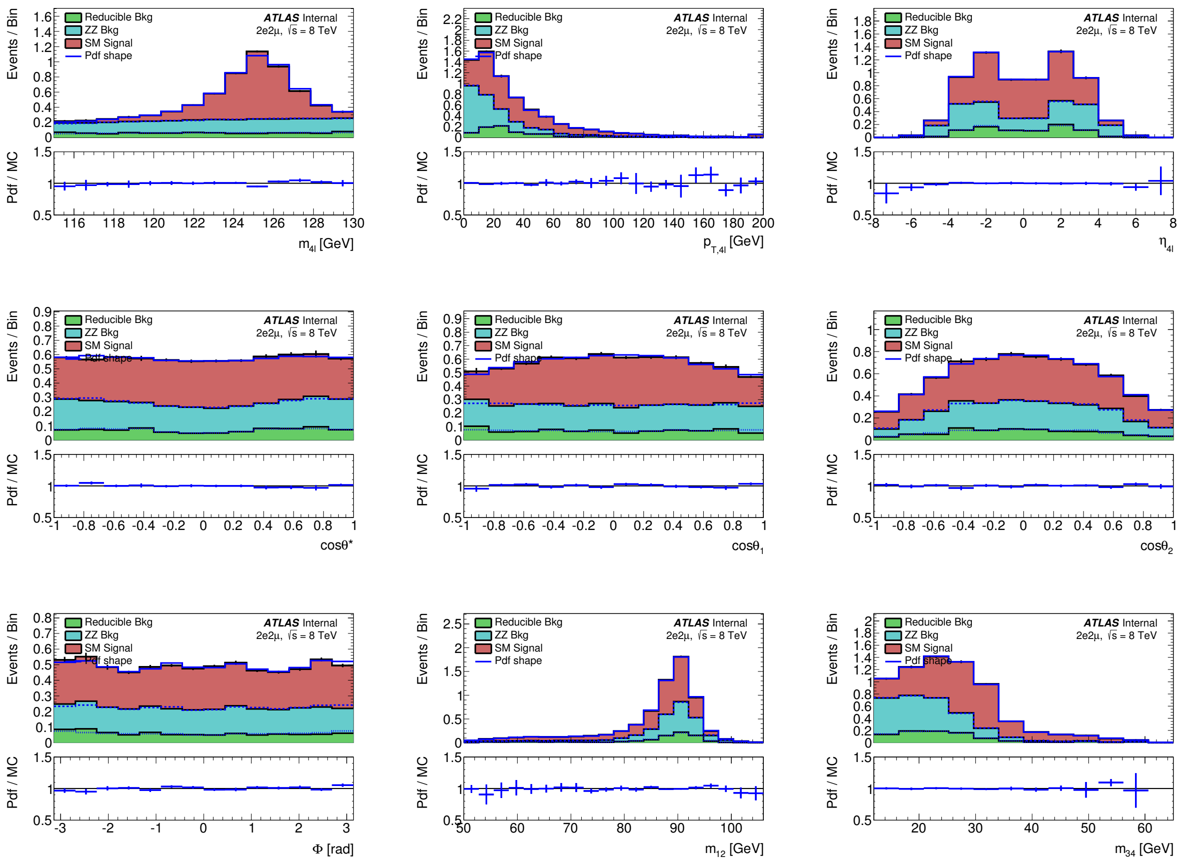

Figure 4.17: Comparison of the probability model to MC for SM Higgs signal in the $2e2\mu$ final state with $\sqrt{s} = 8$ TeV. The blue histograms are populated using a large set of pseudo-data generated from the model. The dashed and dotted blue histograms show the separate contributions from the SM ZZ and reducible backgrounds. The model is compared against independent MC events, so statistical fluctuations are expected.

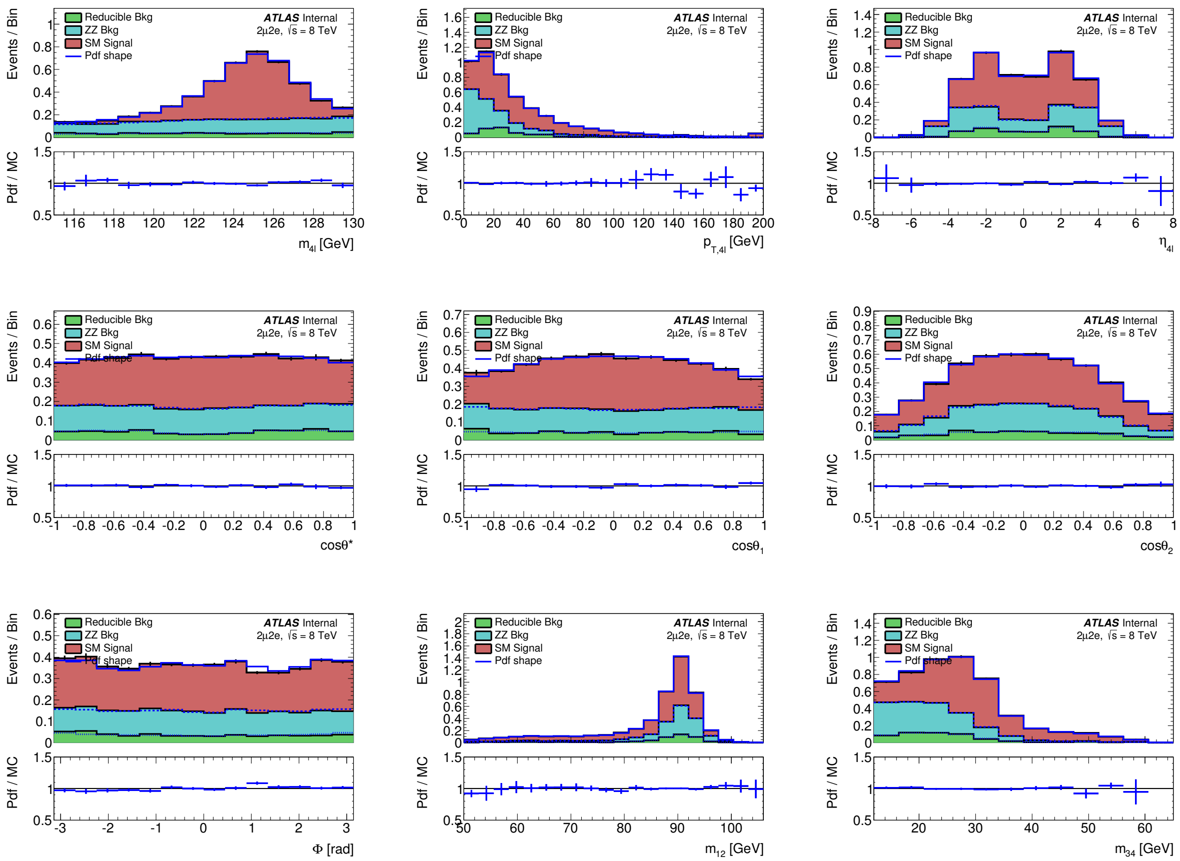

Figure 4.18: Comparison of the probability model to MC for SM Higgs signal in the $2\mu 2e$ final state with $\sqrt{s} = 8$ TeV. The blue histograms are populated using a large set of pseudo-data generated from the model. The dashed and dotted blue histograms show the separate contributions from the SM ZZ and reducible backgrounds. The model is compared against independent MC events, so statistical fluctuations are expected.

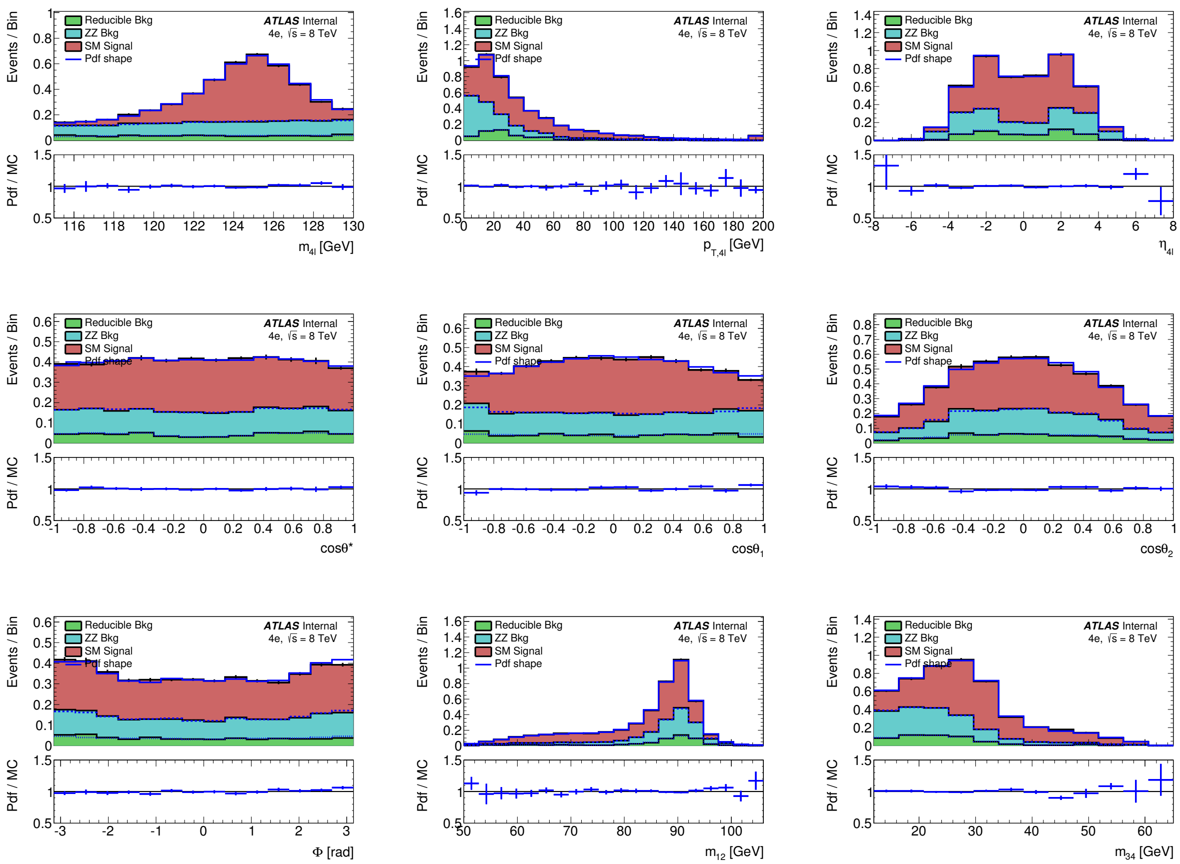

Figure 4.19: Comparison of the probability model to MC for SM Higgs signal in the $4e$ final state with $\sqrt{s} = 8$ TeV. The blue histograms are populated using a large set of pseudo-data generated from the model. The dashed and dotted blue histograms show the separate contributions from the SM ZZ and reducible backgrounds. The model is compared against independent MC events, so statistical fluctuations are expected.

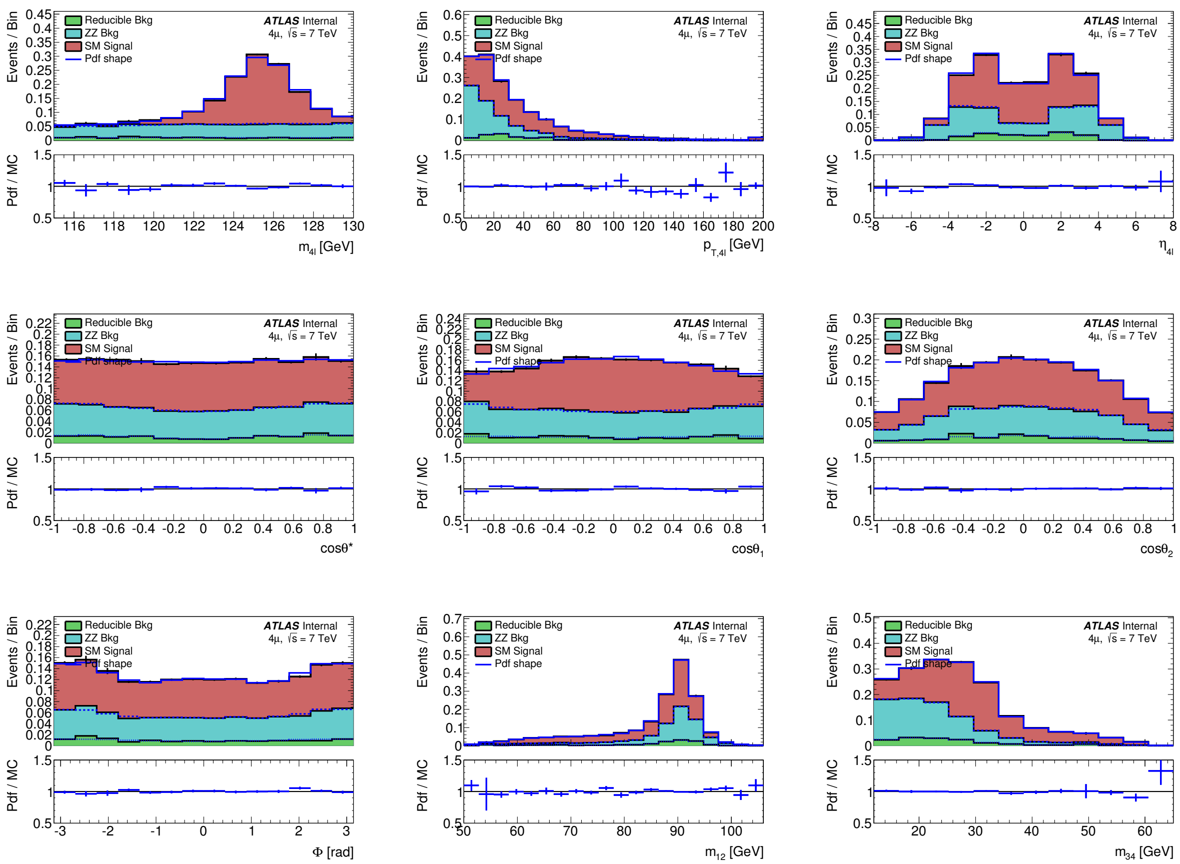

Figure 4.20: Comparison of the probability model to MC for SM Higgs signal in the 4μ final state with $\sqrt{s} = 7$ TeV. The blue histograms are populated using a large set of pseudo-data generated from the model. The dashed and dotted blue histograms show the separate contributions from the SM ZZ and reducible backgrounds. The model is compared against independent MC events, so statistical fluctuations are expected.

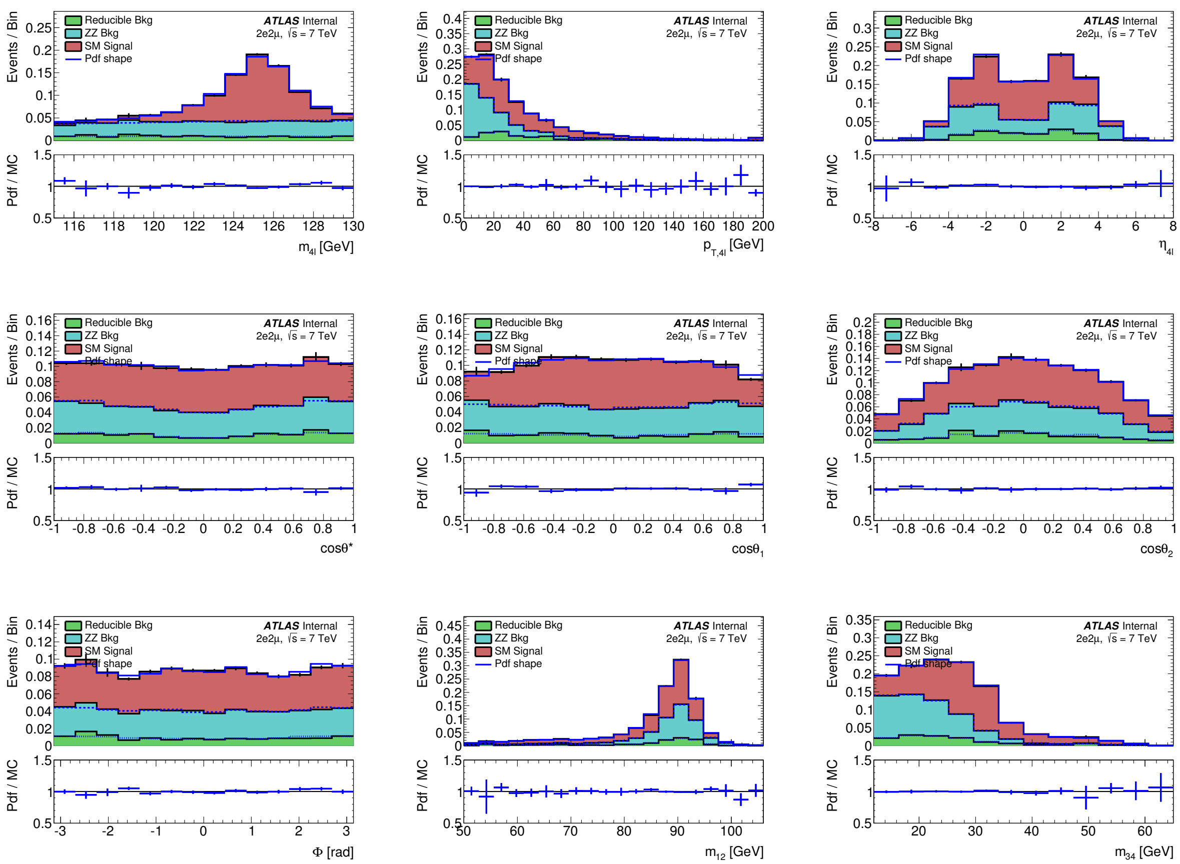

Figure 4.21: Comparison of the probability model to MC for SM Higgs signal in the $2e2\mu$ final state with $\sqrt{s} = 7$ TeV. The blue histograms are populated using a large set of pseudo-data generated from the model. The dashed and dotted blue histograms show the separate contributions from the SM ZZ and reducible backgrounds. The model is compared against independent MC events, so statistical fluctuations are expected.

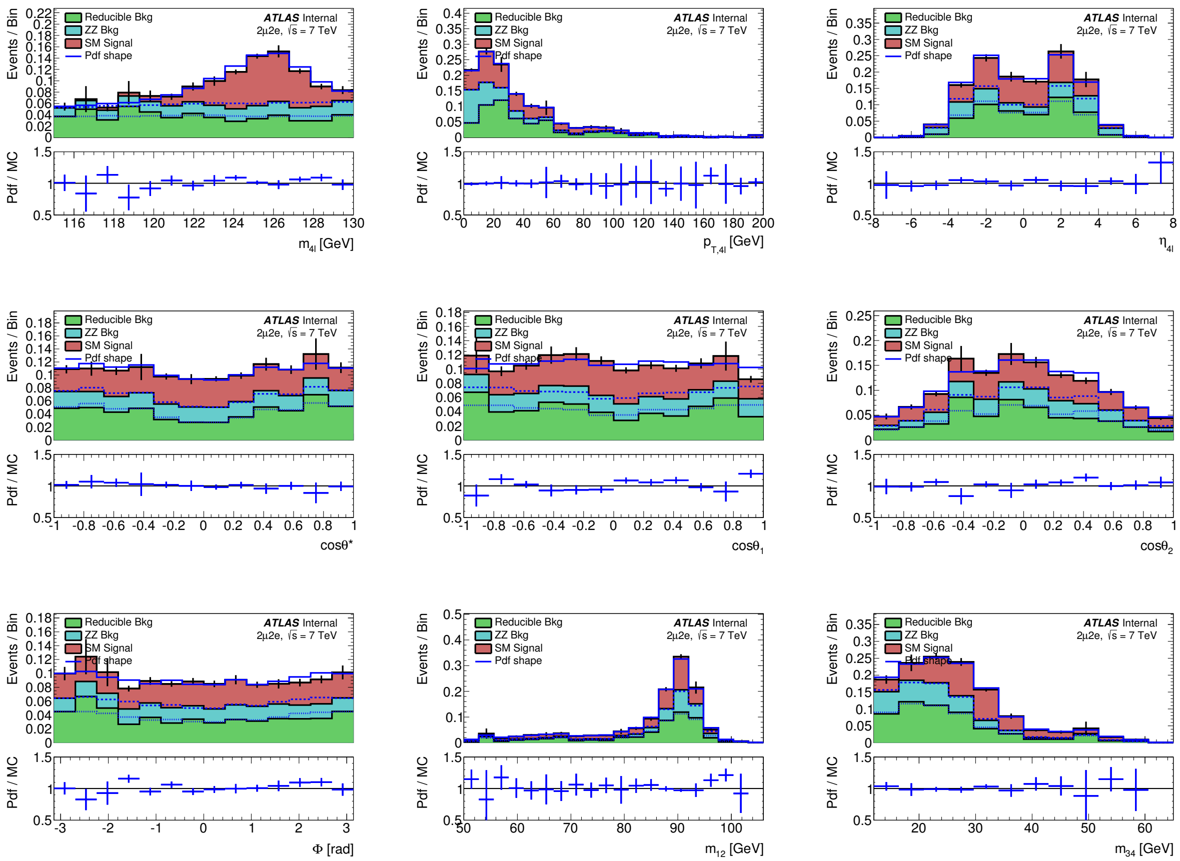

Figure 4.22: Comparison of the probability model to MC for SM Higgs signal in the $2\mu 2e$ final state with $\sqrt{s} = 7$ TeV. The blue histograms are populated using a large set of pseudo-data generated from the model. The dashed and dotted blue histograms show the separate contributions from the SM ZZ and reducible backgrounds. The model is compared against independent MC events, so statistical fluctuations are expected.

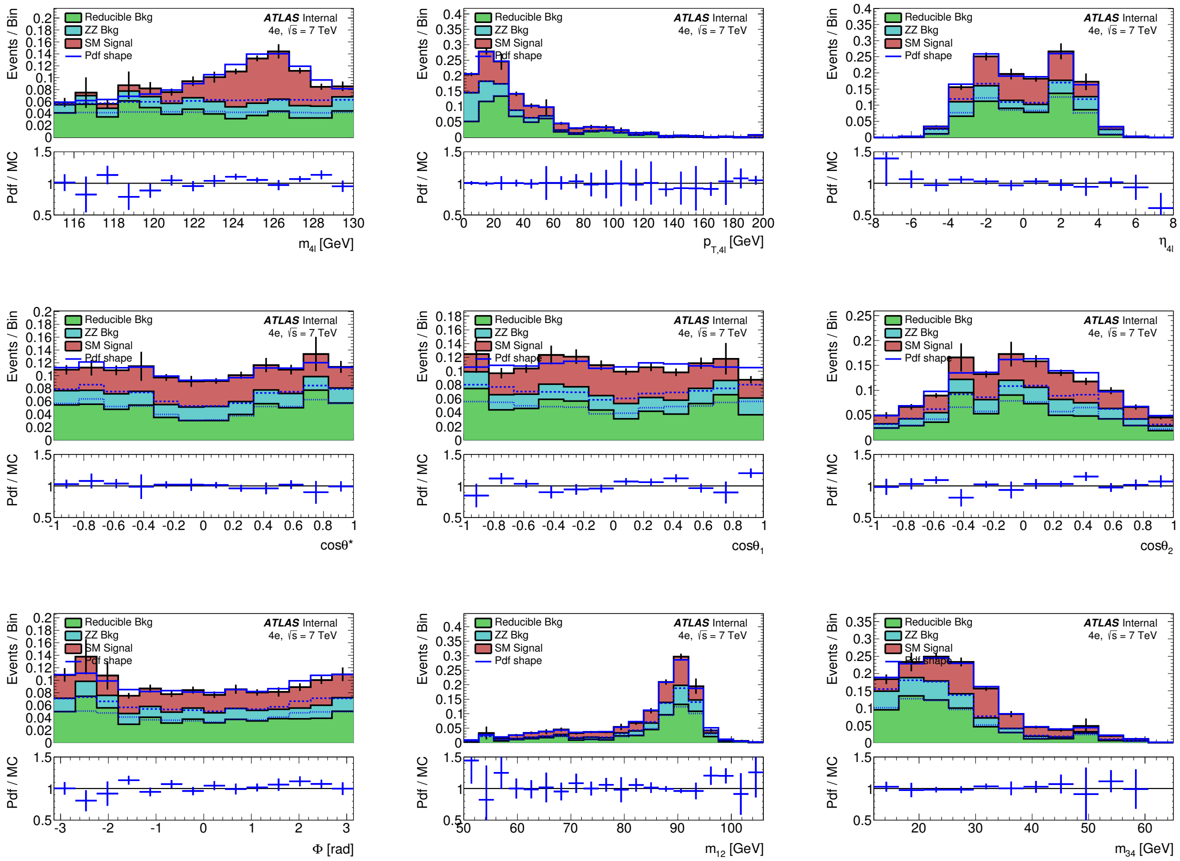

Figure 4.23: Comparison of the probability model to MC for SM Higgs signal in the $4e$ final state with $\sqrt{s} = 7$ TeV. The blue histograms are populated using a large set of pseudo-data generated from the model. The dashed and dotted blue histograms show the separate contributions from the SM ZZ and reducible backgrounds. The model is compared against independent MC events, so statistical fluctuations are expected.

best at discriminating signal from background. The size of the 95% CL interval grows by 48% when neglecting $m_{4\ell}$, 3% when neglecting $p_{T4\ell}$ and $\eta_{4\ell}$, and 1% when neglecting $\cos\theta^*$.

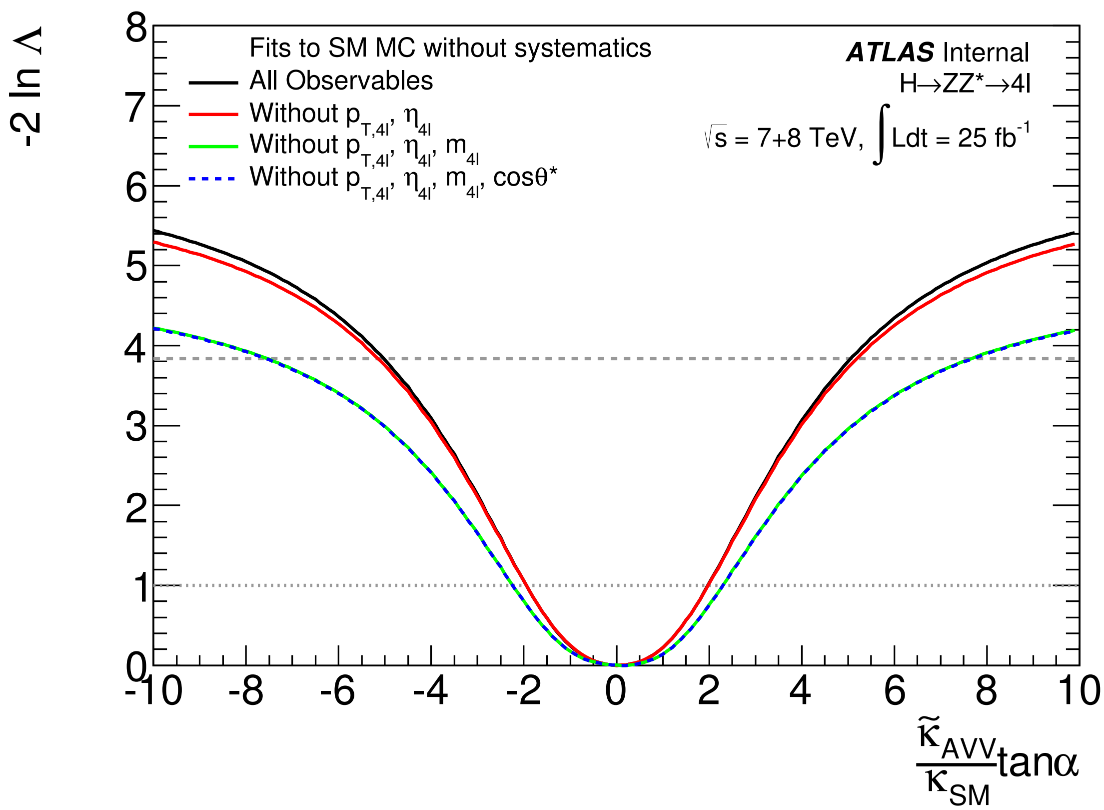

Figure 4.24: Comparison of likelihood curves for the nominal model, and the model reproduced with fewer observables. The fits are done to unbinned signal and background MC events that are scaled to the integrated luminosity from Run I with all final states combined. The observable $m_{4\ell}$ is found to be much more powerful than $p_{T4\ell}$, $\eta_{4\ell}$, and $\cos\theta^*$. The size of the 2σ interval grows by 3% when neglecting $p_{T4\ell}$ and $\eta_{4\ell}$, 51% when neglecting $p_{T4\ell}, \eta_{4\ell}$ and $m_{4\ell}$, and 52% when neglecting $p_{T4\ell}, \eta_{4\ell}, m_{4\ell}$ and $\cos\theta^*$.

A series of validation tests have been performed to verify that likelihood method works as expected and that the signal and background pdfs have negligible bias. As a first test, a large sample of three million pseudo-events is generated from the combined probability model with the parameters $\frac{\tilde{\kappa}_{HVV}}{\kappa_{SM}}$ and $\frac{\tilde{\kappa}_{AVV}}{\kappa_{SM}}\tan\alpha$ fixed to test values. A fit is done to the pseudo-data to verify that the maximum likelihood estimates for the CP coupling parameters equal the test values. This check is done for $\frac{\tilde{\kappa}_{HVV}}{\kappa_{SM}} = 0, \pm 2, \pm 4, \pm 6, \pm 8$ with $\frac{\tilde{\kappa}_{AVV}}{\kappa_{SM}}\tan\alpha = 0$, and for $\frac{\tilde{\kappa}_{AVV}}{\kappa_{SM}}\tan\alpha = 0, \pm 2, \pm 4, \pm 6, \pm 8$ with $\frac{\tilde{\kappa}_{HVV}}{\kappa_{SM}} = 0$. Fits are performed using the full likelihood function, as well as the likelihood functions corresponding to each of the eight final states. Systematic uncertainties are neglected. In all cases, the maximum likelihood estimates are found to be equal to the test values.

While these fits help test the likelihood fit method, they do not test the signal and background pdfs for bias. The latter is done by repeating the same procedure but fitting to MC events that are independent from those used to derive the model. For this test, the signal and background MC samples are each split into two subsets after the full reconstruction and event selection. Half of the events are used to construct signal and background pdfs. Then fits are performed to the remaining half of independent events. Each of the fitted events is given a small weight such that the sum of the event weights is equal to the total number of expected events in the Run I data. In this way, the sensitivity in each fit corresponds to the expected sensitivity in the data. Some example fit results are shown in Figure 4.25 for $\frac{\tilde{\kappa}_{AVV}}{\kappa_{SM}} \tan\alpha$ and Figure 4.26 for $\frac{\tilde{\kappa}_{HVV}}{\kappa_{SM}}$. In these examples the fits are done to SM MC, separately for each lepton flavor final state. The arrows on the figures indicate the MC parameterization, with $\frac{\tilde{\kappa}_{AVV}}{\kappa_{SM}} \tan\alpha = \frac{\tilde{\kappa}_{HVV}}{\kappa_{SM}} = 0$. Small fluctuations in the measured value on the order of 0.1 are expected due to the statistical uncertainty in the fitted MC. All of the observed fluctuations are well below the 1σ level in terms of the expected statistics from Run I. These tests are repeated with the backgrounds neglected to further probe the level of bias in the signal pdf and the results are shown in Figures 4.27 and 4.28. Checks are also done for different CP parameterizations and for the combination of all final states. In all cases, no significant bias is found.

Note that the likelihood curves for measurements of $\frac{\tilde{\kappa}_{HVV}}{\kappa_{SM}}$ (shown in Figures 4.26 and 4.28) are asymmetric about zero. This is expected due to the structure of the signal matrix element, which is also asymmetric about zero. Furthermore, for values near $\frac{\tilde{\kappa}_{HVV}}{\kappa_{SM}} = -1.5$, cancellations in the matrix element cause large variations in the distribution of $(\cos\theta_1, \cos\theta_2, \Phi, m_{12}, m_{34})$. As a result, there is a strong expected exclusion of values near -1.5 under the SM assumption. This is shown further in the following chapter.

4.7 Systematic Uncertainty

The sensitivity of the CP coupling measurement is limited primarily by statistical uncertainty due to the small cross section and branching ratio for the $H \to ZZ^* \to 4\ell$ decay, along with

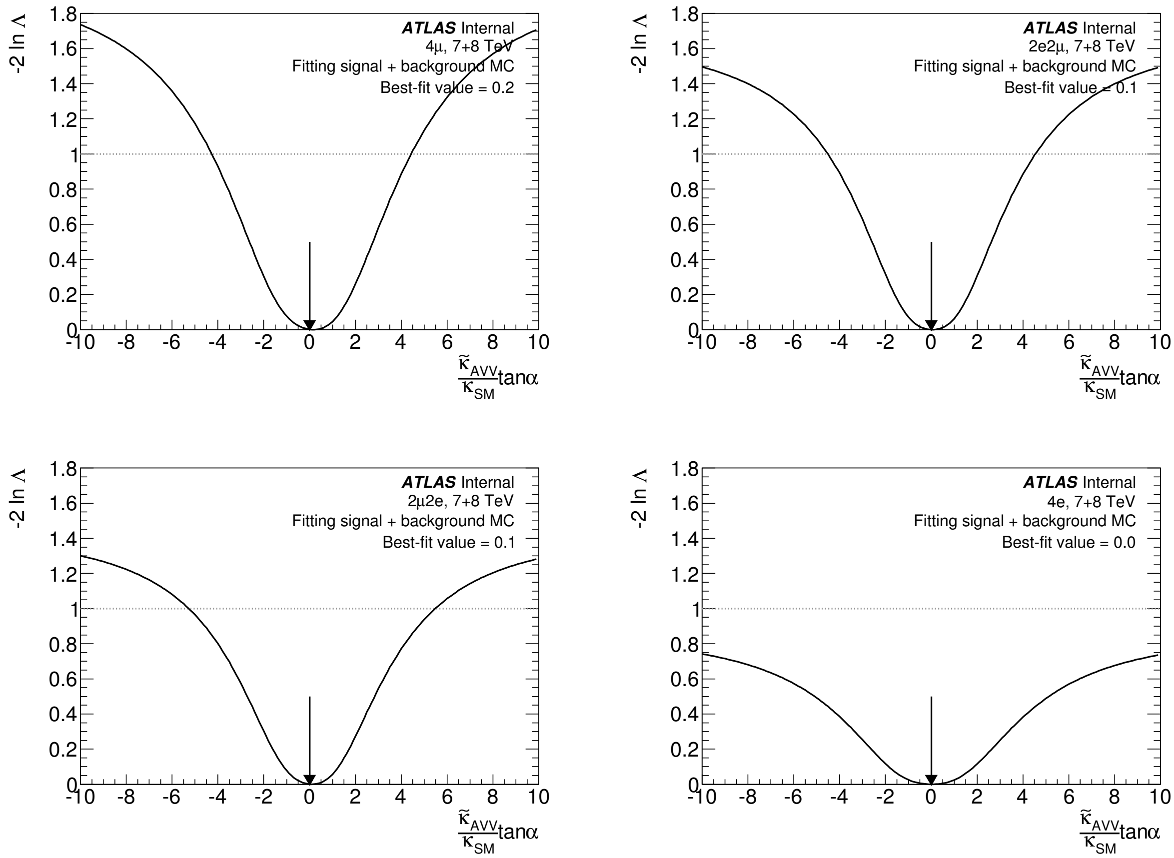

Figure 4.25: Validation checks of the signal and background model for measurements of $\frac{\tilde{\kappa}_{AVV}}{\kappa_{SM}} \tan\alpha$ in each final state. The likelihood curves are produced by fitting to unbinned signal and background MC events corresponding to $\frac{\tilde{\kappa}_{AVV}}{\kappa_{SM}} \tan\alpha = \frac{\tilde{\kappa}_{HVV}}{\kappa_{SM}} = 0$, neglecting systematics. The fitted MC is independent from the MC used to derive the model. The arrow points to the MC value of the fitted parameter of 0, and the corresponding measured value is written on the plot. Small fluctuations in the measured value on the order of 0.1 are expected due to finite MC statistics. The likelihood curves are not perfectly smooth in some areas because the value is calculated at discrete points to save time. For final measurements the likelihood is calculated at more points so the curve is smooth.

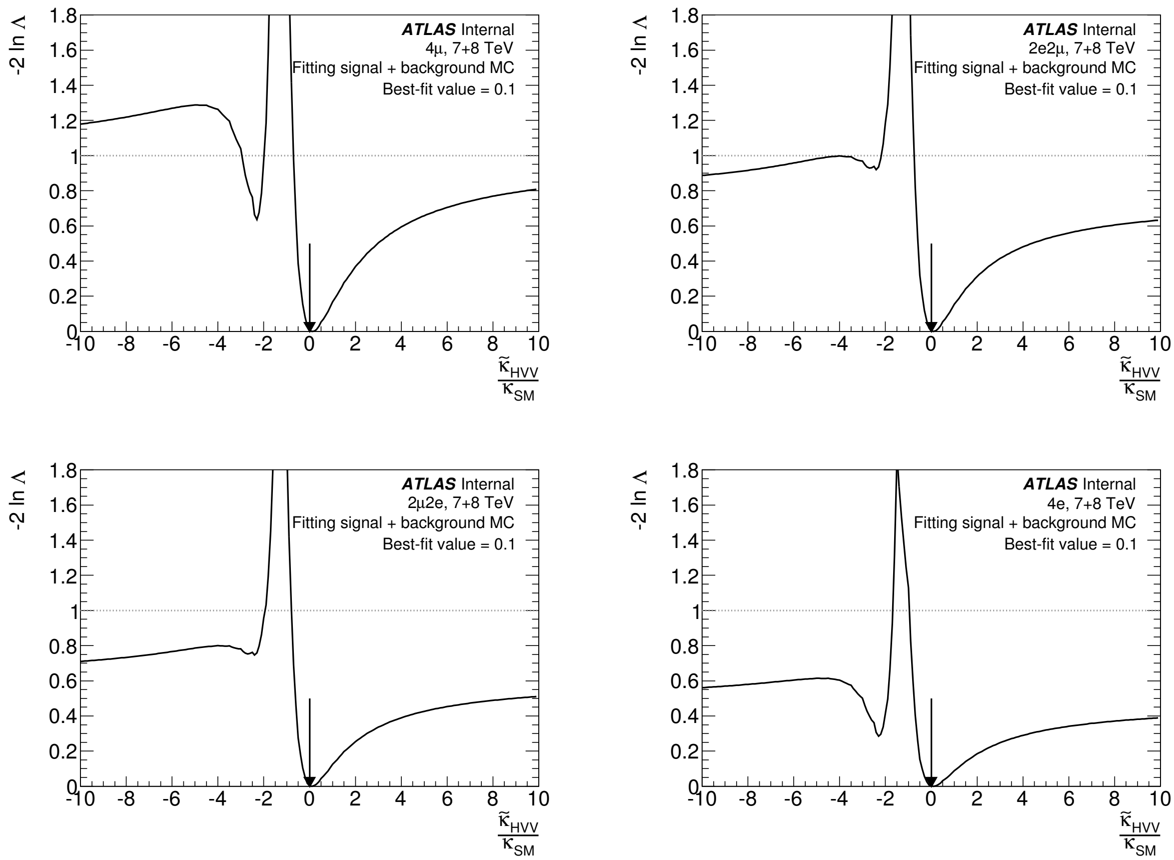

Figure 4.26: Validation checks of the signal and background model for measurements of $\frac{\tilde{\kappa}_{HVV}}{\kappa_{SM}}$ in each final state. The likelihood curves are produced by fitting to unbinned signal and background MC events corresponding to $\frac{\tilde{\kappa}_{AVV}}{\kappa_{SM}} \tan\alpha = \frac{\tilde{\kappa}_{HVV}}{\kappa_{SM}} = 0$, neglecting systematics. The fitted MC is independent from the MC used to derive the model. The arrow points to the MC value of the fitted parameter of 0, and the corresponding measured value is written on the plot. Small fluctuations in the measured value on the order of 0.1 are expected due to finite MC statistics. The likelihood curves are not perfectly smooth in some areas because the value is calculated at discrete points to save time. For final measurements the likelihood is calculated at more points so the curve is smooth.

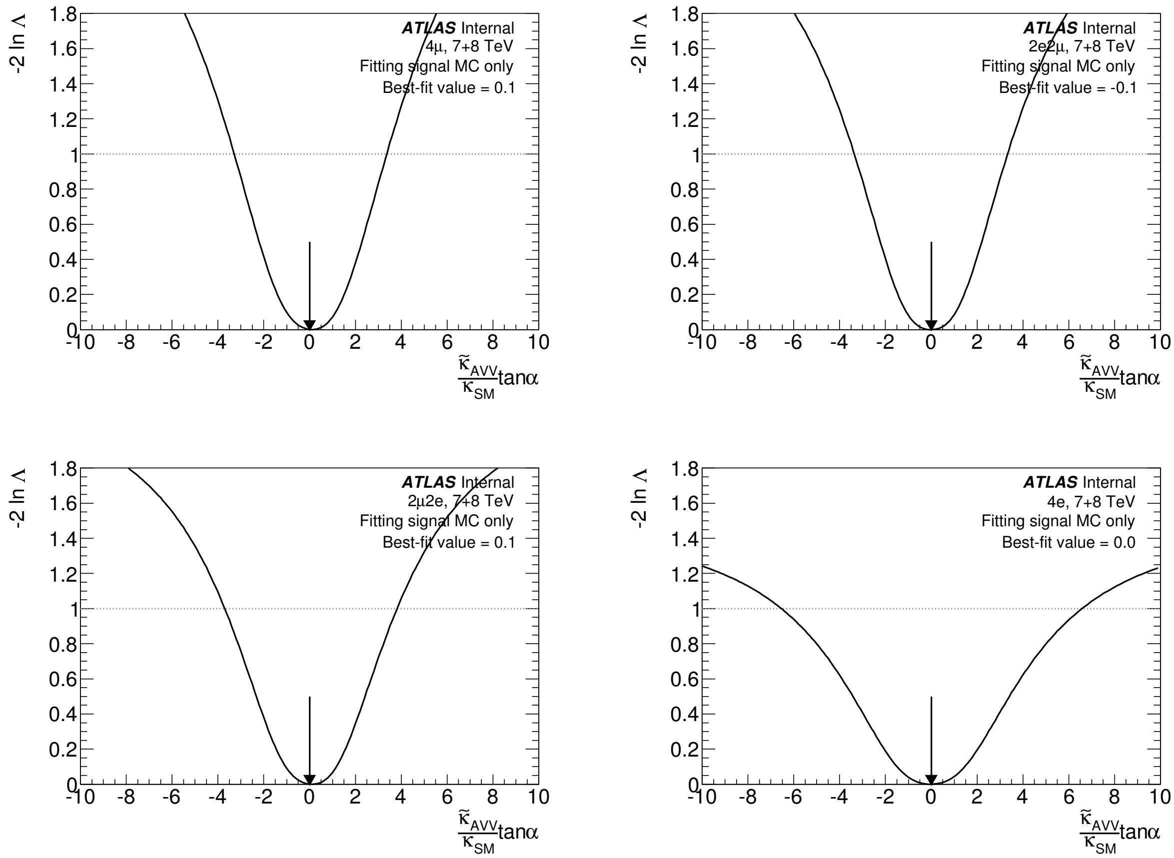

Figure 4.27: Validation checks of the signal model without background for measurements of $\frac{\tilde{\kappa}_{AVV}}{\kappa_{SM}}\tan\alpha$ in each final state. The likelihood curves are produced by fitting to unbinned signal MC events corresponding to $\frac{\tilde{\kappa}_{AVV}}{\kappa_{SM}}\tan\alpha = \frac{\tilde{\kappa}_{HVV}}{\kappa_{SM}} = 0$, neglecting systematics. The fitted MC is independent from the MC used to derive the model. The arrow points to the MC value of the fitted parameter of 0, and the corresponding measured value is written on the plot. Small fluctuations in the measured value on the order of 0.1 are expected due to finite MC statistics. The likelihood curves are not perfectly smooth in some areas because the value is calculated at discrete points to save time. For final measurements the likelihood is calculated at more points so the curve is smooth.

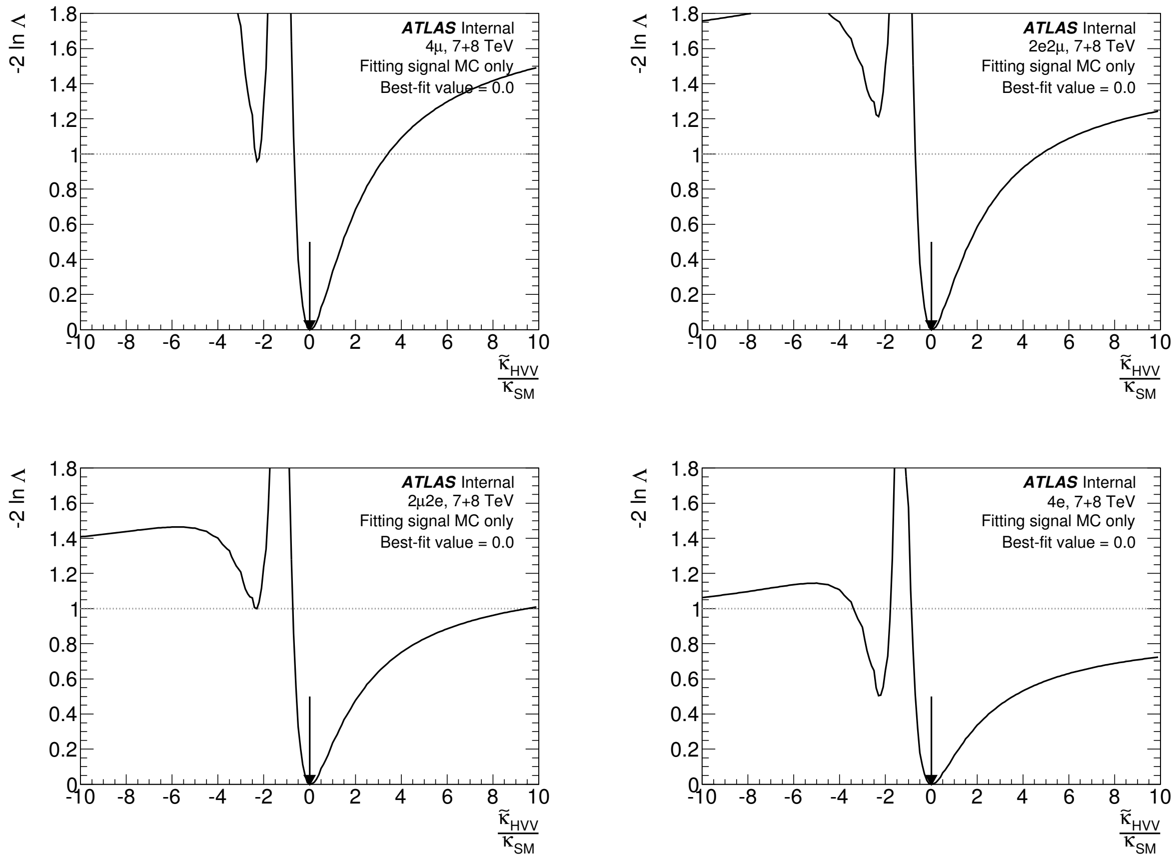

Figure 4.28: Validation checks of the signal model without background for measurements of $\frac{\tilde{\kappa}_{HVV}}{\kappa_{SM}}$ in each final state. The likelihood curves are produced by fitting to unbinned signal MC events corresponding to $\frac{\tilde{\kappa}_{AVV}}{\kappa_{SM}} \tan\alpha = \frac{\tilde{\kappa}_{HVV}}{\kappa_{SM}} = 0$, neglecting systematics. The fitted MC is independent from the MC used to derive the model. The arrow points to the MC value of the fitted parameter of 0, and the corresponding measured value is written on the plot. Small fluctuations in the measured value on the order of 0.1 are expected due to finite MC statistics. The likelihood curves are not perfectly smooth in some areas because the value is calculated at discrete points to save time. For final measurements the likelihood is calculated at more points so the curve is smooth.

the limited luminosity. However, systematic uncertainties from theory, simulation, and data-driven measurements can also impact the result. Such systematics are evaluated so that their impact is understood. The largest systematic uncertainties are included in measurements to ensure that the results are unbiased and that the overall uncertainty is fully characterized.

Systematic uncertainties can impact the measurement in two ways: they can influence the expected number of signal and background events in each final state, and they can alter the shape of the signal and background pdfs. Uncertainties that only impact the expected event yields are referred to a "normalization" uncertainties. Those that impact the shapes of pdfs are referred to as "shape" uncertainties. It is also possible for a single systematic uncertainty to impact both normalization and shape. In any case, the sources of uncertainty are included in the fit by introducing nuisance parameters to the likelihood function. A different systematic nuisance parameter is added for each independent source of uncertainty (so they are uncorrelated). Each parameter is constrained by a Gaussian function with a mean value set to the nominal value and a width set to the 1σ uncertainty on the parameter. The parameters are then free to float to their maximum likelihood values (profiled) in fits.

There are approximately 65 different sources of systematic uncertainty investigated for this analysis. Tables 4.6 and 4.7 list the dominant normalization uncertainties and their corresponding impact on the expected signal and ZZ background yields for each final state lepton flavor combination. This separation of final states is useful because some systematics uncertainties only correspond to muons, and some only correspond to electrons. Most of the uncertainties are briefly summarized in the following section. A more detailed description of the systematic uncertainties can be found in Ref. [62]

4.7.1 Dominant Sources of Uncertainty

The dominant systematic uncertainties associated with theory are listed below:

> **Parton distribution functions:** MC generation is done using parton distribution functions to specify the momentum fractions carried by partons entering the hard collision process. The uncertainty associated with these functions is evaluated by comparing multiple parton distribution functions from different sources. This variation changes the signal normalization by 7.5%, and the ZZ background normalization by 4.0% in all final states.

	Signal Normalization Uncertainty			
Source	4μ	$4e$	$2\mu 2e$	$2e2\mu$
QCD scale		7.8%		
Parton distribution functions		7.5%		
Branching fraction		4.2%		
Electron reconstruction & identification				
– IDStatHigh (Stat & ID, $E_{\mathrm{T}} > 20$ GeV)	–	2.7%	1.0%	1.7%
– IDLow (ID, $E_{\mathrm{T}} < 20$ GeV)	–	1.6%	1.4%	0.2%
– RecoHigh (Reco, $E_{\mathrm{T}} > 15$ GeV)	–	1.0%	0.7%	0.3%
– RecoLow (Reco, $E_{\mathrm{T}} < 15$ GeV)	–	2.5%	2.5%	0.2%
– Stat15 (Stat, $15 < E_{\mathrm{T}} < 20$ GeV)	–	0.8%	0.7%	0.1%
– Stat10 (Stat, $10 < E_{\mathrm{T}} < 15$ GeV)	–	0.9%	0.9%	0.1%
– Stat7 (Stat, $7 < E_{\mathrm{T}} < 10$ GeV)	–	0.6%	0.6%	0.0%
Electron isolation	–	3.3%	3.3%	0.1%
Muon reconstruction & identification	1.8%	–	0.8%	1.2%
Luminosity		1.8% (2011) or 2.8% (2012)		

Table 4.6: Systematic uncertainties on the SM Higgs signal normalizations in different final states. Each row is explained in the text. The numbers reported correspond to a center of mass energy of 8 TeV unless reported otherwise, but the uncertainties at 7 TeV are comparable. If an uncertainty is asymmetric then the larger value is reported.

	ZZ Background Normalization Uncertainty			
Source	4μ	$4e$	$2\mu 2e$	$2e2\mu$
QCD scale		3.0%		
Parton distribution functions		4.0%		
Electron reconstruction & identification				
– IDStatHigh (Stat & ID, $E_{\mathrm{T}} > 20$ GeV)	–	2.3%	0.6%	1.6%
– IDLow (ID, $E_{\mathrm{T}} < 20$ GeV)	–	1.8%	1.5%	0.2%
– RecoHigh (Reco, $E_{\mathrm{T}} > 15$ GeV)	–	0.9%	0.6%	0.3%
– RecoLow (Reco, $E_{\mathrm{T}} < 15$ GeV)	–	3.6%	3.6%	1.3%
– Stat15 (Stat, $15 < E_{\mathrm{T}} < 20$ GeV)	–	0.7%	0.6%	0.1%
– Stat10 (Stat, $10 < E_{\mathrm{T}} < 15$ GeV)	–	1.2%	1.2%	0.1%
– Stat7 (Stat, $7 < E_{\mathrm{T}} < 10$ GeV)	–	1.0%	1.0%	0.0%
Electron isolation	–	4.6%	4.5%	0.1%
Muon reconstruction & identification	2.1%	–	0.8%	1.4%
Luminosity		1.8% (2011) or 2.8% (2012)		

Table 4.7: Systematic uncertainties on the ZZ background normalizations in different final states. Each row is explained in the text. The numbers reported correspond to a center of mass energy of 8 TeV unless reported otherwise, but the uncertainties at 7 TeV are comparable. If an uncertainty is asymmetric then the larger value is reported.

QCD scales: The MC generation is also based on the QCD renormalization and factorization scales, μ_R and μ_F. The uncertainty from these parameters is evaluated by scaling the values up and down by a factor of two. This is found to have a 7.8% impact on the signal normalization, and a 3.0% impact on the ZZ background normalization.

Higgs branching fractions: The uncertainty in the branching fractions of the $H \to ZZ^*$ and $ZZ^* \to 4\ell$ decays can influence the number of expected events corresponding to a SM Higgs. This source of uncertainty is estimated to have a 4.2% impact on the signal normalization [48].

Reconstructed lepton candidates are required to pass a series of quality criteria before they are identified as electrons or muons. There are numerous sources of uncertainty associated with the efficiency for reconstructing and identifying leptons in the MC simulations. They are summarized below:

Electron reconstruction & identification: There are seven nuisance parameters included in the likelihood function to account for uncertainties in the electron reconstruction and identification efficiency. These include identification and reconstruction uncertainties that have a correlated impact on all electrons in each event, and statistical uncertainties that impact each electron in an uncorrelated way. The different correlated and uncorrelated uncertainties are divided into bins of the electron transverse energy, E_{T}. There are uncorrelated uncertainties for electrons with 7 GeV $< E_{\mathrm{T}} <$ 10 GeV (Stat7), 10 GeV $< E_{\mathrm{T}} <$ 15 GeV (Stat10), and 15 GeV $< E_{\mathrm{T}} <$ 20 GeV (Stat15). There are also correlated reconstruction uncertainties for electrons with $E_{\mathrm{T}} <$ 15 GeV (RecoLow) and $E_{\mathrm{T}} >$ 15 GeV (RecoHigh). Similarly, there is a correlated identification uncertainty for electrons with $E_{\mathrm{T}} <$ 20 GeV (IDLow). For electrons with $E_{\mathrm{T}} >$ 20 GeV the uncorrelated statistical uncertainty is combined with the correlated identification uncertainty (IDStatHigh). All of these components combined in quadrature have a 4.3% impact on the signal normalization and a 5.0% impact on the ZZ background normalization in the $4e$ final state.

Electron isolation: An additional uncertainty is included for the efficiency of an electron to pass the isolation and impact parameter significance criteria. This uncertainty is evaluated using a tag-and-probe method[3] with input from data and MC [63]. The estimated impact on the signal (ZZ background) normalization is 3.3% (4.6%) in the $4e$ final state.

Muon reconstruction & identification: The uncertainty on the efficiency for identifying and reconstructing muons is contained in a single nuisance parameter and is found to impact the signal (ZZ background) normalization by 1.8% (2.1%) in the 4μ final state.

Leptons in simulation are reconstructed based on measurements of the detector energy scale and resolution. Uncertainties associated with these measurements are treated as shape uncertainties. They have a negligibly small impact on normalization but they can affect the shapes of the signal and background pdfs. These uncertainties are summarized below:

Electron energy scale and resolution: The electron energy scale and resolution are determined by comparing $Z \rightarrow e^+e^-$ reconstructed mass distributions in data and simulation [62]. This is done in bins of electron η. There are 21 sources of uncertainty that enter the energy scale measurement. The largest energy scale uncertainties come from uncertainty in the amount of material in the detector. There are four uncertainties associated with with electron resolution, coming from detector material, pile-up, non-uniformity, and an intrinsic sampling term.

Muon energy scale and resolution: The muon reconstruction in simulation is based on measurements of $J/\psi \rightarrow \mu^+\mu-$ and $Z \rightarrow \mu^+\mu^-$ events in data. The measurements are done separately in the ID and MS in bins of muon p_{T} and η. One nuisance parameter is included in the likelihood function to account for the uncertainty in the muon energy scale. The muon resolution uncertainty is divided into two nuisance parameters: one associated with the ID and one associated with the MS.

Other uncertainties on the reducible background estimation and the integrated luminosity are summarized below:

3. The tag-and-probe method is technique for measuring object efficiencies in data by exploiting di-object resonances like the Z boson. Final states are identified by requiring one of the two decay products to pass a tight identification criteria (the tag) and the other to pass a loose identification criteria (the probe). The efficiency of the tight identification criteria can be measured by counting the number of probe objects that pass the tight criteria.

Reducible background: The reducible background contributions from $Z+$ jets, $t\bar{t}$, and WZ processes are estimated using data-driven extrapolations described in Section 4.3.3. Uncertainties from this method can impact the shape and normalization of the reducible background pdf. A description of the estimation of these uncertainties is included in Ref. [55]. There is roughly a 16% uncertainty on the reducible background normalization, depending slightly on the lepton flavors in each final state. The normalization and shape uncertainties for the reducible background are treated as uncorrelated. Four nuisance parameters are added to the likelihood function for each center of mass energy: two parameters control the shape and normalization of the pdf in final states where the subleading Z decays to electrons ($2\mu 2e$ and $4e$), and two parameters control the shape and normalization in final states where the subleading Z decays to muons ($2e2\mu$ and 4μ).

Luminosity: The integrated luminosity is measured using beam-separation scans, following the procedure described in Ref. [64]. There is a 2.8% (1.8%) uncertainty on the integrated luminosity in the 2012 (2011) dataset.

4.7.2 Ranking

Most of the systematic uncertainties listed in the previous section have a negligible impact on the measurement of BSM couplings. Including these excess nuisance parameters in the likelihood function introduces extra degrees of freedom and thereby makes fitting more computationally expensive. Thus, the systematic uncertainties are ranked according to their impact on the measurement and only the dominant uncertainties are included when computing results.

Rankings are done by comparing expected exclusions for different values of systematic nuisance parameters. First, an expected exclusion is calculated with no systematic uncertainties included in the fit (i.e. all systematics nuisance parameters are fixed to their nominal values). Then the exclusions are reevaluated after shifting each systematic nuisance parameter separately up and down by 1σ. The average of the absolute fractional shift in the exclusion significance is calculated for each parameter, averaging over the $\pm 1\sigma$ variations. Then the parameters are ranked according to this average. Rankings are produced at one benchmark point for each of the CP couplings parameters. The benchmark points are chosen where there are expected exclusions of roughly 2σ (since this is most relevant for setting 95% CL limits), at $\frac{\tilde{\kappa}_{AVV}}{\kappa_{SM}} \tan\alpha = 5$ and $\frac{\tilde{\kappa}_{HVV}}{\kappa_{SM}} = -0.8$.

Tables 4.8 and 4.9 show rankings of the top 20 systematic nuisance parameters for each of these benchmark points. All of the parameters are found to impact the expected exclusions by less than 1% when shifted by $\pm 1\sigma$, which confirms that the significance is dominated by statistical uncertainty. It is interesting to see that none of the signal normalization uncertainties appear in the top 20 lists. This is because the signal normalization is allowed to float in each fit. This degree of freedom overshadows any signal normalization uncertainty that is correlated between all final states. On the other hand, the luminosity uncertainty appears near the top of both rankings. This is because the luminosity uncertainty, together with the floating signal normalization, impacts the relative normalizations of signal and background. In both rankings, the uncertainties with the largest impact are the parton distribution function and QCD scale uncertainties on the ZZ background normalization, the luminosity uncertainty, and the reducible background shape and normalization uncertainties. These uncertainties (marked in bold in the tables) are included in the final measurement while the others are neglected. Note that the luminosity uncertainty and the reducible background uncertainty categories both consist of multiple nuisance parameters, and not all of the nuisance parameters in each category have an impact on the expected exclusions. For example, the 2011 luminosity uncertainty nuisance parameter has a much smaller impact than the 2012 nuisance parameter. However, all of the luminosity and reducible background nuisance parameters (even those with negligible impact) are included in the final result for completeness.

Other Uncertainties Associated with the Method

Two additional systematic uncertainties related to the construction of the signal and background pdfs are also evaluated:

Signal MC statistical uncertainty: The signal model is constructed using one-, two-, and three-dimensional MC templates for observable distributions and detector corrections. Uncertainties in these templates arise due to finite signal MC statistics. The impact from these uncertainties is measured by reproducing the MC templates after introducing Gaussian fluctuations to the model according the statistical uncertainty

Nuisance Parameter	-1σ Pull from NP Significance	-1σ Pull from NP Difference	$+1\sigma$ Pull from NP Significance	$+1\sigma$ Pull from NP Difference	Average Effect
Expected exclusion at $\frac{\tilde{\kappa}_{AVV}}{\kappa_{SM}} \tan\alpha = 5$ with no systematics	1.929σ	-	1.929σ	-	-
ZZ background PDFs	1.940σ	0.59%	1.917σ	-0.58%	0.58%
ZZ background QCD scale	1.938σ	0.48%	1.919σ	-0.47%	0.48%
Luminosity (2012)	1.938σ	0.47%	1.920σ	-0.46%	0.47%
Reducible norm, $\ell\ell\mu\mu$ (2012)	1.936σ	0.41%	1.921σ	-0.40%	0.40%
Reducible norm, $\ell\ell ee$ (2012)	1.935σ	0.36%	1.922σ	-0.34%	0.35%
Reducible shape, $\ell\ell\mu\mu$ (2012)	1.933σ	0.24%	1.935σ	0.33%	0.29%
Electron RecoLow (2012)	1.934σ	0.27%	1.923σ	-0.27%	0.27%
Electron isolation (2012)	1.933σ	0.26%	1.924σ	-0.25%	0.25%
Reducible shape, $\ell\ell ee$ (2012)	1.932σ	0.18%	1.932σ	0.20%	0.19%
Muon reco efficiency (2012)	1.932σ	0.17%	1.925σ	-0.17%	0.17%
Reducible norm, $\ell\ell ee$ (2011)	1.931σ	0.15%	1.926σ	-0.13%	0.14%
Reducible norm, $\ell\ell\mu\mu$ (2011)	1.931σ	0.13%	1.926σ	-0.12%	0.12%
Electron IDStatHigh (2012)	1.930σ	0.10%	1.927σ	-0.10%	0.10%
Electron IDLow (2012)	1.930σ	0.09%	1.927σ	-0.09%	0.09%
Reducible shape, $\ell\ell ee$ (2011)	1.930σ	0.07%	1.930σ	0.08%	0.08%
Electron Stat7 (2012)	1.930σ	0.07%	1.927σ	-0.07%	0.07%
Luminosity (2011)	1.929σ	0.05%	1.928σ	-0.05%	0.05%
Reducible shape, $\ell\ell\mu\mu$ (2011)	1.929σ	0.04%	1.929σ	0.05%	0.04%
Electron Stat15 (2012)	1.929σ	0.03%	1.928σ	-0.03%	0.03%
Muon resolution, MS (2012)	1.928σ	-0.03%	1.929σ	0.03%	0.03%

Table 4.8: Ranking of systematics nuisance parameters in descending order based on their impact on $-2\ln\Lambda(\frac{\tilde{\kappa}_{AVV}}{\kappa_{SM}}\tan\alpha = 5)$. The pulls are derived using pseudo-data generated from the nominal model and scaled to the integrated luminosity from Run I. The last column indicates the absolute average of the upward and downward differences. The uncertainties marked in bold are included in the final result as explained in the text.

Nuisance Parameter	-1σ Pull from NP Significance	Difference	$+1\sigma$ Pull from NP Significance	Difference	Average Effect
Expected exclusion at $\frac{\tilde{\kappa}_{HVV}}{\kappa_{SM}} = -0.8$ with no systematics	1.943σ	-	1.943σ	-	-
Reducible shape, $\ell\ell\mu\mu$ (2012)	1.934σ	-0.43%	1.938σ	-0.24%	0.33%
Reducible norm, $\ell\ell\mu\mu$ (2012)	1.948σ	0.27%	1.938σ	-0.25%	0.26%
Reducible norm, $\ell\ell ee$ (2012)	1.947σ	0.25%	1.938σ	-0.23%	0.24%
Reducible shape, $\ell\ell ee$ (2012)	1.937σ	-0.32%	1.940σ	-0.15%	0.23%
Reducible shape, $\ell\ell ee$ (2012)	1.938σ	-0.24%	1.940σ	-0.12%	0.18%
Luminosity (2012)	1.945σ	0.14%	1.940σ	-0.14%	0.14%
ZZ **background PDFs**	1.945σ	0.10%	1.941σ	-0.11%	0.10%
Reducible norm, $\ell\ell\mu\mu$ (2011)	1.945σ	0.10%	1.941σ	-0.08%	0.09%
ZZ **background QCD scale**	1.944σ	0.08%	1.941σ	-0.09%	0.08%
Reducible norm, $\ell\ell ee$ (2011)	1.944σ	0.08%	1.941σ	-0.07%	0.08%
Reducible shape $\ell\ell\mu\mu$ (2012)	1.941σ	-0.07%	1.942σ	-0.04%	0.05%
Electron isolation (2012)	1.943σ	0.04%	1.942σ	-0.05%	0.05%
Electron RecoLow (2012)	1.943σ	0.04%	1.942σ	-0.04%	0.04%
Muon reco efficiency (2012)	1.943σ	0.03%	1.942σ	-0.04%	0.03%
Electron resolution non-uniformity (2012)	1.944σ	0.06%	1.943σ	-0.01%	0.03%
Electron resolution pile-up (2012)	1.943σ	0.04%	1.943σ	0.02%	0.03%
Electron resolution sampling (2012)	1.943σ	0.03%	1.943σ	0.02%	0.03%
Electron energy scale (2012)	1.942σ	-0.01%	1.943σ	0.03%	0.02%
Electron resolution material (2012)	1.943σ	0.02%	1.942σ	-0.02%	0.02%
Luminosity (2011)	1.943σ	0.01%	1.942σ	-0.01%	0.01%

Table 4.9: Ranking of systematics nuisance parameters in descending order based on their impact on $-2\ln\Lambda(\frac{\tilde{\kappa}_{HVV}}{\kappa_{SM}} = -0.8)$. The pulls are derived using pseudo-data generated from the nominal model and scaled to the integrated luminosity from Run I. The last column indicates the absolute average of the upward and downward differences. The uncertainties marked in bold are included in the final result as explained in the text.

in each bin. The fluctuated models are then smoothed (using the standard treatment that is applied for the nominal analysis) and fit to SM pseudo-data generated from the nominal model before any fluctuations are added. The idea here is to see if a typical statistical fluctuation in the signal MC has a significant impact on the sensitivity of the measurement. The expected exclusion at $\frac{\tilde{\kappa}_{AVV}}{\kappa_{SM}} \tan\alpha = 5$ is evaluated for five different fluctuated models (using five different random seeds to produce the Gaussian fluctuations) and then compared to the nominal expected exclusion. The root-mean-square of the fractional differences in significance of the fluctuated and nominal exclusions is 0.27%. This uncertainty is neglected in the final measurement.

Background factorization: Correlations among $(\cos\theta_1, \cos\theta_2)$, Φ, and (m_{12}, m_{34}) are included in the signal pdf and neglected from the background functions, which could potentially cause a false separation between signal and background. There is not enough ZZ MC to include these correlations in the ZZ background pdf, so to check for false separation a new background model is constructed from templates using between 3 and 6 bins per observable. In this way, it is possible to populate a five-dimensional template for $(\cos\theta_1, \cos\theta_2, \Phi, m_{12}, m_{34})$ with the available MC. Then a competing ZZ shape is produced using the same coarse binning, but only including the nominal background correlations that are in the baseline analysis. Both models are fitted to SM MC and the significance of the exclusion at $\frac{\tilde{\kappa}_{AVV}}{\kappa_{SM}} \tan\alpha = 5$ is measured for both cases. The inclusion of additional correlations in the ZZ background pdf is found to improve the significance by 0.34%. Neglecting the correlations errs on the conservative side by a negligible amount, so this systematic uncertainty is not included in the final measurement.

4.8 Validation of the Asymptotic Approximation

To save computation time, the 68% and 95% CL intervals on CP coupling parameters are estimated using asymptotic formulae [58]. These formulae approximate the intervals assuming the profile-likelihood is distributed like a χ^2 function. The approximation is typically valid when the number of events included in the fit is greater than about 20.

Pseudo-experiments (toys) are used to verify that the approximation is valid for this measurement. For each pseudo-experiment, a set of pseudo-data is generated from the probability model using a particular CP coupling configuration $\boldsymbol{\alpha}$. The number of events per experiment is randomly drawn from a Poisson distribution with mean set to the total number of expected events in data. The datasets are then fitted to measure either $\frac{\tilde{\kappa}_{AVV}}{\kappa_{SM}} \tan\alpha$ or $\frac{\tilde{\kappa}_{HVV}}{\kappa_{SM}}$ and the resulting $-2\ln\Lambda(\boldsymbol{\alpha})$ is added to a histogram to produce a distribution of the profile-likelihood. Example profile-likelihood distributions are shown in Figures 4.29 and 4.30. The distributions are found to agree well with χ^2 distributions, as expected.

In addition, distributions of the measured values of $\frac{\tilde{\kappa}_{HVV}}{\kappa_{SM}}$ and $\frac{\tilde{\kappa}_{AVV}}{\kappa_{SM}} \tan\alpha$ from SM pseudo-experiments are shown in Figure 4.31. These distributions peak at 0, as expected. Note that the distribution for $\frac{\tilde{\kappa}_{HVV}}{\kappa_{SM}}$ is asymmetric, which is expected because the sensitivity to this parameter is asymmetric about $\frac{\tilde{\kappa}_{HVV}}{\kappa_{SM}} = 0$, as explained in Section 4.6.3.

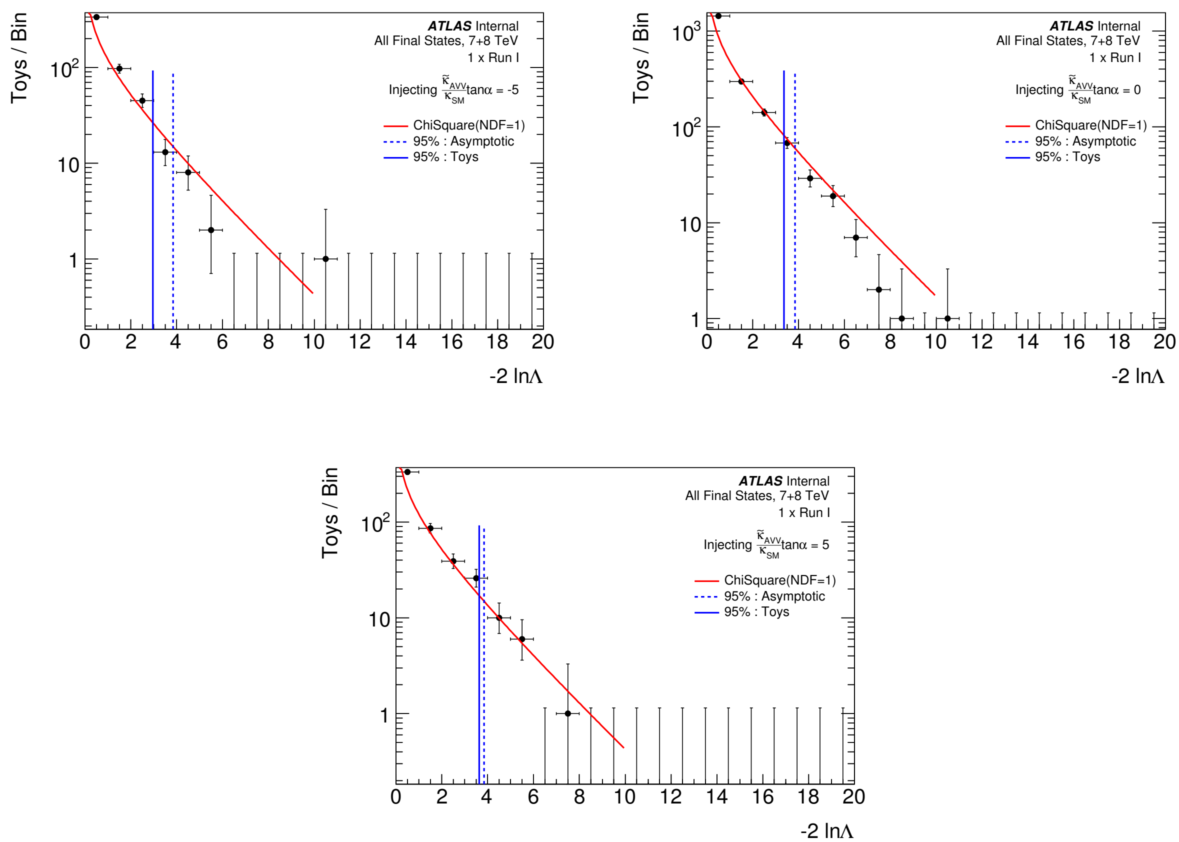

Figure 4.29: Distributions of $-2\ln\Lambda$ produced from pseudo-experiments (toys) when measuring $\frac{\tilde{\kappa}_{AVV}}{\kappa_{SM}}\tan\alpha$ with $\frac{\tilde{\kappa}_{HVV}}{\kappa_{SM}}$ fixed at 0. Pseudo-experiments are generated from the model for $\frac{\tilde{\kappa}_{AVV}}{\kappa_{SM}}\tan\alpha = 0$ and ±5. The $\frac{\tilde{\kappa}_{AVV}}{\kappa_{SM}}\tan\alpha$ values are included in the plot labels. In the asymptotic regime the distributions are approximated by a χ^2 function with one degree of freedom (red), making the 95% CL exclusion at $-2\ln\Lambda > 3.84$ (shown in dashed blue). This is compared to the 95% CL exclusion measured directly from pseudo-experiments (solid blue). The distributions are produced using either 2000 experiments (for $\frac{\tilde{\kappa}_{AVV}}{\kappa_{SM}}\tan\alpha = 0$) or 500 experiments (for $\frac{\tilde{\kappa}_{AVV}}{\kappa_{SM}}\tan\alpha = \pm5$).

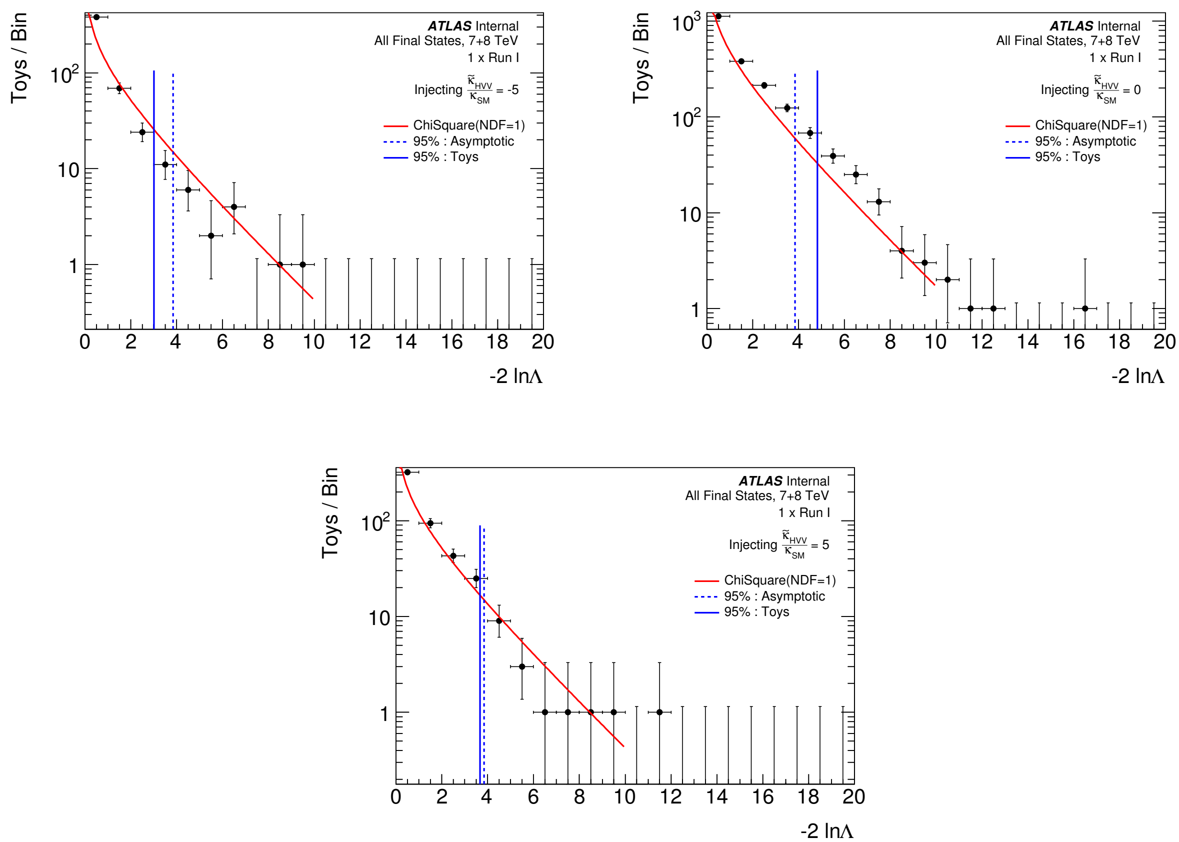

Figure 4.30: Distributions of $-2 \ln \Lambda$ produced from pseudo-experiments (toys) when measuring $\frac{\tilde{\kappa}_{HVV}}{\kappa_{SM}}$ with $\frac{\tilde{\kappa}_{AVV}}{\kappa_{SM}} \tan\alpha$ fixed at 0. Pseudo-Experiments are generated from the model for $\frac{\tilde{\kappa}_{HVV}}{\kappa_{SM}} = 0$ and ± 5. The $\frac{\tilde{\kappa}_{HVV}}{\kappa_{SM}}$ values are included in the plot labels. In the asymptotic regime the distributions are approximated by a χ^2 function with one degree of freedom (red), making the 95% CL exclusion at $-2 \ln \Lambda > 3.84$ (shown in dashed blue). This is compared to the 95% CL exclusion measured directly from pseudo-experiments (solid blue). The distributions are produced using either 2000 experiments (for $\frac{\tilde{\kappa}_{HVV}}{\kappa_{SM}} = 0$) or 500 experiments (for $\frac{\tilde{\kappa}_{HVV}}{\kappa_{SM}} = \pm 5$).

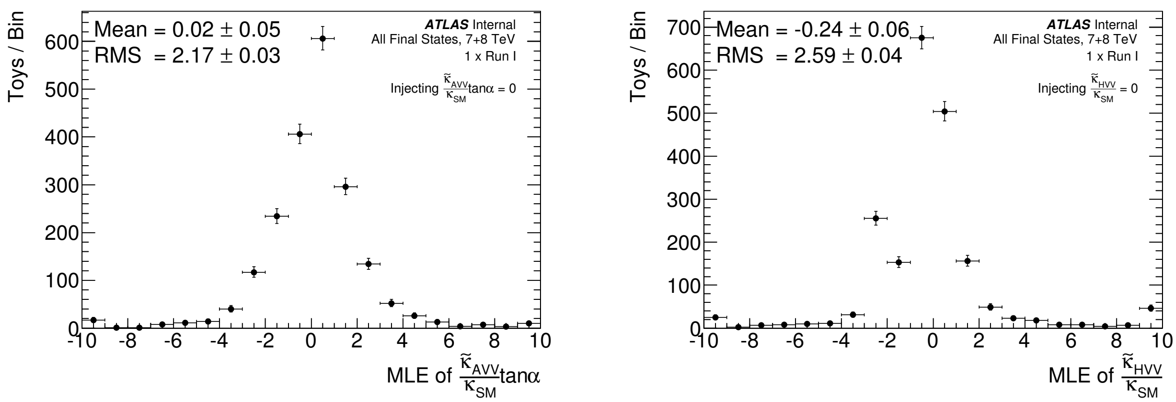

Figure 4.31: Distributions of the maximum likelihood estimates for $\frac{\tilde{\kappa}_{AVV}}{\kappa_{SM}} \tan\alpha$ (left) and $\frac{\tilde{\kappa}_{HVV}}{\kappa_{SM}}$ (right). The distributions are produced from 2000 pseudo-experiments (toys) generated from the model assuming SM values for $\frac{\tilde{\kappa}_{AVV}}{\kappa_{SM}} \tan\alpha$ and $\frac{\tilde{\kappa}_{HVV}}{\kappa_{SM}}$. The asymmetry in the maximum likelihood estimates for $\frac{\tilde{\kappa}_{HVV}}{\kappa_{SM}}$ is expected because the sensitivity to this parameter is not symmetric about zero. The peak in the expected exclusion occurs at roughly $\frac{\tilde{\kappa}_{HVV}}{\kappa_{SM}} = -1.5$, where there is a dip in the histogram.

Chapter 5
Results

The full analysis described in the previous chapter was applied to MC and tested for validity before any data was viewed. Results are presented in this chapter. Figures 5.1 and 5.2 show the data from Run I projected onto each discriminant observable. The shapes of the observed distributions appear to be roughly consistent with a SM Higgs hypothesis. The distributions from data are generally higher than the prediction due to a fluctuation above the expected event yield (shown previously in Table 4.5), but the resulting yield is still consistent with the SM expectation. More quantitative comparisons are included throughout this chapter.

The BSM coupling factors are measured using the model and fit strategy described in the previous chapter. The measurements include only the dominant systematic uncertainties, i.e. the parton distribution function and QCD scale uncertainties on the ZZ background normalization, the reducible background shape and normalization uncertainties from data-driven methods, and the luminosity uncertainty. The two CP parameters, $\frac{\tilde{\kappa}_{AVV}}{\kappa_{SM}} \tan\alpha$ and $\frac{\tilde{\kappa}_{HVV}}{\kappa_{SM}}$, are measured individually. In addition, a combined fit is done to simultaneously measure both parameters. The signal strength μ and the Higgs mass m_H are always treated as unconstrained free parameters in order to maintain generality. The expected signal yield generally depends on the values of the BSM coupling factors. In principle, this information can be used to further constrain measurements, but it is neglected in this analysis to minimize the dependence on any particular model. The results are presented in the following sections.

5.1 Separate Measurements of Each Parameter

The CP coupling factors are measured by performing a likelihood fit to the Run I dataset using the method described in the previous chapter. Each is measured individually in intervals from -10 and $+10$. In each fit the alternate parameter is fixed to its SM value at zero. Expected results for the SM hypothesis are also computed for comparison with these measurements. These are obtained by fitting to a set of pseudo-data generated from the likelihood function with $\frac{\tilde{\kappa}_{AVV}}{\kappa_{SM}} \tan\alpha = \frac{\tilde{\kappa}_{HVV}}{\kappa_{SM}} = 0$, $\mu = 1$ and $m_H = 125.5$ GeV. The set of pseudo-data contains a large number of events (roughly two million) to minimize the impact from statistical fluctuations. Each event is given a small weight so that the sum of the event

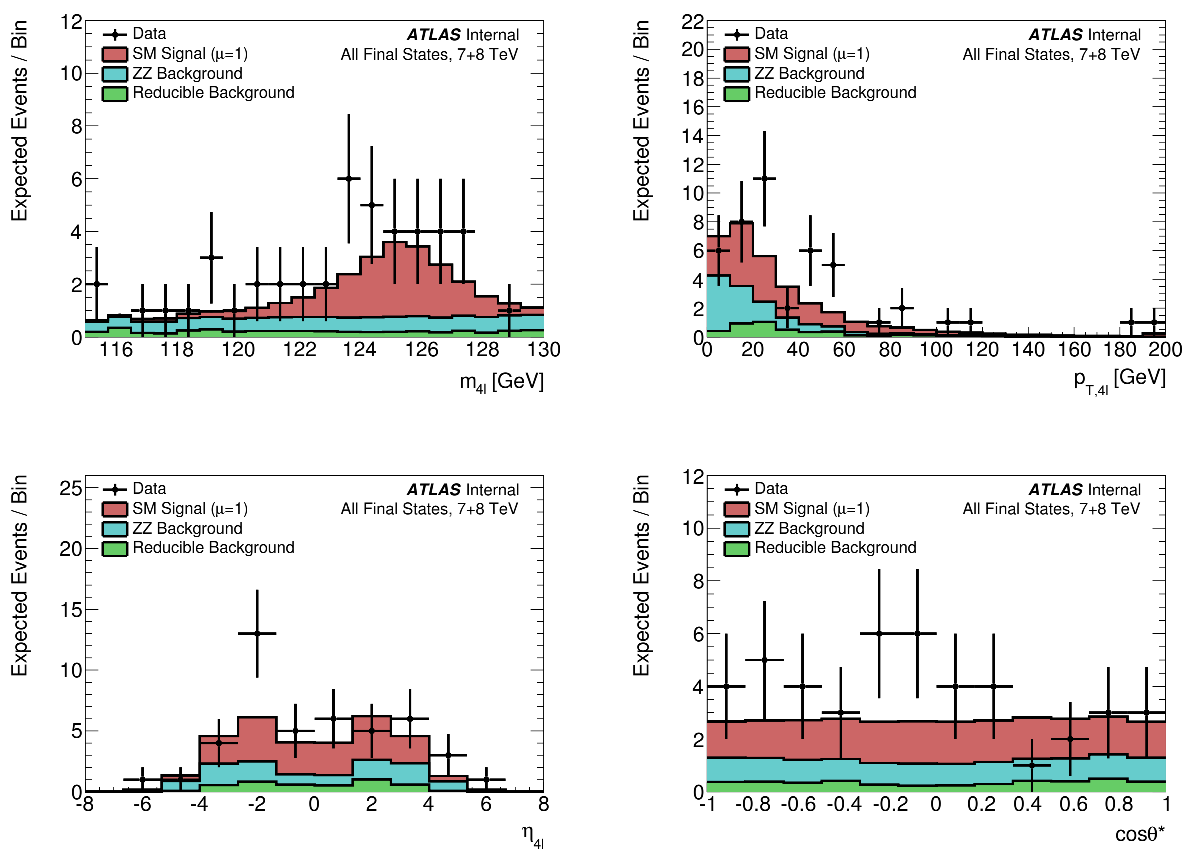

Figure 5.1: Observed and expected distributions of the observables used to discriminate signal from background. The data are indicated by the black points. The stacked histograms show the expected distributions from SM signal and background MC. All final states are combined.

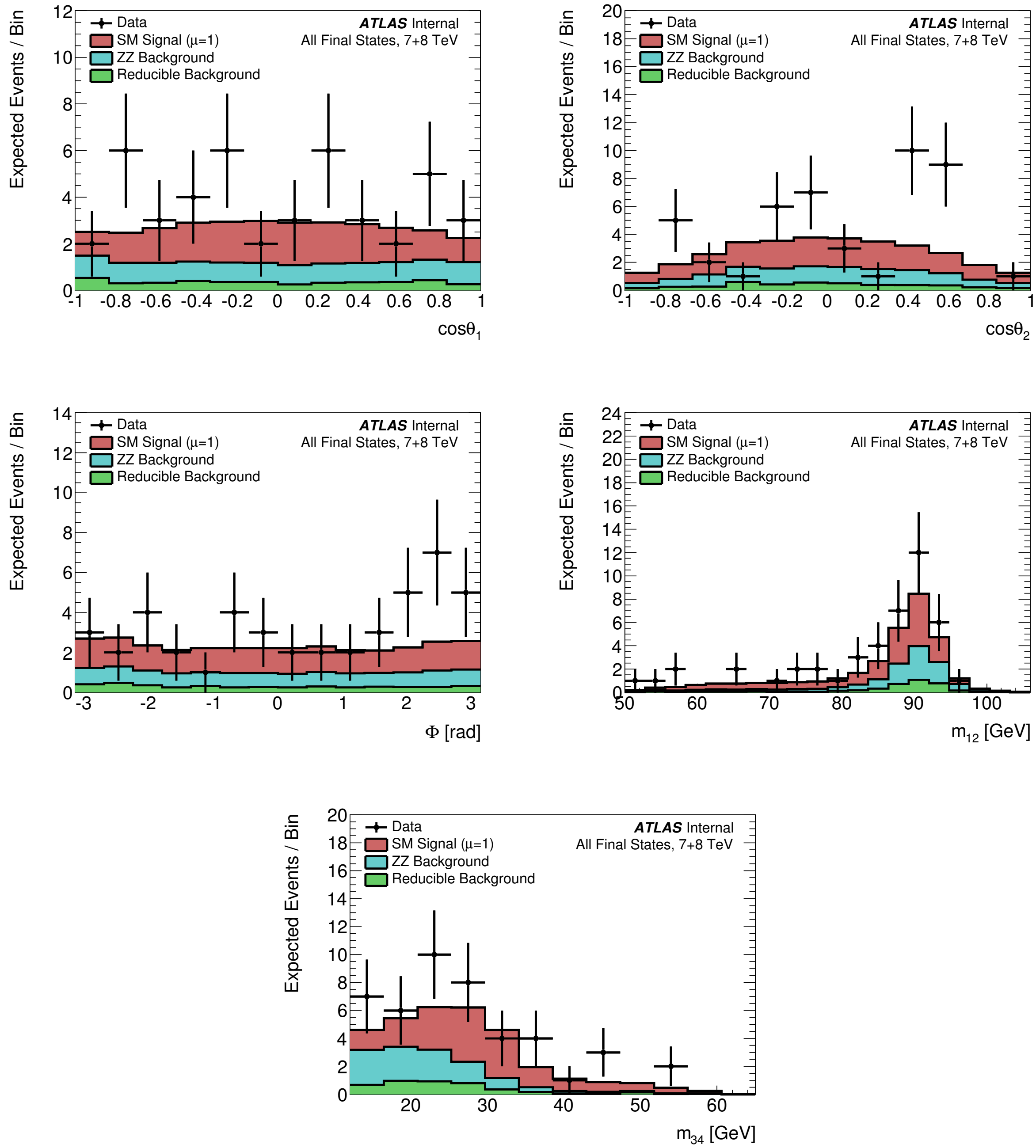

Figure 5.2: Observed and expected distributions of the observables that depend on parameters $\frac{\tilde{\kappa}_{AVV}}{\kappa_{SM}} \tan\alpha$ and $\frac{\tilde{\kappa}_{HVV}}{\kappa_{SM}}$. The data are indicated by the black points. The stacked histograms show the expected distributions from SM signal and background MC. All final states are combined.

weights is equal to the total number of expected events. An alternative method is to compute expected results by fitting directly to MC events. Pseudo-data is used instead because it is found to be compatible with the MC, and it allows larger datasets to be generated with better coverage of the observable space.

Fits are done to this pseudo-data both with and without the systematic nuisance parameters to better understand the impact from systematic uncertainties. The comparison is shown in Figure 5.3. The best-fit values are zero for both $\frac{\tilde{\kappa}_{AVV}}{\kappa_{SM}} \tan\alpha$ and $\frac{\tilde{\kappa}_{HVV}}{\kappa_{SM}}$, as expected. The sensitivity to $\frac{\tilde{\kappa}_{HVV}}{\kappa_{SM}}$ is asymmetric about zero due to an asymmetry in the matrix element distribution. The dominant systematic uncertainties impact the expected 95% CL interval for $\frac{\tilde{\kappa}_{AVV}}{\kappa_{SM}} \tan\alpha$ by less than 1%, causing the two likelihood distributions to overlap in the figure.

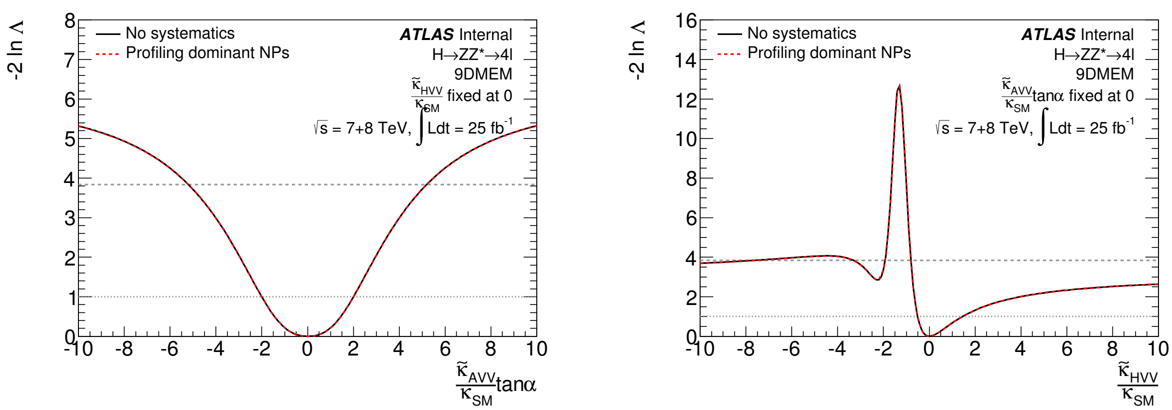

Figure 5.3: Expected fits for $\frac{\tilde{\kappa}_{AVV}}{\kappa_{SM}} \tan\alpha$ (left) and $\frac{\tilde{\kappa}_{HVV}}{\kappa_{SM}}$ (right) before and after including systematic uncertainties. The distributions of $-2\ln\Lambda$ are shown with all systematic nuisance parameters fixed to their nominal values (black) and with the dominant systematic nuisance parameters allowed to float (dashed red). The red curve appears dashed because it overlaps with the black curve. The dominant systematics included are the parton distribution function and QCD scale uncertainties on the ZZ background normalization, the reducible background shape and normalization uncertainties from data-driven methods, and the luminosity uncertainty.

In Figure 5.4, the expected fits are shown for each individual final state. The sensitivity is best in the 4μ final state where the expected signal yield is largest. The $4e$ final state has the least sensitivity since it has the lowest expected signal yield and the worst $m_{4\ell}$ resolution. These separate final state measurements are done with systematic uncertainties neglected for simplicity.

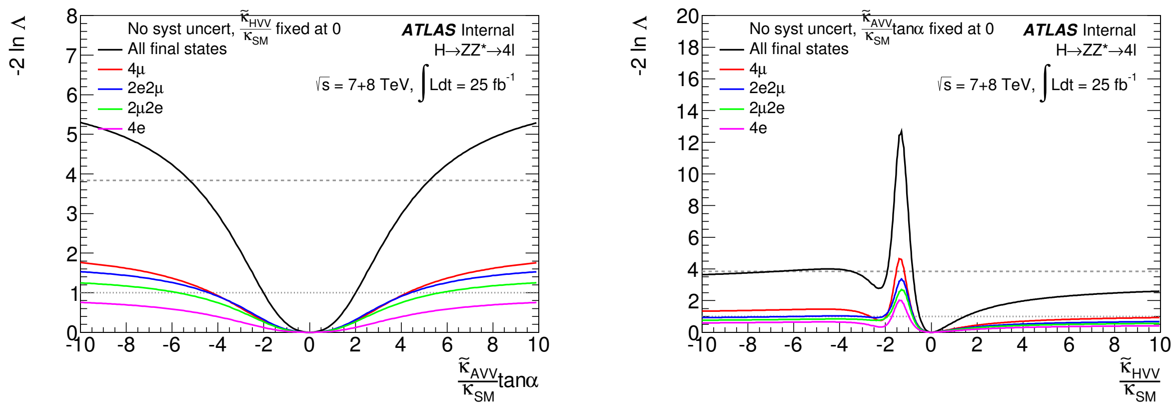

Figure 5.4: Expected distributions of $-2\ln\Lambda$ for $\frac{\tilde{\kappa}_{HVV}}{\kappa_{SM}}$ (left) and $\frac{\tilde{\kappa}_{AVV}}{\kappa_{SM}}\tan\alpha$ (right) in each final state and for the combined final states, neglecting all systematics.

The observed measurements of $\frac{\tilde{\kappa}_{AVV}}{\kappa_{SM}}\tan\alpha$ and $\frac{\tilde{\kappa}_{HVV}}{\kappa_{SM}}$ are shown in Figure 5.5 with the expected results. The maximum likelihood estimate for $\frac{\tilde{\kappa}_{AVV}}{\kappa_{SM}}\tan\alpha$ is found to be $-0.91^{+0.85}_{-0.96}$ assuming $\frac{\tilde{\kappa}_{HVV}}{\kappa_{SM}} = 0$. The maximum likelihood estimate for $\frac{\tilde{\kappa}_{HVV}}{\kappa_{SM}}$ is found to be $-0.36^{+0.42}_{-0.26}$ assuming $\frac{\tilde{\kappa}_{AVV}}{\kappa_{SM}}\tan\alpha = 0$. Both measurements are consistent with the SM. The best-fit values for μ and m_H at $\frac{\tilde{\kappa}_{AVV}}{\kappa_{SM}}\tan\alpha = \frac{\tilde{\kappa}_{HVV}}{\kappa_{SM}} = 0$ are found to be 1.71 and 124.62 GeV, respectively. These values are consistent with similar dedicated measurements of μ and m_H targeting the same $H \to ZZ^* \to 4\ell$ decay [62]. Both μ and m_H have very little dependence on the CP parameters.

There are two expected likelihood curves plotted with the data in Figure 5.5. The dashed blue curve is derived from a fit to pseudo-data generated assuming all the nuisance parameters (including μ and m_H) are fixed to their expected values. The dashed red curve, on the other hand, is derived from pseudo-data generated with nuisance parameters set to their values measured in data at $\frac{\tilde{\kappa}_{AVV}}{\kappa_{SM}}\tan\alpha = \frac{\tilde{\kappa}_{HVV}}{\kappa_{SM}} = 0$. The latter expected results have a better 95% CL exclusion because of the enhanced μ measured in data. All of the expected and observed measurements are summarized in Table 5.1.

It is notable that the observed 95% CL exclusions are found to be better than expected, even after accounting for the enhanced signal strength measured in data. This is studied further using 300 pseudo-experiments with data generated from the model assuming $\frac{\tilde{\kappa}_{AVV}}{\kappa_{SM}}\tan\alpha = \frac{\tilde{\kappa}_{HVV}}{\kappa_{SM}} = 0$. The number of events in each experiment is drawn randomly from a Poisson distribution with a mean value set to the expected total yield corresponding

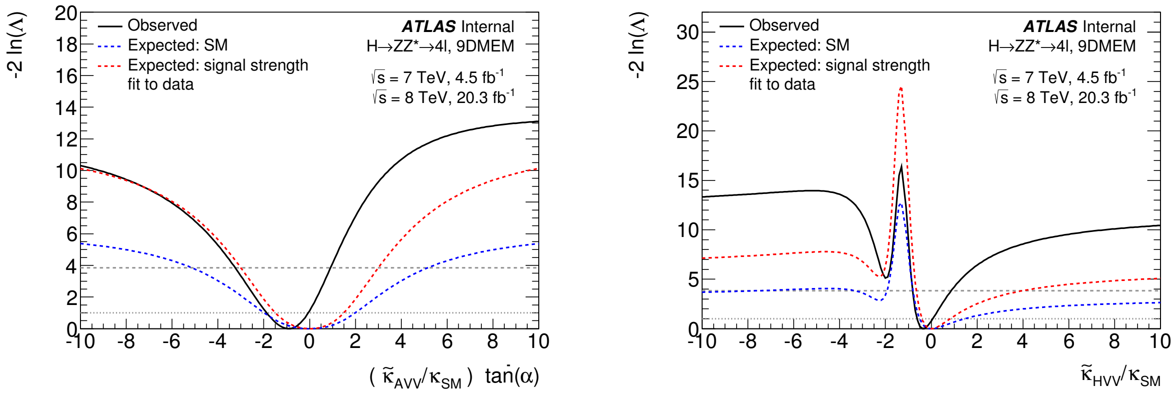

Figure 5.5: Expected and observed distributions of $-2\ln\Lambda$ as function of $\frac{\tilde{\kappa}_{AVV}}{\kappa_{SM}}\tan\alpha$ (left) and $\frac{\tilde{\kappa}_{HVV}}{\kappa_{SM}}$ (right). In both figures the red dashed line represents the expectation for a SM Higgs using the signal strength measured from the data under the SM assumption ($\mu = 1.71$). The blue dashed lines represent the SM expectation assuming $\mu = 1$. The regions excluded at the 68 % and 95 % CL are indicated by the gray dashed lines at 1 and 3.84, respectively. It can be seen that the fitted coupling ratios are in good agreement with the SM.

Dataset	Best fit value	Regions excluded at 95% CL
Measurement of $\frac{\tilde{\kappa}_{AVV}}{\kappa_{SM}}\tan\alpha$ assuming $\frac{\tilde{\kappa}_{HVV}}{\kappa_{SM}} = 0$		
Observed	$-0.91^{+0.85}_{-0.96}$	< -3.24 and > 0.91
Expected: SM	$0.00^{+1.99}_{-1.98}$	< -5.12 and > 5.14
Expected: NPs fit to data	$0.00^{+1.49}_{-1.49}$	< -2.99 and > 2.99
Measurement of $\frac{\tilde{\kappa}_{HVV}}{\kappa_{SM}}$ assuming $\frac{\tilde{\kappa}_{AVV}}{\kappa_{SM}}\tan\alpha = 0$		
Observed	$-0.36^{+0.42}_{-0.26}$	< -0.82 and > 0.87
Expected: SM	$0.00^{+1.46}_{-0.51}$	$[-7.48, -3.33]$ and $[-1.93, -0.80]$
Expected: NPs fit to data	$0.00^{+0.82}_{-0.40}$	< -0.65 and > 3.99

Table 5.1: Best fit values and observed exclusion regions for individual measurements of $\frac{\tilde{\kappa}_{AVV}}{\kappa_{SM}}\tan\alpha$ and $\frac{\tilde{\kappa}_{HVV}}{\kappa_{SM}}$. The expected results are derived by fitting to a set of pseudo-data generated from the fit model. The pseudo-data is generated with all nuisance parameters set to nominal SM values, and with all nuisance parameters set to the values measured in data with $\frac{\tilde{\kappa}_{AVV}}{\kappa_{SM}}\tan\alpha = \frac{\tilde{\kappa}_{HVV}}{\kappa_{SM}} = 0$.

to $\mu = 1.71$. A fit is performed to the dataset for each pseudo-experiment and the resulting ensemble of likelihood curves is used to derive uncertainty bands around the expected likelihood distributions. The resulting bands are compared to the observed fit results in Figure 5.6. The observed likelihood values are found to be within the expected 95% CL band over the entire range of each fit. The fluctuation away from the expected likelihood is found to be primarily due to the observed distribution of (m_{12}, m_{34}). The expected and observed results become much more compatible when these masses are removed from the likelihood function.

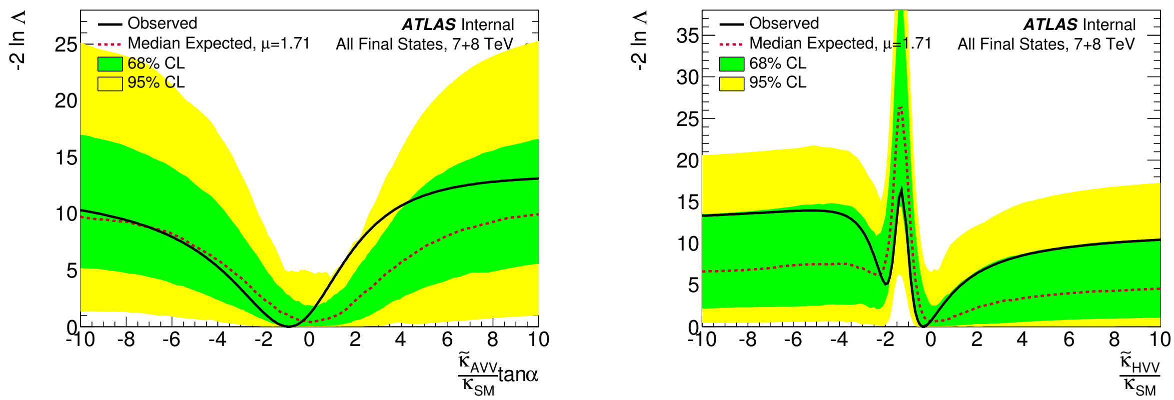

Figure 5.6: Expected $-2\ln\Lambda$ distributions of $\frac{\tilde{\kappa}_{AVV}}{\kappa_{SM}}\tan\alpha$ (left) and $\frac{\tilde{\kappa}_{HVV}}{\kappa_{SM}}$ (right) with uncertainty bands estimated from 300 pseudo-experiments generated assuming $\frac{\tilde{\kappa}_{HVV}}{\kappa_{SM}} = \frac{\tilde{\kappa}_{AVV}}{\kappa_{SM}}\tan\alpha = 0$ and $\mu = 1.71$. The dashed red line represents the median likelihood from the experiments, while the green and yellow bands represent the 68% and 95% CL intervals, respectively. The observed likelihood is shown in black.

The pseudo-experiments are used to calculate the probability for observing a SM exclusion with significance greater than or equal to the significance measured in data as an additional cross-check. In the measurement of $\frac{\tilde{\kappa}_{AVV}}{\kappa_{SM}}\tan\alpha$ the p-value for the observed SM exclusion is $27 \pm 3\%$ assuming $\mu = 1.71$. In the measurement of $\frac{\tilde{\kappa}_{HVV}}{\kappa_{SM}}$ the p-value for the observed SM exclusion is $46 \pm 3\%$ assuming $\mu = 1.71$.

5.2 Simultaneous Measurement of Both Parameters

In a generic scalar model it is possible for both $\frac{\tilde{\kappa}_{AVV}}{\kappa_{SM}}\tan\alpha$ and $\frac{\tilde{\kappa}_{HVV}}{\kappa_{SM}}$ to be nonzero. To probe this scenario, a likelihood fit is done to measure both parameters simultaneously. Figures 5.7

and 5.8 shows the observed and expected likelihood distributions in the two-dimensional plane of $\frac{\tilde{\kappa}_{HVV}}{\kappa_{SM}}$ versus $\frac{\tilde{\kappa}_{AVV}}{\kappa_{SM}}\tan\alpha$. The asymptotic interpretation of the likelihood is modified to account for the added dimension. Namely, the 68% CL contour is drawn at $-2\ln\Lambda = 2.3$ and the 95% CL contour is drawn at $-2\ln\Lambda = 6.0$. The observed best-fit value is found to be $\frac{\tilde{\kappa}_{AVV}}{\kappa_{SM}}\tan\alpha = -0.8^{+1.1}_{-1.3}$ and $\frac{\tilde{\kappa}_{HVV}}{\kappa_{SM}} = -0.5^{+0.8}_{-0.5}$, which is consistent with the SM. The expected likelihood distribution shown in Figure 5.8 is derived from fitting to pseudo-data generated with the assumption that $\mu = 1.71$. The expected and observed contours are plotted together in Figure 5.9.

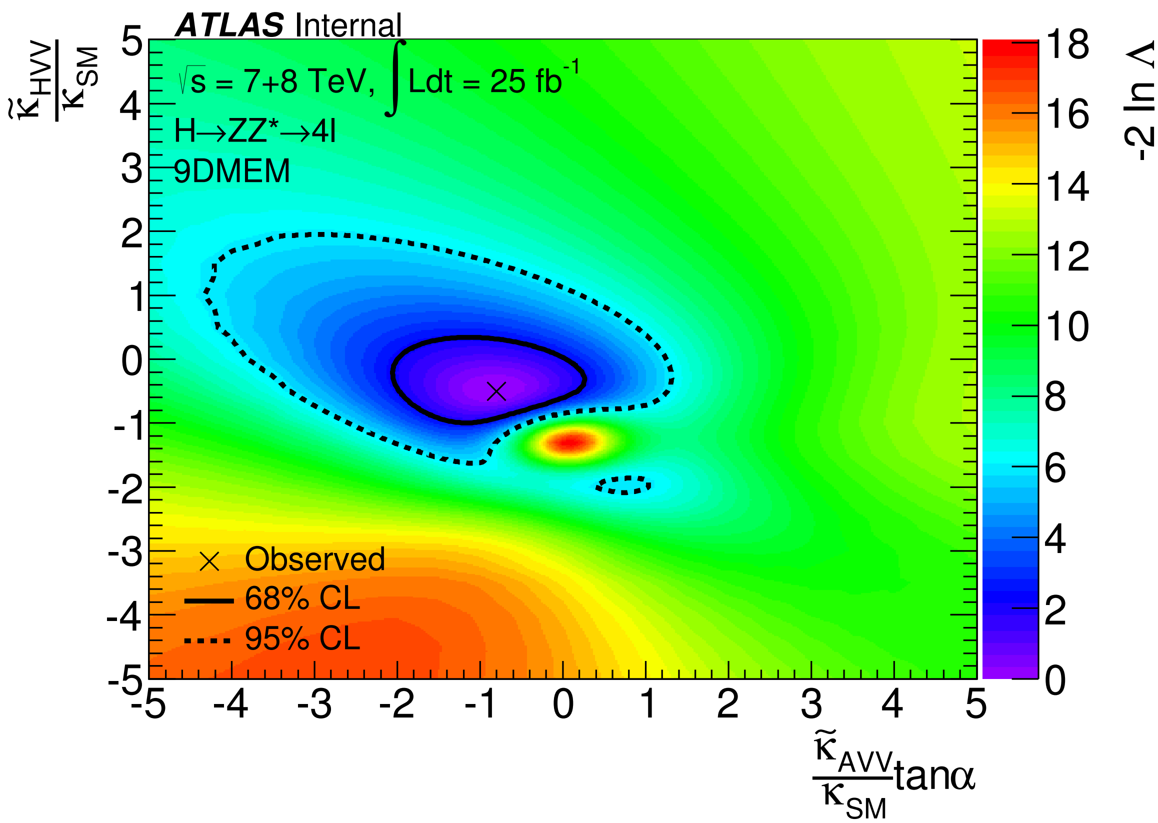

Figure 5.7: Observed likelihood distribution in the two-dimensional plane of $\frac{\tilde{\kappa}_{AVV}}{\kappa_{SM}}\tan\alpha$ versus $\frac{\tilde{\kappa}_{HVV}}{\kappa_{SM}}$. The 68% and 95% CL contours are indicated by the solid and dashed contours where the value of $-2\ln\Lambda$ equals 2.3 and 6.0, respectively.

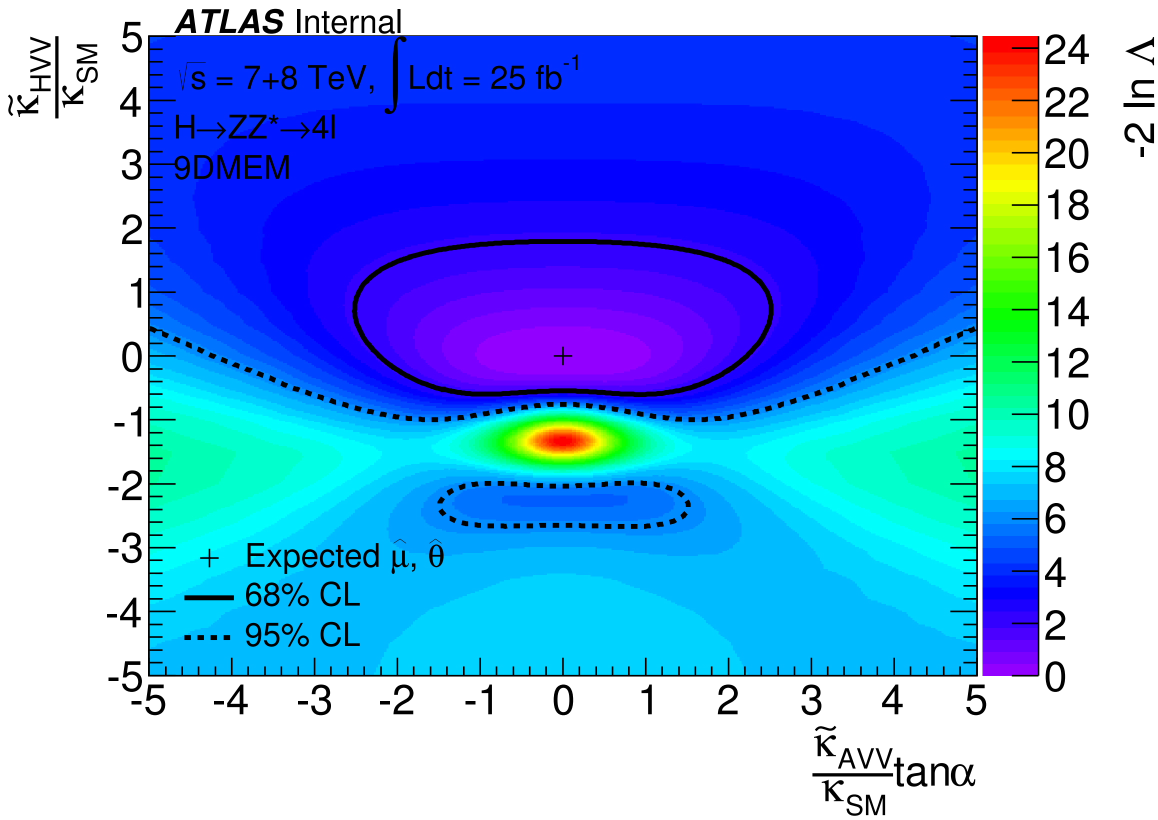

Figure 5.8: Expected likelihood distribution in the two-dimensional plane of $\frac{\tilde{\kappa}_{AVV}}{\kappa_{SM}} \tan\alpha$ versus $\frac{\tilde{\kappa}_{HVV}}{\kappa_{SM}}$, calculated assuming $\mu = 1.71$. The 68% and 95% CL contours are indicated by the solid and dashed contours where the value of $-2\ln\Lambda$ equals 2.3 and 6.0, respectively.

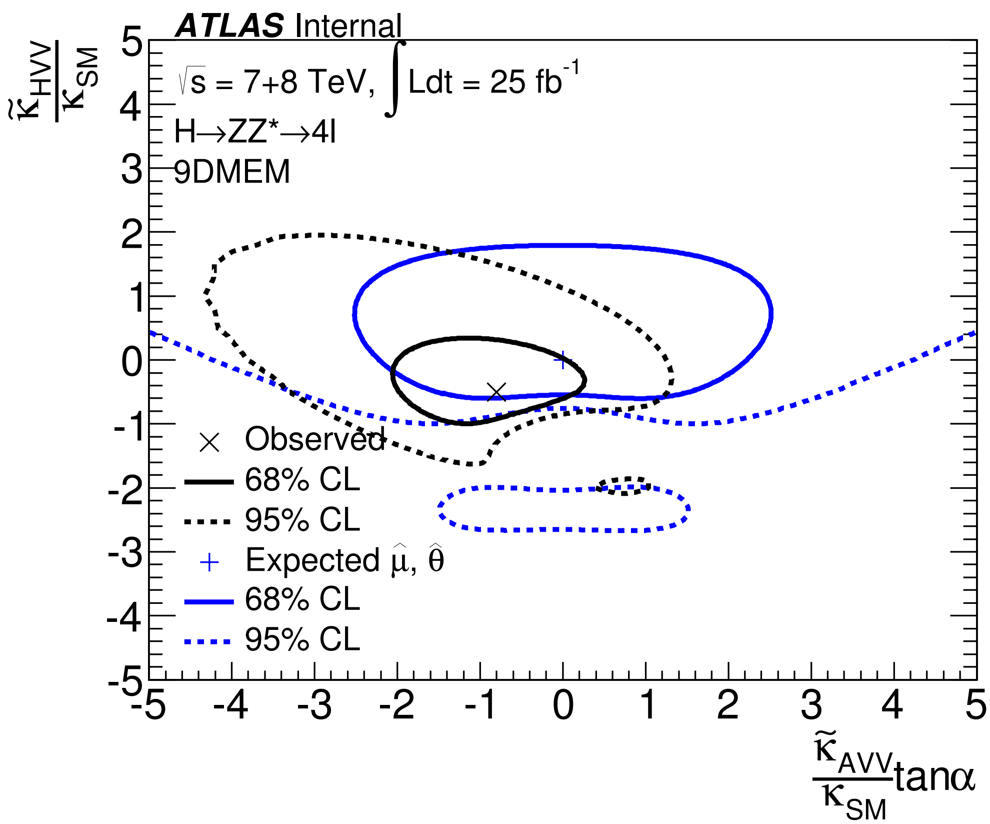

Figure 5.9: Observed and expected 68% and 95% CL regions in the two-dimensional plane of $\frac{\tilde{\kappa}_{AVV}}{\kappa_{SM}} \tan\alpha$ versus $\frac{\tilde{\kappa}_{HVV}}{\kappa_{SM}}$. The regions outside of the enclosed dashed contours are excluded at 95% CL.

Chapter 6

Combination with $H \to WW^*$

The measurement of non SM couplings in $H \to ZZ^* \to 4\ell$ is combined with a similar measurement based on $H \to WW^* \to e\nu\mu\nu$ decays. The combination is done using a slightly different analysis method for the $H \to ZZ^* \to 4\ell$ measurement. This chapter contains a short description of the alternate method followed by the combined results.

6.1 Matrix Element Observable Method

The nine-dimensional matrix element method (9DMEM) analysis described in Chapter 4 is cross-checked with an independent method for measuring non SM couplings in $H \to ZZ^* \to 4\ell$ events. The alternate method utilizes the same data and event selection, but a slightly different implementation of the likelihood function. It is called the Matrix Element Observable (ME-Obs) method. The ME-Obs methods was developed primarily by others, but I helped work on numerous validation checks.

The general idea of the ME-Obs method is to reduce the observable-space by collapsing the reconstructed masses and decay angles onto five multivariate discriminants that retain most of the sensitivity. One of the multivariate discriminants is a Boosted Decision Tree (BDT) designed to separate signal from the ZZ background. This is trained using observables that have little sensitivity to the non SM couplings: $m_{4\ell}$, $p_{T4\ell}$, $\eta_{4\ell}$, $\cos\theta^*$, and Φ_1. The observable Φ_1 is included here even though it is neglected in the 9DMEM analysis. This is because adding an extra observable to the BDT training is not computationally expensive, whereas including an extra dimension in the 9DMEM likelihood function makes fitting significantly slower.

The remaining four multi-variate discriminants are based on matrix element calculations for the $H \to ZZ^* \to 4\ell$ process:

$$\begin{aligned}
\mathcal{O}^1_{\text{odd}} &= \frac{2\Re\left(\mathcal{M}(\boldsymbol{x}|0^+)^* \cdot \mathcal{M}(\boldsymbol{x}|0^-)\right)}{|\mathcal{M}(0^-)|^2}, \\
\mathcal{O}^2_{\text{odd}} &= \frac{|\mathcal{M}(\boldsymbol{x}|0^-)|^2}{|\mathcal{M}(\boldsymbol{x}|0^+)|^2}, \\
\mathcal{O}^1_{\text{even}} &= \frac{2\Re\left(\mathcal{M}(\boldsymbol{x}|0^+)^* \cdot \mathcal{M}(\boldsymbol{x}|0^+_h)\right)}{|\mathcal{M}(\boldsymbol{x}|0^+)|^2}, \\
\mathcal{O}^2_{\text{even}} &= \frac{|\mathcal{M}(\boldsymbol{x}|0^+_h)|^2}{|\mathcal{M}(\boldsymbol{x}|0^+)|^2}.
\end{aligned} \tag{6.1}$$

Here, $\mathcal{M}$ represents the matrix element for signal and $\boldsymbol{x}$ is a vector of CP-dependent observables, i.e. $\cos\theta_1$, $\cos\theta_2$, Φ, m_{12}, and m_{34}. The 0^+_h signal hypothesis represents the parameterization where $\tilde{\kappa}_{HVV} = 1$ and $\kappa_{SM} = \tilde{\kappa}_{AVV}\tan\alpha = 0$. These discriminant definitions correspond to the first and second order "Optimal Observables" proposed for measuring BSM amplitudes [65]. The discriminant $\mathcal{O}^2_{\text{odd}}$ is a second order Optimal Observable sensitive to the magnitude of $\frac{\tilde{\kappa}_{AVV}}{\kappa_{SM}}\tan\alpha$. Meanwhile, $\mathcal{O}^1_{\text{even}}$ is a first order Observable that is primarily sensitive to the sign of $\frac{\tilde{\kappa}_{AVV}}{\kappa_{SM}}\tan\alpha$. Similarly, $\mathcal{O}^2_{\text{even}}$ is sensitive to the magnitude of $\frac{\tilde{\kappa}_{HVV}}{\kappa_{SM}}$ and $\mathcal{O}^1_{\text{even}}$ is primarily sensitive to the sign. More details on optimal observables are in Ref. [65], and the matrix elements in the above equations are fully defined in Ref. [3].

The ME-Obs method is used to make individual measurements of $\frac{\tilde{\kappa}_{AVV}}{\kappa_{SM}}\tan\alpha$ and $\frac{\tilde{\kappa}_{HVV}}{\kappa_{SM}}$. For each measurement a likelihood is constructed using three of the five multivariate discriminants. The fit for $\frac{\tilde{\kappa}_{AVV}}{\kappa_{SM}}\tan\alpha$ is done using the BDT, $\mathcal{O}^1_{\text{odd}}$, and $\mathcal{O}^2_{\text{odd}}$, while the fit for $\frac{\tilde{\kappa}_{HVV}}{\kappa_{SM}}$ is done using the BDT, $\mathcal{O}^1_{\text{even}}$, and $\mathcal{O}^2_{\text{even}}$. The signal and background pdfs used in the likelihood function are derived from simulated data using binned three-dimensional templates with all of the correlations included. A detailed description of the method is included in Ref. [19].

The ME-Obs and 9DMEM methods are compared by fitting to a common set of 300 SM pseudo-experiments populated with MC events. The CP coupling factors are measured using both methods in each pseudo-experiment. The resulting measurements of $\frac{\tilde{\kappa}_{AVV}}{\kappa_{SM}}\tan\alpha$ are shown in Figure 6.1. The results are found to be well correlated, as expected. Furthermore, the mean difference in the measured value of $\frac{\tilde{\kappa}_{AVV}}{\kappa_{SM}}\tan\alpha$ is consistent with zero, which confirms that the methods are compatible. Similar studies are done for $\frac{\tilde{\kappa}_{HVV}}{\kappa_{SM}}$ and μ and the corresponding results also confirm compatibility between the two methods.

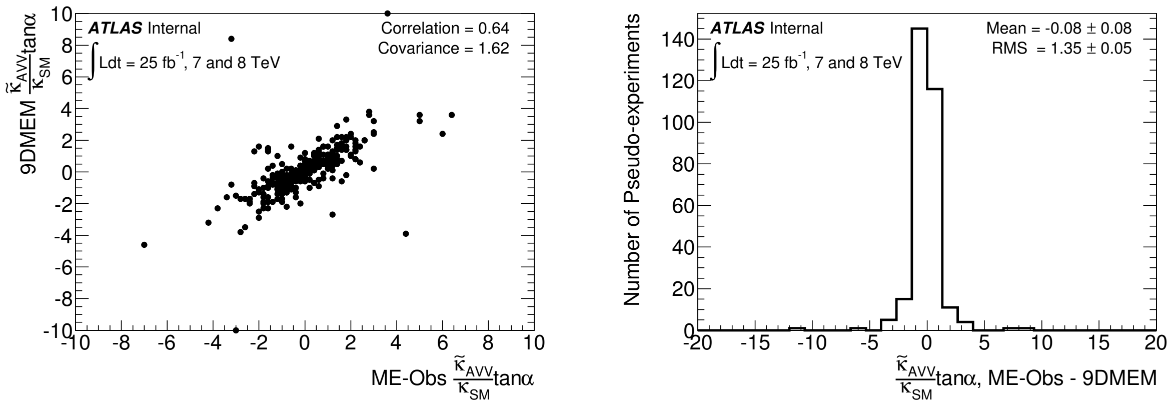

Figure 6.1: Comparison of ME-Obs and 9DMEM measurements of $\frac{\tilde{\kappa}_{AVV}}{\kappa_{SM}} \tan\alpha$ in an ensemble of 300 SM pseudo-experiments generated from MC. The plot on the left is a two-dimensional scatter of the ME-Obs measurement vs. the 9DMEM measurement. The correlation coefficient reported on the plot is given by the covariance divided by the product of the individual standard deviations from each method. A value close to one indicates that the measurements have a positive linear relationship and that the points fall near a straight line with slope equal to one. The plot on the right is a histogram of the difference in the measured value for each pseudo-experiment. The mean of the histogram is found to be consistent with zero, which confirms that the two methods are compatible.

The results from the ME-Obs method for the data are shown in Figure 6.2. The maximum likelihood estimate of $\frac{\tilde{\kappa}_{AVV}}{\kappa_{SM}} \tan\alpha = -0.8^{+0.9}_{-0.9}$ assuming $\frac{\tilde{\kappa}_{HVV}}{\kappa_{SM}} = 0$, and the maximum likelihood estimate of $\frac{\tilde{\kappa}_{HVV}}{\kappa_{SM}} = -0.2^{+0.7}_{-0.4}$ assuming $\frac{\tilde{\kappa}_{AVV}}{\kappa_{SM}} \tan\alpha = 0$. The measurements are found to be very similar to the 9DMEM measurements shown in Figure 5.5. The small differences are primarily due to the different use of discriminant observables.

6.2 Combined Measurement

The HVV tensor structure is also measured in the $H \to WW^* \to e\nu\mu\nu$ channel and the result is combined with the $H \to ZZ^* \to 4\ell$ measurement. The ME-Obs method is chosen for the combination because it is computationally simpler. Both the ME-Obs and 9DMEM methods are capable of measuring separately the CP coupling factors and they both yield consistent results. However, the ME-Obs measurements are computationally faster by roughly an order of magnitude because the corresponding likelihood function contains fewer observables (three instead of nine). One of the primary advantages of the 9DMEM method

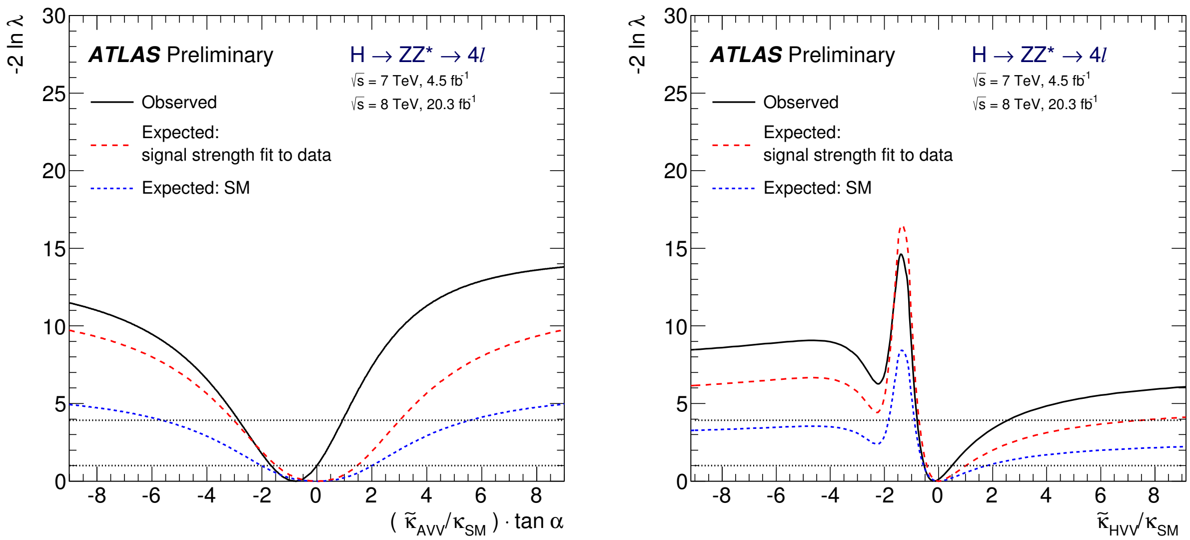

Figure 6.2: Expected and observed distributions of $-2\ln\Lambda$ as function of $\frac{\tilde{\kappa}_{AVV}}{\kappa_{SM}}\tan\alpha$ (left) and $\frac{\tilde{\kappa}_{HVV}}{\kappa_{SM}}$ (right) derived from the ME-Obs method. In both figures the dashed line represents the expectation for a SM Higgs using a signal strength that is fitted from the data under the SM assumption. The observed likelihood is represented by the solid curve. It can be seen that the fitted coupling ratios are in good agreement with the SM.

is that it allows both CP coupling factors to be measured simultaneously. This cannot be done using the ME-Obs method without adding more multivariate discriminants to the likelihood function. However, this is not relevant for the combination since the simultaneous measurement of CP coupling factors is not done in the $H \to WW^* \to e\nu\mu\nu$ channel.

The $H \to WW^*$ analysis is detailed in Ref. [66]. A brief summary is included here. The analysis incorporates an event selection designed to identify events consistent with a WW^* decay to mixed flavor leptons. The final state is required to have one electron, one muon, and missing energy. The leading and subleading leptons are required to have $p_{\mathrm{T}} > 22$ GeV and $p_{\mathrm{T}} > 15$ GeV, respectively. Events are vetoed if there are any reconstructed jets with $p_{\mathrm{T}} > 25$ GeV and $|\eta| < 2.5$ or $p_{\mathrm{T}} > 30$ GeV and $2.5 < |\eta| < 4.5$. Background comes from Z/γ^*+jets (Drell-Yan), diboson production, top-quark production, and W+jets where one of the jets is misidentified as a lepton. Drell-Yan events are suppressed by cuts on the dilepton kinematics requiring 20 GeV $< m_{\ell\ell} <$ 80 GeV and $\Delta\phi_{\ell\ell} < 2.8$ rad. The upper bound on $m_{\ell\ell}$ helps suppress non-resonant WW background. The contribution from misidentified leptons is suppressed by lepton isolation requirements. The total transverse mass of the two leptons and missing energy, m_T is required to be below 150 GeV. After the selection there are approximately 218 events expected from the SM Higgs signal (assuming $\mu = 1$)and 4390 events expected from background.

Two BDTs are used as the discriminant observables in the likelihood function for the WW final state. There is a BDT designed to separate signal from background, which is trained using m_T and the dilepton kinematic observables $m_{\ell\ell}$, $\Delta\phi_{\ell\ell}$, and $p_{\mathrm{T}}^{\ell\ell}$. A second BDT is used to discriminate between different CP hypotheses. This is trained using $m_{\ell\ell}$, $\Delta\phi_{\ell\ell}$, and $p_{\mathrm{T}}^{\ell\ell}$ for the measurement of $\frac{\tilde{\kappa}_{HVV}}{\kappa_{SM}}$. For the measurement of $\frac{\tilde{\kappa}_{AVV}}{\kappa_{SM}} \tan\alpha$ it is trained using $m_{\ell\ell}$, $\Delta\phi_{\ell\ell}$, the estimated energy of the $e\nu\mu\nu$ system, and the absolute difference in the lepton p_{T} values.

A measurement is done using a simultaneous fit combining the profile likelihoods from the $H \to ZZ^* \to 4\ell$ and $H \to WW^* \to e\nu\mu\nu$ analyses. The parameters $\frac{\tilde{\kappa}_{AVV}}{\kappa_{SM}} \tan\alpha$ and $\frac{\tilde{\kappa}_{HVV}}{\kappa_{SM}}$ are each measured separately (with the other assumed to be zero). It is assumed that these coupling factors are the same for the W and Z vector bosons. The signal strength parameters are treated as unconstrained nuisance parameters that are uncorrelated between the different final states and different center of mass energies. In this way, no assumptions are made regarding the relative branching fractions of the Higgs to pairs of W and Z bosons. Furthermore, no assumption is made on how the Higgs cross-section scales with energy. The constrained nuisance parameters from systematic uncertainties are correlated between the channels when it is appropriate. The expected likelihood distributions from each channel and the expected combined likelihood distributions are shown in Figure 6.3. Here, the signal strength parameters are set to the values measured in data. The observed likelihood distributions are shown in Figure 6.4. The results are found to be consistent with the SM (for the combined measurement and the individual channels). The best-fit values and 95% CL exclusions for the combination are summarized in Table 6.1.

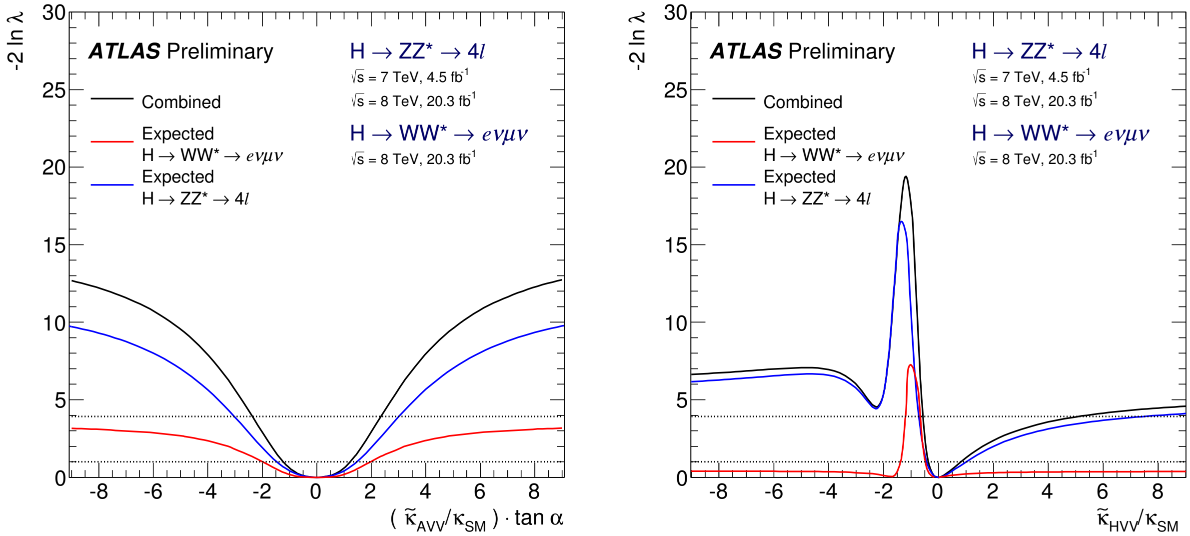

Figure 6.3: Expected distributions of $-2\ln\Lambda$ for $\frac{\tilde{\kappa}_{AVV}}{\kappa_{SM}}\tan\alpha$ (left) and $\frac{\tilde{\kappa}_{HVV}}{\kappa_{SM}}$ (right). The likelihoods are shown for the $H \to ZZ^* \to 4\ell$ (blue) and $H \to WW^* \to e\nu\mu\nu$ (red) channels. The combination is shown in black.

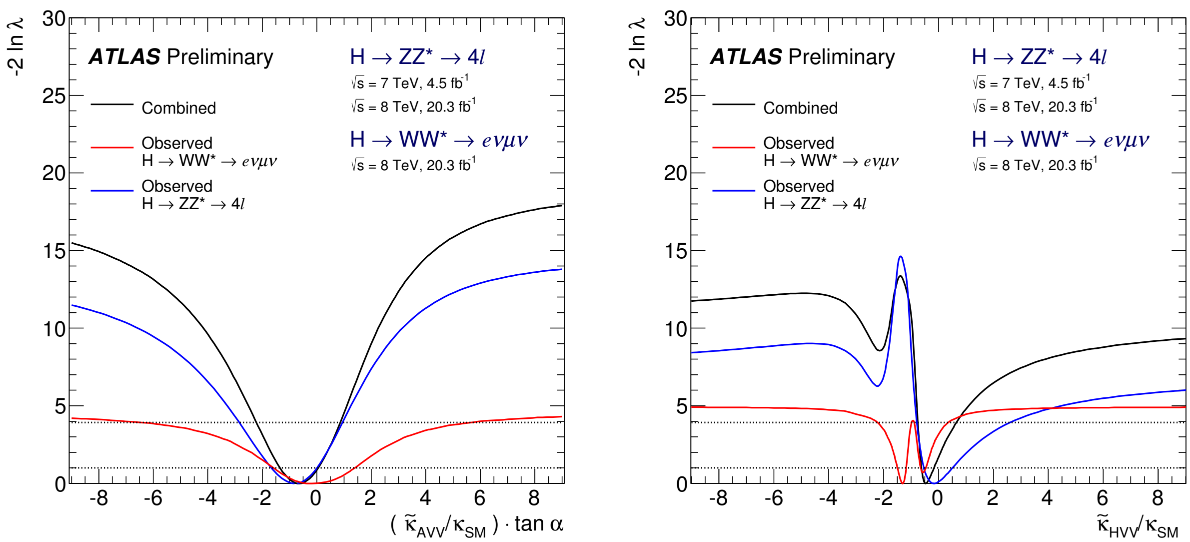

Figure 6.4: Observed distributions of $-2\ln\Lambda$ for $\frac{\tilde{\kappa}_{AVV}}{\kappa_{SM}}\tan\alpha$ (left) and $\frac{\tilde{\kappa}_{HVV}}{\kappa_{SM}}$ (right). The likelihoods are shown for the $H \to ZZ^* \to 4\ell$ (blue) and $H \to WW^* \to e\nu\mu\nu$ (red) channels. The combination is shown in black. In the plot on the right there is a region the exclusion from $H \to ZZ^* \to 4\ell$ is better than the exclusion from the combination. This is possible because the the combination with $H \to WW^* \to e\nu\mu\nu$ causes the best-fit value to shift.

Dataset	Best fit value	Regions excluded at 95% CL
Measurement of $\frac{\tilde{\kappa}_{AVV}}{\kappa_{SM}} \tan\alpha$ assuming $\frac{\tilde{\kappa}_{HVV}}{\kappa_{SM}} = 0$		
Observed	-0.68	< -2.18 and > 0.83
Expected: NPs fit to data	0.00	< -2.33 and > 2.30
Measurement of $\frac{\tilde{\kappa}_{HVV}}{\kappa_{SM}}$ assuming $\frac{\tilde{\kappa}_{AVV}}{\kappa_{SM}} \tan\alpha = 0$		
Observed	-0.48	< -0.73 and > 0.63
Expected: NPs fit to data	0.00	< -0.55 and > 4.80

Table 6.1: Best fit values and observed exclusion regions for individual measurements of $\frac{\tilde{\kappa}_{AVV}}{\kappa_{SM}} \tan\alpha$ and $\frac{\tilde{\kappa}_{HVV}}{\kappa_{SM}}$ combining the $H \to ZZ^* \to 4\ell$ and $H \to WW^* \to e\nu\mu\nu$ channels. The expected results are derived assuming all nuisance parameters are set to the values measured in data with $\frac{\tilde{\kappa}_{AVV}}{\kappa_{SM}} \tan\alpha = \frac{\tilde{\kappa}_{HVV}}{\kappa_{SM}} = 0$.

Chapter 7

Conclusion

Studies of the tensor structure of the HVV interaction have been presented. The investigations are based on 25 fb^{-1} of proton-proton collision data collected by the ATLAS detector with center of mass energy of 7 and 8 TeV. BSM coupling factors represented by $\frac{\tilde{\kappa}_{AVV}}{\kappa_{SM}} \tan\alpha$ and $\frac{\tilde{\kappa}_{HVV}}{\kappa_{SM}}$ are searched for using $H \to ZZ^* \to 4\ell$ decays. The results are found to be compatible with the Standard Model. Values outside of the intervals $-3.24 < \frac{\tilde{\kappa}_{AVV}}{\kappa_{SM}} \tan\alpha < 0.91$ and $-0.82 < \frac{\tilde{\kappa}_{HVV}}{\kappa_{SM}} < 0.87$ are excluded at 95% CL. These results are combined with a tensor structure measurement using $H \to WW^* \to e\nu\mu\nu$ decays. After the combination, values outside of the intervals $-2.18 < \frac{\tilde{\kappa}_{AVV}}{\kappa_{SM}} \tan\alpha < 0.83$ and $-0.73 < \frac{\tilde{\kappa}_{HVV}}{\kappa_{SM}} < 0.63$ are excluded at 95% CL. These are the first direct measurements of the HVV tensor structure from ATLAS data.

The analysis presented in this thesis incorporates a challenging fit with nine discriminant observables. This will hopefully lay groundwork for future measurements characterizing the HVV vertex. The Run I dataset is too small to justify complicated fits that simultaneously measure many parameters. The large statistical uncertainty in the dataset limits the precision of results even when fitting for a single real coupling value. During and after Run II, there will be enough data at the LHC to perform measurements with more degrees of freedom. For example, when enough data accumulates it will be interesting to simultaneously measure all CP couplings, probing both real and imaginary values, in addition to the Higgs mass and production rate. Such a measurement would require a fit with many discriminant observables, but would be within the scope of the analysis method described in this thesis.

References

[1] ATLAS Collaboration, Observation of a new particle in the search for the Standard Model Higgs boson with the ATLAS detector at the LHC, *Phys. Lett.*, B 716:1–29, 2012.

[2] CMS Collaboration, Observation of a new boson at a mass of 125 GeV with the CMS experiment at the LHC, *Phys. Lett.*, B 716:30–61, 2012.

[3] Sara Bolognesi, Yanyan Gao, Andrei V. Gritsan, Kirill Melnikov, Markus Schulze, et al., On the spin and parity of a single-produced resonance at the LHC, *Phys. Rev.*, D 86:095031, 2012.

[4] S Heinemeyer et al., Handbook of LHC Higgs Cross Sections: 3. Higgs Properties, arXiv:1307.1347 [hep-ph], 2013.

[5] S.L. Glashow, Partial Symmetries of Weak Interactions, *Nucl. Phys.*, 22:579–588, 1961.

[6] Steven Weinberg, A Model of Leptons, *Phys. Rev. Lett.*, 19:1264–1266, 1967.

[7] Abdus Salam, Weak and Electromagnetic Interactions, *Conf. Proc.*, C680519:367–377, 1968.

[8] Gerard 't Hooft and M.J.G. Veltman, Regularization and Renormalization of Gauge Fields, *Nucl. Phys.*, B 44:189–213, 1972.

[9] Steven Weinberg, The Quantum theory of fields. Vol. 1: Foundations, 1995.

[10] Peter W. Higgs, Broken symmetries, massless particles and gauge fields, *Phys. Lett.*, 12:132–133, 1964.

[11] Peter W. Higgs, Broken Symmetries and the Masses of Gauge Bosons, *Phys. Rev. Lett.*, 13:508–509, 1964.

[12] F. Englert and R. Brout, Broken Symmetry and the Mass of Gauge Vector Mesons, *Phys. Rev. Lett.*, 13:321–323, 1964.

[13] G.S. Guralnik, C.R. Hagen, and T.W.B. Kibble, Global Conservation Laws and Massless Particles, *Phys. Rev. Lett.*, 13:585–587, 1964.

[14] Peter W. Higgs, Spontaneous Symmetry Breakdown without Massless Bosons, *Phys. Rev.*, 145:1156–1163, 1966.

[15] ATLAS and CMS Collaborations, Combined Measurement of the Higgs Boson Mass in pp Collisions at $\sqrt{s} = 7$ and 8 TeV with the ATLAS and CMS Experiments, *Phys. Rev. Lett.*, 114:191803, 2015.

[16] B.T. Cleveland, Timothy Daily, Jr. Davis, Raymond, James R. Distel, Kenneth Lande, et al., Measurement of the solar electron neutrino flux with the Homestake chlorine detector, *Astrophys. J.*, 496:505–526, 1998.

[17] V. C. Rubin, N. Thonnard, and Jr. Ford, W. K., Extended rotation curves of high-luminosity spiral galaxies. IV - Systematic dynamical properties, SA through SC, *Astrophys. J.*, 225:L107–L111, 1978.

[18] G. Paál, I. Horváth, and B. Lukács, Inflation and compactification from galaxy redshifts?, *Astrophys. Space Sci.*, 191(1):107–124, 1992.

[19] ATLAS Collaboration, Study of the spin and parity of the Higgs boson in HVV decays with the ATLAS detector, Technical Report ATLAS-CONF-2015-008, CERN, Geneva, Mar 2015.

[20] CMS Collaboration, Constraints on the spin-parity and anomalous HVV couplings of the Higgs boson in proton collisions at 7 and 8 TeV, *Submitted to Phys. Rev. D.*, arXiv:1411.3441 [hep-ex], 2014.

[21] L.D. Landau, On the angular momentum of a two-photon system, *Dokl. Akad. Nauk Ser. Fiz.*, 60:207–209, 1948.

[22] Chen-Ning Yang, Selection Rules for the Dematerialization of a Particle Into Two Photons, *Phys. Rev.*, 77:242–245, 1950.

[23] ATLAS Collaboration, Evidence for the spin-0 nature of the Higgs boson using ATLAS data, *Phys. Lett.*, B 726:120–144, 2013.

[24] P. Artoisenet, P. de Aquino, F. Demartin, R. Frederix, S. Frixione, et al., A framework for Higgs characterisation, *JHEP*, 1311:043, 2013.

[25] J. Beringer et al., Review of Particle Physics (RPP), *Phys. Rev.*, D 86:010001, 2012.

[26] Thomas Sven Pettersson and P Lefèvre, The Large Hadron Collider: conceptual design, Technical Report CERN-AC-95-05-LHC, CERN, Geneva, Oct 1995.

[27] Lyndon Evans and Philip Bryant, LHC Machine, *JINST*, 3:S08001, 2008.

[28] Oliver Sim Bruning, Paul Collier, P Lebrun, Stephen Myers, Ranko Ostojic, John Poole, and Paul Proudlock, *LHC Design Report*, CERN, Geneva, 2004.

[29] ATLAS Collaboration, The ATLAS Experiment at the CERN Large Hadron Collider, *JINST*, 3:S08003, 2008.

[30] ATLAS Collaboration, ATLAS: Detector and physics performance technical design report. Volume 1, ATLAS-TDR-14, 1999.

[31] ATLAS Collaboration, Studies of the performance of the ATLAS detector using cosmic-ray muons, *Eur. Phys. J.*, C 71:1593, 2011.

[32] ATLAS Collaboration, The ATLAS Inner Detector commissioning and calibration, *Eur. Phys. J.*, C 70:787–821, 2010.

[33] ATLAS Collaboration, Performance of the ATLAS Detector using First Collision Data, *JHEP*, 1009:056, 2010.

[34] S. Chatrchyan et al., The CMS experiment at the CERN LHC, *JINST*, 3:S08004, 2008.

[35] K. Aamodt et al., The ALICE experiment at the CERN LHC, *JINST*, 3:S08002, 2008.

[36] Jr. Alves, A. Augusto et al., The LHCb Detector at the LHC, *JINST*, 3:S08005, 2008.

[37] ATLAS Collaboration, *Online*, `https://twiki.cern.ch/twiki/bin/view/AtlasPublic/LuminosityPublicResults`.

[38] ATLAS Collaboration, Luminosity Determination in pp Collisions at $\sqrt{s} = 7$ TeV Using the ATLAS Detector at the LHC, *Eur. Phys. J.*, C 71:1630, 2011.

[39] ATLAS Collaboration, ATLAS pixel detector: Technical design report, CERN-LHCC-98-13, 1998.

[40] G. Aad, M. Ackers, F.A. Alberti, M. Aleppo, G. Alimonti, et al., ATLAS pixel detector electronics and sensors, *JINST*, 3:P07007, 2008.

[41] A. Abdesselam, T. Akimoto, P.P. Allport, J. Alonso, B. Anderson, et al., The barrel modules of the ATLAS semiconductor tracker, *Nucl. Instrum. Meth.*, A 568:642–671, 2006.

[42] A. Abdesselam et al., The ATLAS semiconductor tracker end-cap module, *Nucl. Instrum. Meth.*, A 575:353–389, 2007.

[43] E. Abat et al., The ATLAS Transition Radiation Tracker (TRT) proportional drift tube: Design and performance, *JINST*, 3:P02013, 2008.

[44] G. Aielli, A. Aloisio, M. Alviggi, V. Aprodu, V. Bocci, et al., The RPC first level muon trigger in the barrel of the ATLAS experiment, *Nucl. Phys. Proc. Suppl.*, 158:11–15, 2006.

[45] S. Majewski, Georges Charpak, A. Breskin, and G. Mikenberg, A thin multiwire chamber operating in the high multiplication mode, *Nucl. Instrum. Meth.*, 217:265–271, 1983.

[46] F. Bauer, U. Bratzler, H. Dietl, H. Kroha, T. Lagouri, et al., Construction and test of MDT chambers for the ATLAS muon spectrometer, *Nucl. Instrum. Meth.*, A 461:17–20, 2001.

[47] Theodoros Argyropoulos, Ketevi Adikle Assamagan, Brian Hugues Benedict, Valeri Chernyatin, Elliot Cheu, et al., Cathode strip chambers in ATLAS: Installation, commissioning and in situ performance, *IEEE Trans. Nucl. Sci.*, 56:1568–1574, 2009.

[48] A. Denner, S. Heinemeyer, I. Puljak, D. Rebuzzi, and M. Spira, Standard Model Higgs-Boson Branching Ratios with Uncertainties, *Eur. Phys. J.*, C 71:1753, 2011.

[49] Daniel de Florian, Giancarlo Ferrera, Massimiliano Grazzini, and Damiano Tommasini, Transverse-momentum resummation: Higgs boson production at the Tevatron and the LHC, *JHEP*, 1111:064, 2011.

[50] S. Agostinelli et al., GEANT4: A Simulation toolkit, *Nucl. Instrum. Meth.*, A 506:250–303, 2003.

[51] Michelangelo L. Mangano, Mauro Moretti, Fulvio Piccinini, Roberto Pittau, and Antonio D. Polosa, ALPGEN, a generator for hard multiparton processes in hadronic collisions, *JHEP*, 0307:001, 2003.

[52] Michelangelo L. Mangano, Mauro Moretti, Fulvio Piccinini, and Michele Treccani, Matching matrix elements and shower evolution for top-quark production in hadronic collisions, *JHEP*, 0701:013, 2007.

[53] Piotr Golonka and Zbigniew Was, PHOTOS Monte Carlo: A Precision tool for QED corrections in Z and W decays, *Eur. Phys. J.*, C 45:97–107, 2006.

[54] T. Gleisberg, Stefan. Hoeche, F. Krauss, M. Schonherr, S. Schumann, et al., Event generation with SHERPA 1.1, *JHEP*, 0902:007, 2009.

[55] ATLAS Collaboration, Measurements of the properties of the Higgs-like boson in the four lepton decay channel with the ATLAS detector using 25 fb^{-1} of proton-proton collision data, *Submitted for publication*, ATLAS-CONF-2013-013, 2013.

[56] ATLAS Collboration, Muon Performance in Minimum Bias pp Collision Data at $\sqrt{s}=$ 7 TeV with ATLAS, ATLAS-CONF-2010-036, 2010.

[57] ATLAS Collaboration, Reconstruction of collinear final-state-radiation photons in Z decays to muons in $\sqrt{s} = 7$ TeV proton-proton collisions., ATLAS-CONF-2012-143, 2012.

[58] Glen Cowan, Kyle Cranmer, Eilam Gross, and Ofer Vitells, Asymptotic formulae for likelihood-based tests of new physics, *Eur. Phys. J.*, C 71:1554, 2011.

[59] K Pearson, Note on Regression and Inheritance in the Case of Two Parents, *Proc. R. Soc. Lond.*, 58:240–242, 1895.

[60] Murray Rosenblatt, Remarks on some nonparametric estimates of a density function., *Ann. Math. Stat.*, 27:832–837, 1956.

[61] E. Parzen, On estimation of a probability density function and mode., *Ann. Math. Stat.*, 33:1065–1076, 1962.

[62] ATLAS Collaboration, Measurement of the Higgs boson mass from the $H \rightarrow \gamma\gamma$ and $H \rightarrow ZZ^* \rightarrow 4\ell$ channels with the ATLAS detector using 25 fb^{-1} of pp collision data, *Phys. Rev.*, D 90(5):052004, 2014.

[63] S H Abidi, C Anastopoulos, et al., Event selection and background estimation for the measurement of the properties of the Higgs particle in the four lepton decay channel with the ATLAS detector, Technical Report ATL-PHYS-INT-2014-032, CERN, Geneva, Oct 2014.

[64] ATLAS Collaboration, Improved luminosity determination in pp collisions at $\sqrt{s} =$ 7 TeV using the ATLAS detector at the LHC, *Eur. Phys. J.*, C 73(8):2518, 2013.

[65] D. Atwood and A. Soni, Analysis for magnetic moment and electric dipole moment form factors of the top quark via $e^+e^- \rightarrow t\bar{t}$, *Phys. Rev. D*, 45:2405–2413, 1992.

[66] ATLAS Collaboration, Determination of spin and parity of the Higgs boson in the $WW^* \rightarrow e\nu\mu\nu$ decay channel with the ATLAS detector, *Submitted to Eur. Phys. J.*, arXiv:1503.03643 [hep-ex], 2015.